Technical Physics Letters, Vol. 29, No. 10, 2003, pp. 791–792. Translated from Pis'ma v Zhurnal Tekhnicheskoĭ Fiziki, Vol. 29, No. 19, 2003, pp. 1–4.

Additional Relationship between Canonical and Microcanonical Ensembles in Classical Statistical Mechanics

A. Yu. Zakharov

Novgorod State University, Novgorod, Russia

e-mail: ayz@novsu.ac.ru

Received February 3, 2003

Abstract—A one-to-one relationship is established between the accessible volume in the phase space of a microcanonical ensemble and the canonical partition function. *© 2003 MAIK "Nauka/Interperiodica".*

The state of the art in statistical mechanics in general and even in the classical branch cannot be considered as satisfactory [1–3]. The point is not even that no one model with more or less realistic interaction between particles admits an exact solution or qualitative analysis. It is not less significant that the very transition from classical mechanics to classical statistical mechanics encounters serious logical problems, beginning with the ergodic hypothesis (sometimes considered as not very significant) and ending with interrelations between ensembles.

For example, the transition from a microcanonical ensemble to the canonical one is based to a significant extent on several uncontrolled hypotheses that are valid for the ideal gas, whereas nothing is known about the "stability" of these assumptions with respect to interactions in the system under study. In particular, the procedure of replacing an arbitrarily thin spherical layer $E - \epsilon \le \sum_{k=1}^{N} \mathbf{p}_k^2/2m \le E$ in the momentum space by the volume of a sphere with $0 \le \sum_{k=1}^{N} \mathbf{p}_k^2/2m \le E$ for calculating the phase volume Γ of the ideal gas is unconditionally justified. At the same time, the analogous statement about the possibility of replacing an arbitrarily thin layer

$$E - \epsilon \le H(p, q) \le E \tag{1}$$

(where $H(p, q)$ is the system Hamiltonian) with the entire volume of the phase space inside the constant energy surface of a system of particles is quite reasonably doubted.

On the other hand, the derivation of all sequential ensembles in statistical mechanics, which are practically much more "advanced" than a microcanonical ensemble, relies substantially on the latter ensemble. Therefore, it would be important to render the microcanonical ensemble "working" to the same extent as the canonical or grand canonical ensembles. To this end, it is necessary to find a method of calculating the phase volume of a system between two close surfaces of constant energy.

Consider a classical system of N identical particles interacting with each other and with an external field. Let this system occupy the volume V and be isolated from the environment. The state of the system is determined by the position of the imaging point in the phase space Γ, while evolution of the system is described by the canonical Hamilton equations of motion. For the isolated system under consideration, the imaging point in the phase space moves over the constant energy surface given by the equation $H(p, q) - E = 0$, where E is the system energy.

Let the system energy be not fixed but confined within an interval $[E - \epsilon, E]$, where $\epsilon > 0$. Then, the accessible volume $\Delta\Gamma$ of the phase space of the system is

$$\Delta\Gamma = \int \chi_{[E-\epsilon, E]}(H(p, q))d\Gamma, \tag{2}$$

where

$$\chi_\Omega(x) = \begin{cases} 1, & x \in \Omega; \\ 0, & x \notin \Omega \end{cases} \tag{3}$$

is the characteristic function (indicator) of the set Ω. In integral (2), this function imparts the unit weight to all points in the phase space corresponding to the system energies in the interval $[E - \epsilon, E]$ and zero weight, to all points outside this interval. Thus, integral (2) determines the volume of the phase space confined between the surfaces $H(p, q) = E - \epsilon$ (σ_1) and $H(p, q) = E$ (σ_2). It should be noted that, in the general case, the manifolds σ_1 and σ_2 can be independent (non-connected).

1063-7850/03/2910-0791$24.00

Introducing an integral representation of the above characteristic function of the manifold,

$$\chi_{[E-\epsilon, E]}(x) = \frac{1}{\pi}\int_{-\infty}^{\infty} \frac{\sin\left(\frac{\tau\epsilon}{2}\right)}{\tau} \exp\left[i\tau\left(x - E + \frac{\epsilon}{2}\right)\right] d\tau, \quad (4)$$

and substituting expression (4) into relation (2), we obtain

$$\Delta\Gamma(N, V, E, \epsilon) = \frac{1}{\pi}\int_{-\infty}^{\infty} \frac{\sin\left(\frac{\tau\epsilon}{2}\right)}{\tau} \exp\left[-i\tau\left(E + \frac{\epsilon}{2}\right)\right] \quad (5)$$
$$\times \left(\int \exp[i\tau H(p, q)] dp dq\right) d\tau.$$

Note that the internal integral over the phase space is the canonical partition function Z of the system at an imaginary temperature $T = \beta^{-1} = i/\tau$:

$$Z(N, V, i\tau) = \int \exp[i\tau H(p, q)] dp dq. \quad (6)$$

Therefore,

$$\Delta\Gamma(N, V, E, \epsilon) = \frac{1}{\pi}\int_{-\infty}^{\infty} \frac{\sin\left(\frac{\tau\epsilon}{2}\right)}{\tau} \quad (7)$$
$$\times \exp\left[-i\tau\left(E - \frac{\epsilon}{2}\right)\right] Z(N, V, i\tau) d\tau.$$

Thus, for the microcanonical ensemble, the accessible volume $\Delta\Gamma$ of the phase space of the system is obtained via integral transformation of the canonical partition function $Z(i\tau)$ of this system considered as a function of the imaginary temperature $i\tau$.

Note that the established integral relationship between $\Delta\Gamma$ and $Z(i\tau)$ is valid irrespective of the thermodynamic transition $N, V \longrightarrow \infty$ ($N/V = n$ = const), which is especially important in connection to the investigations of nanostructures, extensively developed in recent years, and to the theory of phase transitions, since no correct thermodynamics of small systems (such as nuclei of new phases) has yet been developed.

Acknowledgments. This study was supported in parts by the Federal Program "Universities of Russia" (project no. UR.01.01.024), the Program of Russia–Netherlands Cooperation (NWO project 047.011.2001.011), and the Federal Targeted Program "Integration" (project no. B0056).

REFERENCES

1. F. A. Berezin, *Lectures on Statistical Physics* (Inst. Komp. Issled., Moscow–Izhevsk, 2002).
2. D. Ruelle, *Thermodynamic Formalism. The Mathematical Structures of Classical Equilibrium Statistical Mechanics* (Addison-Wesley, London, 1978).
3. H.-O. Georgii, O. Hänggström, and C. Maes, *Phase Transitions and Critical Phenomena*, Ed. by C. Domb and J. Lebowitz (Academic, London, 2000), Vol. 18, pp. 1–142.

Translated by P. Pozdeev

Technical Physics Letters, Vol. 29, No. 10, 2003, pp. 793–796. Translated from Pis'ma v Zhurnal Tekhnicheskoĭ Fiziki, Vol. 29, No. 19, 2003, pp. 5–12.

The Area Theorems for Two-Core Nonlinear Directional Couplers

P. I. Khadzhi and O. V. Korovay

Dniester State University, Tiraspol, Moldova

e-mail: tdsu4@idknet.com

Revised manuscript received May 6, 2003

Abstract—The area theorems, describing propagation of ultrashort pulses of resonant laser radiation in a two-core nonlinear directional coupler, are formulated for the first time. It is shown that such a system is characterized by a finite, bounded above set of areas of the stationary propagating pulses. We also predict quantization of the limit cycles and possible existence of the regime of periodic complete transfer of the radiation energy from one fiber to another. © *2003 MAIK "Nauka/Interperiodica".*

It was demonstrated [1–5] that nonlinear directional couplers (NLDCs) are capable of providing all-optical signal switching. For the model of a nonlinear resonant coupler based on a dielectric matrix doped with resonant absorbing centers [1], the numerical experiment revealed localization of a light pulse in one channel and the energy transfer from one channel to another by portions equal to a multiple of the 2π soliton energy. Investigations of the phenomenon of soliton switching [2, 3] showed that the process of energy transfer significantly depends on the initial pulse shape. Assuming the localization of light in one fiber, the shape of a solitonlike pulse was determined [3].

McCall and Hahn [5] showed that the stable soliton pulses are governed by the area theorem, according to which a single-soliton solution of the Maxwell–Bloch equations has the form of a pulse with an area of 2π. This soliton can propagate in a bulk medium consisting of two-level atoms. For more complicated physical objects, such as NLDCs, the area theorem has not yet been formulated. Should such a law be established, it would be possible to make a conclusion about the areas of stationary propagating pulses in fibers of NLDCs.

Below, we will show that the area theorem for NLDCs is represented by a system of two nonlinear differential equations describing the areas of pulses propagating in each fiber of the coupler. We consider an NLDC comprising a pair of identical tunneling-coupled fibers. The tunneling coupling between fields in the fibers is provided by the field penetrating from one fiber into another. The fiber material is modeled by a system of two-level atoms exhibiting resonance interaction with the propagating wave field. We assume that ultrashort pulses of laser radiation propagating in the fibers possess a width smaller than the characteristic excitation relaxation time of the host medium.

Using the material Bloch equations and the wave equations for the fields of pulses, we obtain a system of Maxwell–Bloch equations in the well-known approximation of envelopes slowly varying in space and time:

$$i\dot{\rho}_j = \sigma(q_j^+ E_j^- - q_j^- E_j^+), \tag{1}$$

$$i\dot{q}_j^+ = -\sigma\rho_j E_j^+/2, \tag{2}$$

$$\frac{\partial E_j^+}{\partial t} + c\frac{\partial E_j^+}{\partial x} = 2i\pi\hbar\omega(\sigma q_j^+ + \mu E_{3-j}^+), \tag{3}$$

where E_j^+ (E_j^-) is the positive-frequency (negative-frequency) component of the electric field of the electromagnetic wave propagating in the jth fiber (j = 1, 2) with the frequency ω and the wave vector k_j; q_j^+ is the polarization of the medium; ρ_j is the difference between populations of the levels; μ is the constant of tunneling coupling between fibers [5], $\sigma = d/\hbar$; and d is the dipole moment of the transition between levels.

Assuming that the laser radiation excites the same eigenmode in both fibers, we use the following ansatz: the complex wave field $E_j^+(x, t)$ is represented as a product of the amplitude $E_j(x, t)$, considered as a function of both coordinate and time, and the phase $\varphi_j(x)$ depending only on the coordinate: $E_j^+ = E_j(x, t)\exp(i\varphi_j(x))$. Applying the approach developed in [8] to Eqs. (1)–(3), it is easy to obtain a system of nonlinear differential equations describing spatial variation of the areas $\Theta_j(x)$

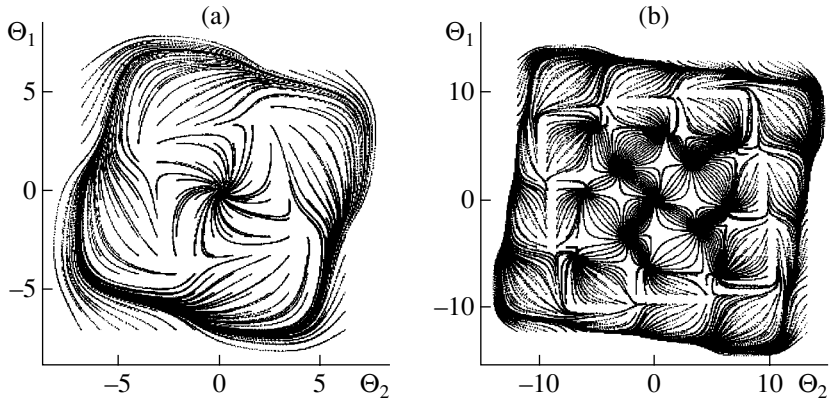

Fig. 1. Phase trajectories of a system of Eqs. (7)–(8) for $a = \alpha/2\kappa = 3$ (a) and 8 (b).

of the ultrashort pulses propagating in each fiber:

$$\frac{d\Theta_1}{dx} = -\frac{\alpha}{2}\sin\Theta_1 - \kappa\Theta_2\sin\varphi, \quad (4)$$

$$\frac{d\Theta_2}{dx} = -\frac{\alpha}{2}\sin\Theta_2 + \kappa\Theta_1\sin\varphi, \quad (5)$$

$$\frac{d\varphi}{dx} = \kappa\frac{\Theta_1^2 - \Theta_2^2}{\Theta_1\Theta_2}\cos\varphi. \quad (6)$$

Here, the pulse area $\Theta_j(x)$ is defined by the formula

$$\Theta_j(x) = \sigma\int_{-\infty}^{\infty} E_j(x, t)dt$$

and

$$\varphi(x) = \varphi_2(x) - \varphi_1(x),$$

α is the linear absorption coefficient of the medium [6–8], and κ is the coupling constant [2–5]. The above system of equations has to be supplemented with the boundary conditions for $\Theta_j(0)$ and $\varphi(0)$. As for the initial phase $\varphi(0)$, we select this value proceeding from the linear approximation of Eqs. (4)–(6), whereby the initial areas of pulses $\Theta_j(0) \ll 1$. As can be readily shown, this limit implies that $\varphi(x) = \pi/2$. Taking this value for the initial phase, we arrive at the conclusion that the phase is always equal to $\pi/2$, that is, the phase does not vary in space (in other words, the propagating pulse is not phase-modulated).

Under these conditions, Eqs. (4)–(6) transform into the final system of two equations describing spatial variation of the areas of propagating pulses:

$$\frac{d\Theta_1}{dx} = -\frac{\alpha}{2}\sin\Theta_1 - \kappa\Theta_2, \quad (7)$$

$$\frac{d\Theta_2}{dx} = -\frac{\alpha}{2}\sin\Theta_2 + \kappa\Theta_1. \quad (8)$$

Under the assumption that $\kappa = 0$ (i.e., that the fibers do not interact), these equations became mutually independent and can be reduced to the well-known McCall–Hahn area theorem [6, 7]: $d\Theta/dx = -(\alpha/2)\sin\Theta$. This relation indicates that stable propagating pulses possess the areas $\Theta = 0, 2\pi, 4\pi, \ldots, 2k\pi$ (where k is an integer), while the pulses with $\Theta = \pi, 3\pi, \ldots, (2k + 1)\pi$ are unstable. In the case of $\alpha = 0$ (a system of two-level atoms without absorption), Eqs. (7)–(8) convert into the well-known equations describing a linear directional coupler with the solutions $\Theta_1(x) = \Theta_{10}\cos(kx)$ and $\Theta_2(x) = \Theta_{10}\sin(kx)$, where Θ_{10} is the pulse area in the first fiber at $x = 0$.

In the general case, system (7)–(8) has no analytical solutions. Below, we will treat the solutions qualitatively and illustrate the results of analysis by numerical solutions. Assuming in Eqs. (7)–(8) that $d\Theta_j/dx = 0$ ($j = 1, 2$), we arrive at a system of transcendental equations whose solutions determine the coordinates of singular points $(\Theta_{s1}, \Theta_{s2})$ on the phase plane, which correspond to the areas of stationary propagating pulses. These stationary areas significantly depend on the parameter $a = \alpha/2\kappa$. For any value of a, there exist a finite, limited from above, number of stationary areas Θ_{js} ($j = 1, 2$).

Note that, for small values of the parameter a ($a < \pi$), there is only one singular point with the coordinates $\Theta_{s1} = \Theta_{s2} = 0$, which is a stable focus of the system (Fig. 1a). As can be seen from Fig. 1a, all phase trajectories in a certain region of the phase plane are directed toward this point, while outside of this region, the phase trajectories tend to a limiting cycle having the shape of a slightly rotated and distorted square. Therefore, should the initial values $\Theta_1(0)$ and $\Theta_2(0)$ of the pulses belong to the basin of attraction to the singular point, the areas of such pulses will decrease, tending to zero in the course of propagation. Thus, for $a < \pi$, stable propagating pulses represent the 0π solitons. A different behavior is observed for the pulses with initial areas belonging to the basin of attraction of the limiting cycle. Their areas exhibit periodic variations in the course of propagation and the process reduces to peri-

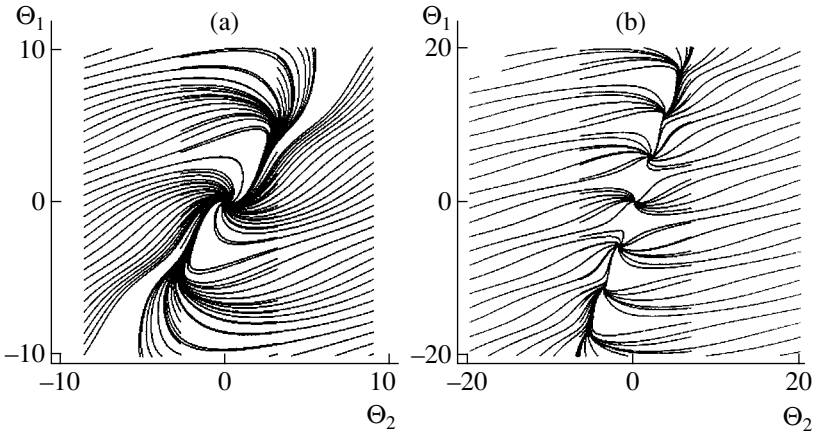

Fig. 2. Phase trajectories of a system of Eqs. (9)–(10) for $\alpha_1/2\kappa = \alpha_2/2\kappa = \sqrt{3}$ (a) and $\sqrt{10}$ (b).

odic transfer of the energy from one fiber to another, which is characteristic of stationary operation of directional couplers [5]. Note that the first limiting cycle (closest to the stable focus at the center) of system (7)–(8) is followed by an infinite number of concentric limiting cycles receding from the center.

For $a > \pi$, the situation becomes more complicated because the number of stationary points increases. For $a = 5$, the number of such points increases to nine, of which only one point with the coordinates $\Theta_{s1} = \Theta_{s2} = 0$ is a stable focus of the system, four points being unstable foci and the remaining four representing saddles. The first limiting cycle, formed outside of the region containing these singular points, is followed by a sequence of concentric limiting cycles receding from the center. Therefore, the system with $a = 5$ (like that with $a = 3$) possesses a single stationary singular point attracting the trajectories from a certain region of pulse areas. Outside this region, the system occurs in a regime of periodic complete transfer of radiation from one fiber to another.

As the parameter a grows further, the structure of phase trajectories becomes still more complicated. For example, a system with $a = 8$ (Fig. 1b) features 25 singular points, of which nine points are stable foci, four points are unstable foci, and the remainder twelve points are saddles. Each stable focus has a basin of attraction. Pulses with the initial areas $\Theta_1(0)$ and $\Theta_2(0)$ belonging to a certain basin of attraction evolve in the course of propagation so that their areas at large distances correspond to the coordinates of the given focus. As can be seen from Figs. 1a and 1b, the values of stationary areas Θ_{s1} and Θ_{s2} in the first and second fiber, corresponding to the same singular point, can be either approximately equal or significantly different. The latter case corresponds to the regime of propagation accompanied by predominant localization of the radiation energy in one of the two fibers. Further growth in the parameter a leads to the generation of new singular points contained inside the limiting cycles. However, it should be noted that the number of singular points is finite, rather than infinite as in the case of the McCall–Hahn area theorem.

Thus, Eqs. (7)–(8) show that the system is characterized by a finite, limited from above, number of areas of the stationary propagating pulses. The areas of such stationary pulses in the two fibers are not arbitrary and are related to one another by transcendental relationships. The obtained area theorems reveal an infinite sequences of concentric limiting cycles, suggesting that regimes are possible in which the radiation energy is periodically completely transferred from one fiber to another and back. These limiting cycles are quantized like periodic orbits. Each next curve representing a limiting cycle intersects the Θ_1 and Θ_2 axes at the points spaced exactly by 2π from the points of intersection with the preceding curve. The values of Θ_1 and Θ_2 vary continuously and periodically along each limiting cycle, but the passage from one limiting cycle to the next is accompanied by a jumplike change in the area of one pulse by 2π. Note that no such quantization of the limiting cycles takes place in the case of radiation pulses stationary propagating in NLDCs [5].

In the case when one fiber in an NLDC is linear and the other contains resonant two-level centers, Eqs. (7)–(8) transform to

$$\frac{d\Theta_1}{dx} = -\frac{\alpha_1}{2}\sin\Theta_1 - \kappa\Theta_2, \tag{9}$$

$$\frac{d\Theta_2}{dx} = -\frac{\alpha_2}{2}\Theta_2 + \kappa\Theta_1, \tag{10}$$

where α_1 and α_2 are the coefficients of linear absorption of the corresponding fiber materials.

Figure 2a shows the phase trajectories of the system (9)–(10) with $\alpha_1/2\kappa = \alpha_2/2\kappa = \sqrt{3}$, which converge to the point with $\Theta_{s1} = \Theta_{s2} = 0$, irrespective of the initial point. Some regions of the phase space show

dense bundles of phase trajectories. This behavior of the areas of stationary propagating pulses also significantly differs from that predicted by the McCall–Hahn theory.

Figure 2b demonstrates the behavior of phase trajectories in a system with $\alpha_1/2\kappa = \alpha_2/2\kappa = \sqrt{10}$. In this case, Eqs. (9)–(10) have five singular points, of which three are stable foci and two others are saddles. As can be seen, the phase trajectories converge to stable foci. Irrespective of how large are the initial areas of pulses, Θ_{10} and Θ_{20}, the areas of propagating pulses tend to the values corresponding to one of the stable foci. As can also be seen from Fig. 2b, each stable focus has a basin of attraction and some regions of the phase space show dense bundles of phase trajectories. Thus, the system described by Eqs. (9)–(10) is characterized by a finite, limited from above, number of areas of the stationary propagating pulses. In this case, the limiting cycles are absent.

In conclusion, the area theorems obtained for NLDCs with like or unlike fibers exhibit qualitatively different behavior of the areas of propagating pulses. This behavior is also significantly different from that observed in a volume medium in the self-induced transparency regime.

REFERENCES

1. M. Guzman, M. Romagnoli, and S. Wabnitz, Appl. Phys. Lett. **56**, 614 (1990).
2. F. Kh. Abdullaev, S. A. Darmanyan, and V. I. Goncharov, Pis'ma Zh. Tekh. Fiz. **18** (14), 29 (1992) [Sov. Tech. Phys. Lett. **18**, 448 (1992)].
3. F. Kh. Abdullaev and R. Gulyamov, Pis'ma Zh. Tekh. Fiz. **18** (20), 10 (1992) [Sov. Tech. Phys. Lett. **18**, 653 (1992)].
4. F. Kh. Abdullaev, S. A. Darmanyan, and P. K. Khabibullaev, *Optical Solitons* (Fan, Tashkent, 1987), p. 200.
5. A. A. Maĭer, Usp. Fiz. Nauk **166**, 1171 (1996) [Phys. Usp. **39**, 1109 (1996)].
6. S. L. McCall and E. L. Hahn, Phys. Rev. **183**, 457 (1969).
7. L. Allen and J. H. Eberly, *Optical Resonance and Two-Level Atoms* (Wiley, New York, 1975; Mir, Moscow, 1978).
8. V. A. Alekseev and B. Ya. Zel'dovich, Kvantovaya Élektron. (Moscow) **2**, 1078 (1975).

Translated by P. Pozdeev

Technical Physics Letters, Vol. 29, No. 10, 2003, pp. 797–800. Translated from Pis'ma v Zhurnal Tekhnicheskoĭ Fiziki, Vol. 29, No. 19, 2003, pp. 13–20.

On the Role of Exothermal Chemical Reaction during Wire Explosion in Water

V. P. Kortkhonjia

Andronikashvili Institute of Physics, Academy of Sciences of Georgia, Tbilisi, Georgia

e-mail: lado@iph.hepi.edu.ge

Received February 7, 2003; in final form, April 25, 2003

Abstract—The explosion of a metal wire in water, accompanied by exothermal chemical reaction with evolution of a large amount of heat, gives rise to thermal ionization of the reaction products. As a result, a dense plasma is generated and energy on the order of or greater than that initially accumulated in the storage battery is liberated. *© 2003 MAIK "Nauka/Interperiodica".*

The electrical explosion of a wire as a result of a high-power pulse of current offers a convenient model for basic investigations of various physical phenomena involving high energy densities. On the other hand, there are many technical applications of the electrical explosion of wires: generation of high pressure pulses by the explosion in a liquid medium [1–3], synthesis of nanopowders [4], etc.

Considering the explosion of a wire in liquid as a means of creating pulsed pressure, it is necessary to evaluate the efficiency of this process. For this purpose, we have to determine what part of the energy initially stored in a capacitor bank is deposited in the discharge. To this end, we obtained oscillograms of the discharge parameters, current and voltage, and determined the deposited energy by numerically integrating these curves.

Of special interest are the cases when the explosion of a metal wire in a liquid medium involves a chemical reaction between the metal and this liquid [3, 5]. In particular, the explosion in water usually leads to the formation of metal oxides and is accompanied by evolution of a large amount of heat, because the reactions between metals and water are exothermal. In the general case, such reactions can be described by the equation

$$mM + n\mathrm{H_2O} \longrightarrow Ox + n\mathrm{H_2O} + Q,$$

where M is the mass of the exploded metal, Ox is the mass of the oxide products, and Q is the reaction heat.

In our experiments, wires of various metals (aluminum, titanium, tantalum, tungsten, and molybdenum) were exploded in water. The samples had various diameters and a length of 23 cm. The experiments were performed in a discharger of the trigatron type [6] with graphite electrodes. Figure 1 shows the oscillograms of current (upper curves) and voltage (lower curve) measured during the explosion of aluminum (Figs. 1a and 1b) and titanium (Fig. 1c) wires. As can be seen from these data, the passage of the initial current pulse (the first peak on the left) through a metal is accompanied by a secondary pulse (the rightmost peak) appearing with some delay, or without it, depending on the applied voltage (the storage battery voltage). The latter

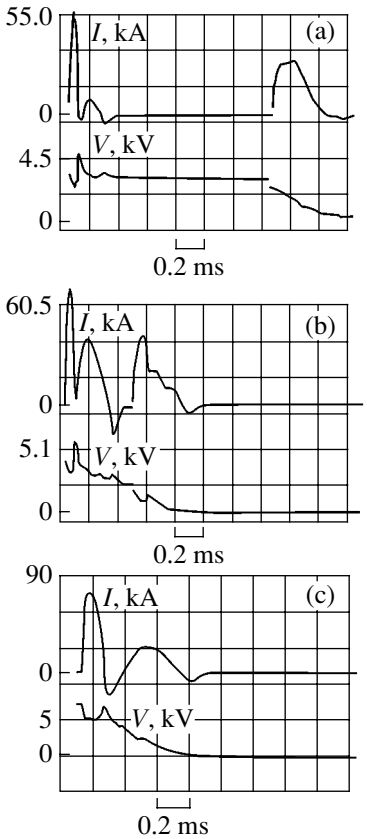

Fig. 1. The oscillograms of current and voltage measured during the explosion of (a, b) aluminum and (c) titanium wires in water at V = 4.6 (a), 5.1 (b), and 5.0 kV (c).

Table

No.	Metal	Mass, g	Capacitor bank energy E_0, kJ	System energy E_S, kJ	Reaction heat q, kJ	Integrated energy E^Σ, kJ	$E^\Sigma - E_0$, kJ	$\frac{N_i}{N}$, 10^{-2}	Temperature of reaction products T, 10^4 K
1	Al	0.31	16.2		19.20	23.36	7.17		
2	Al	0.31	19.9	19.0	19.20	30.37	10.6	<0.1	
3	Al	0.31	24.7	19.6	19.20	42.00	17.55	0.1	1.0
4	Mo	0.44	23.5	31.0	3.52	54.45	30.95	0.14	2.3
5	W	0.613	23.5	33.95	2.76	57.45	33.95	0.244	5.0
6	Ti	2.08	23.5		65.87	43.55	20.05		
7	Ti	3.25	23.5		102.9	52.0	28.5		
8	Ta	0.747	23.5	25.5	8.65	46.7	23.2	0.11	0.11
9	Ta	1.50	23.5	31.95	17.3	53.41	29.90	0.15	0.15

pulse is related to the passage of current through the chemical reaction products. It is possible to observe how this pulse shifts leftward with increasing voltage (cf. Figs. 1a and 1b). This is explained by the fact that the explosion is followed by the formation of a cylindrical region (coaxial with the exploding wire) filled with the products of reaction between water and metal. The pressure and temperature in this cylindrical region are high due to a large amount of heat liberated from the exothermal chemical reaction. The current cannot pass through the products until the pressure drops to a level at which breakdown is possible. This delay is clearly illustrated by Fig. 1a.

The results of numerical integration of the current and voltage oscillograms are presented in the table. As can be seen from these data, the value of energy E^Σ obtained by numerical integration of the discharge current and voltage curves exceeds the energy E_0 accumulated in the storage battery. As a result of the exothermal chemical reaction, the system acquires an energy denoted by E_S. Evolution of the large amount of heat leads to thermal ionization of the reaction products (this process is considered below), resulting in the formation of a dense plasma (with a density on the order of 10^{18} cm^{-3}). This plasma is polarized so that the capacitor bank is charged to a voltage of about 6 kV.

Thus, the value of E^Σ usually exceeds the energy E_0 accumulated in the storage battery. In the case of explosion of aluminum and titanium wires, the excess energy $\Delta = E^\Sigma - E_0$ is close to the energy of exothermal chemical reactions. For the explosion of refractory metal wires, the excess energy is greater than the values of the heat of formation of the corresponding oxides known to the author. It is not excluded that plasma chemical reactions may lead to the formation of oxides possessing higher heats of formation Q (the values of Q were taken from [7]). The values of the reaction heat q in the table were calculated for the known amount of a metal entering into the reaction.

From an analysis of the oscillograms, it is also possible to determine the number of charged particles N_i in the plasma and to estimate the temperature T and the degree of ionization N_i/N of this plasma (see table). The temperature T was calculated using the Saha equation [8].

Thus, it is necessary to emphasize the following experimental features:

(i) In the case of a titanium wire with a diameter d_0 = 2 mm, the energy stored in the capacitor bank was insufficient to explode the sample of the corresponding mass, provided that the required energy is calculated by the formula

$$Q = m[c(T_2 - T_1) + q_m + c(T_3 - T_2) + \lambda + \ldots],$$

where m is the mass of the metal wire, q_m is the specific heat of melting, λ is the specific heat of vaporization, c is the heat capacity, T_1 is the initial temperature, T_2 is the melting temperature, and T_3 is the temperature of evaporation. Thus, the explosion takes place only due to a chemical reaction between the heated titanium wire and water leading to the oxide formation.

(ii) In the case of aluminum wires, the excess energy Δ increases with the initial voltage to which the capacitor bank is charged.

(iii) In the case of tantalum, tungsten, and molybdenum wires (Fig. 2), the energy excess relative to that stored in the capacitor bank cannot be explained using the values of the heat of formation of the corresponding

oxides known to the author (see table). It is likely that plasmachemical reactions may lead to the formation of oxides possessing higher heats of formation.

Now let us consider the mechanism of the observed phenomenon. This analysis is well illustrated by Fig. 1a. On the oscillogram of current, the first sharp peak on the left corresponds to the current passing through the aluminum wire. The current pulse amplitude was on the order of 55 kA. This current pulse leads to melting of the metal and the development of a magnetohydrodynamic instability of the waist type [9], which results in breakage of the liquid metal column into separate parts. This is clearly seen in the photographs obtained using a high-speed photoregistrator [3]. Since the residual voltage drop across the discharge gap upon melting of the wire is insufficient to evaporate the metal, the current ceases to pass through the melted metal. At the moment of wire breakage, the electric circuit response leads to overvoltage across the discharge gap. This voltage is sufficient to initiate the arc between separate parts of the liquid metal column, which causes evaporation of the metal.

As the aluminum wire is heated, the metal enters into exothermal chemical reaction between the metal and water:

$$2Al + 3H_2O \longrightarrow Al_2O_3 + 3H_2 + Q,$$

where Q = 1672 kJ/mol is the reaction heat per mole of the metal. The reaction products are ionized by the UV radiation generated in the course of the wire explosion. Additional ionization is related to the large thermal energy liberated from the exothermal reaction, whereby the reaction products are heated to a temperature on the order of 10^4 K (see table). The plasma contacts with the wall and becomes polarized. The discharge current changes direction and charges the capacitor bank up to about 5.0 kV. At the time t = 0.4 ms, the voltage applied to the discharge gap is about 4.5 kV and the energy stored in the capacitor bank amounts to 19.0 kJ. During the time interval from t = 0.4 ms to t =1.48 ms, the current is zero and the battery voltage slightly decreases. This voltage is insufficient to cause breakdown of the plasma of reaction products occurring at a high pressure [2, 3]. The pressure decreases with time and, beginning with t = 1.48 ms, the current passes through the plasma until almost complete discharge of the capacitor bank. Numerical integration of the current and voltage oscillograms in this region (Fig. 1a) yields an energy of about 10.6 kJ, which is comparable to the energy stored in the capacitor bank (19.0 kJ).

As can be seen from the oscillograms of current and voltage measured during the explosion of refractory metal wires, the current begins to pass through the reaction products immediately after the explosion. This behavior is explained by the fact that, at the moment of metal evaporation (i.e., about t = 0.2 ms), the voltage drop across the discharge gap reaches 6 kV. This voltage is sufficient for the current to pass through the dense plasma of chemical reaction products. In all cases, a deposit formed in the system consists of metal oxides.

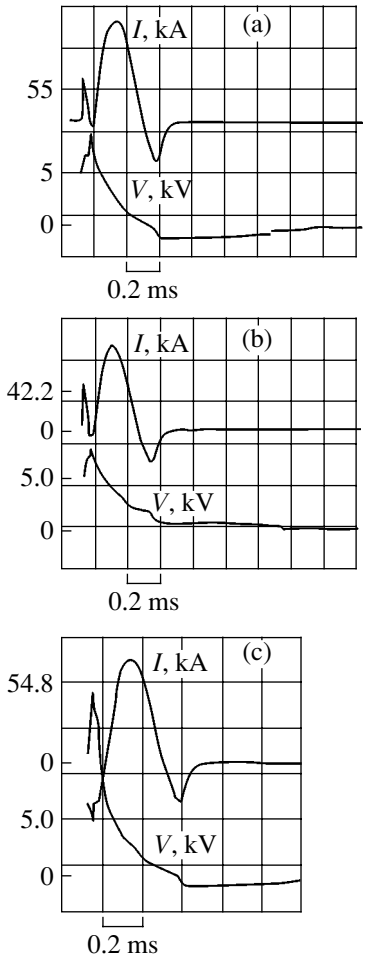

Fig. 2. The oscillograms of current and voltage measured during the explosion of (a) tantalum, (b) tungsten, and (c) molybdenum wires in water at V = 5.0 kV.

In summary, the explosion of a metal wire in water is accompanied by exothermal chemical reaction with evolution of a large amount of heat. As a result, the reaction products possess a high temperature and are subject to thermal ionization. This results in the formation of a dense plasma of the products of exothermal chemical reaction. The plasma exhibits polarization and the system acquires an energy on the order of or greater than that initially stored in the capacitor bank. Numerical integration of the current and voltage oscillograms gives values of energy comparable with those acquired by the system upon the wire explosion.

Acknowledgments. The author is grateful to Z. Saralidze, V. Berezhiani, and I. Murusidze for constructive criticism and fruitful discussions.

This study was supported by the International Scientific-Technological Center, grant no. G-663.

REFERENCES

1. E. V. Krivitskiĭ, *The Dynamics of Electrical Explosion in Fluid* (Naukova Dumka, Kiev, 1986).
2. V. P. Kortkhonjia, M. O. Mdivnishvili, and M. I. Taktakishvili, Zh. Tekh. Fiz. **69** (4), 41 (1999) [Tech. Phys. **44**, 387 (1999)].
3. V. P. Kortkhonjia and M. O. Mdivnishvili, Pis'ma Zh. Tekh. Fiz. **25** (13), 10 (1999) [Tech. Phys. Lett. **25**, 509 (1999)].
4. http://www.fpl.gpi.ru/Zvenigorod/XXVIIIPT/en/15e-Sedoi.doc.
5. *Exploding Wires*, Ed. by W. Chace and H. Moore (New York, 1962; Mir, Moscow, 1965).
6. G. A. Mesyats, *Generation of High-Power Nanosecond Pulses* (Sov. Radio, Moscow, 1974), p. 90.
7. *Concise Chemical Encyclopedia* (Sov. Éntsiklopediya, Moscow, 1961–1967).
8. F. Chen, *Introduction to Plasma Physics* (Plenum, New York, 1984; Mir, Moscow, 1987).
9. K. B. Abramova, N. A. Zlatin, and B. P. Peregud, Zh. Éksp. Teor. Fiz. **69**, 2005 (1975) [Sov. Phys. JETP **42**, 1019 (1975)].

Translated by P. Pozdeev

Technical Physics Letters, Vol. 29, No. 10, 2003, pp. 801–803. Translated from Pis'ma v Zhurnal Tekhnicheskoĭ Fiziki, Vol. 29, No. 19, 2003, pp. 21–25.

Estimating Hydrodynamical Drag of a Seagoing Vessel by Data of Remote Trajectory Measurements

A. S. Devyatisilny, V. M. Dorozhko, and V. M. Grinyak

Institute of Automation and Control Processes, Far East Division of the Russian Academy of Sciences, Vladivostok, Russia

e-mail: devyatis@iacp.dvo.ru

Received March 31, 2003

Abstract—A method for determining the hydrodynamical drag of a seagoing vessel using the data of a coastal two-coordinate surveillance radar is described and verified. The results of large-scale numerical simulation are presented. © *2003 MAIK "Nauka/Interperiodica".*

Introduction. Recently [1], we described a method of determining the hydrodynamical drag of a seagoing vessel by the method of inertial travel. As confirmed by the results of full-scale experiments, this approach allows the drag as a function of the vessel velocity to be studied and the seaforming properties of various objects to be compared using the results of processing of a single trajectory of inertial motion. The method was verified using the data of trajectory measurements obtained by standard onboard facilities (towed logs).

However, it is important in practice to solve the same problem by alternative methods based on external sources of information such as coastal 2D surveillance radars determining the distance to an object and its azimuth. The value of this approach is determined by the prospects of the development of navigation and service functions of modern coastal traffic control systems. In particular, data acquisition systems are developed for solving problems related to the online monitoring of the hull state and the load of a vessel.

This study was aimed at numerical verification of a new, practically significant method of determining the drag of seagoing vessels.

Formulation of the problem. The problem consists in evaluating the velocity and acceleration of a vessel and, eventually, the drag as a function of the velocity, from a body of data on the inertial travel of the vessel coordinates measured by a coastal 2D surveillance radar.

Let us introduce a Cartesian coordinate system $0xy$, in which the radar data are expressed as follows:

$$\begin{aligned} z_r(t_k) &= \sqrt{x^2(t_k) + y^2(t_k)} + \xi_r, \\ z_\varphi(t_k) &= \arctan(x(t_k)/y(t_k)) + \xi_\varphi. \end{aligned} \tag{1}$$

Here, $z_\varphi(t_k)$ and $z_r(t_k)$ are the azimuth and distance determined at discrete moments of time t_k; $x(t_k)$ and $y(t_k)$ are the vessel coordinates; and ξ_r and ξ_φ are the instrumental measurement errors.

Since the free inertial motion trajectory is a straight line, the problem can be formulated as one-dimensional and, hence, system (1) can be reduced to a single equation:

$$d(t_k) = f(z_r, z_\varphi, t_k), \qquad k = \overline{1, n}, \tag{2}$$

where $d(t_k)$ is interpreted as the result of a "new" measurement of the distance traveled by the vessel from the start point of rectilinear inertial motion, $f(z_r, z_\varphi, t_k)$ is the function obtained by linear (in the $0xy$ plane) regression of the results of radar measurements, and n is the total number of measurements.

The data array $\{d(t_k)\}_{k = \overline{1, n}}$ can be processed as described previously [1], provided that model (2) is supplemented by a relation (considered as known) of the type [2]

$$r_d = -(1 + n_r)\ddot{d}, \tag{3}$$

where r_d is the specific (per unit object mass) hydrodynamical drag, d the inertial travel length, and n_r is a correction taking into account nonstationary character of the motion and the particular vessel geometry.

Despite the evident similarity of the above problem to that studied previously [1], the different character of the measured data (2D trajectory measurements instead of 1D travel distance and velocity determinations) requires adequate verification and adaptation of the method of problem solution under new conditions. This will be done within the framework of a numerical experiment.

1063-7850/03/2910-0801$24.00 © 2003 MAIK "Nauka/Interperiodica"

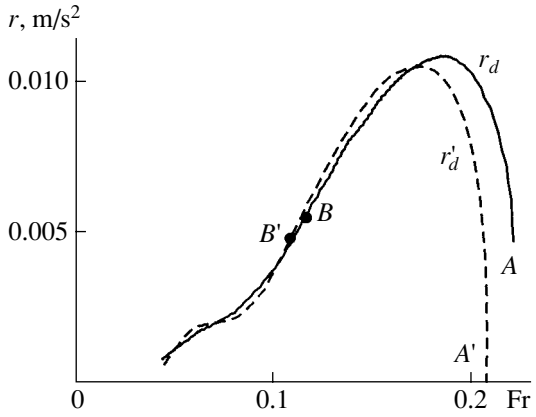

Fig. 1.

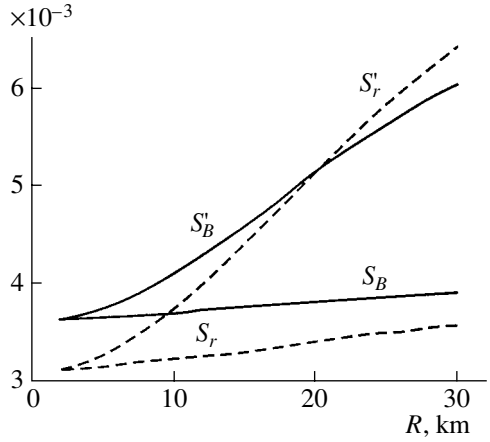

Fig. 2.

Experimental results. The results presented below were obtained using the concept of large-scale computer simulation. This includes (i) the construction of a model of the object motion based on the results of onboard measurements (essentially, the results presented in [1]) and (ii) the computer simulation of situations encountered in remote radar observations.

Let us consider the case of a single coastal radar of the Raytheon type characterized by the range (ξ_r) and azimuthal (ξ_φ) errors uniformly distributed within the intervals [–6.25 m; 6.25 m] and [–0.06°; 0.06°], respectively, and by a radar antenna scan period of 3 s. In this large-scale experiment, we will use (as in [1]) the results of full-scale measurements performed for the real cargo ship Vitus Bering.

The model parameters are as follows: vessel length along the waterline, L = 150 m; volume displacement, V_{vol} = 20200 m^3; initial velocity, v_1 = 8.2 m/s; inertial motion duration, 1500 s; total number of measurements, n = 501; the correction n_r is introduced according to the results of approximation of a typical dependence on the vessel velocity, length, and volume displacement [2]

$$n_r = b_0 + b_1 v^1 + b_2 v^2,$$

where

$$b_0 = 0.2017 - 0.0321\psi + 0.0010\psi^2,$$

$$b_1 = (-0.4871 + 0.1193\psi - 0.0034\psi^2)/\sqrt{(gL)},$$

$$b_2 = (5.9608 - 1.3284\psi + 0.0679\psi^2)/(gL),$$

$$\psi = L/V_{\text{vol}}^{1/3},\ g = 9.81\ \text{m/s}^2.$$

Figure 1 shows the plots of the estimated specific drag versus relative velocity (in terms of the Froude number $\text{Fr} = v/\sqrt{gL}$) for the inertial motion of the vessel under consideration. The solid curve r_d (considered as the base) corresponds to the specific drag determined using the towed lag. The dashed curve r'_d represents the worst statistical realization of Eq. (3). The points A and A' correspond to the start of the inertial travel, and the coordinates of points B and B' on the (Fr, r_d) plane can serve as the measures for a comparison of the seaforming properties of various vessels [1]. As can be seen, the values of the specific drag r'_d determined from the radar data are somewhat different from the base values.

We have analyzed the problem so as to characterize the discrepancy quantitatively, as dependent on the vessel trajectory parameters (the distance and the direction of motion). The error of the specific drag determination was characterized by the value of $rms(\delta r_d) = \|\delta r_d\|/(\sqrt{n}/r_d(B))$, where $\|\delta r_d\| = \|r_d - r'_d\|$ is the Euclidean norm of the vector of difference of the specific drags calculated using the lag and radar data, $r_d(B)$ is the drag at point B, and n is the number of determinations. Proceeding from physical notions, the measure of uncertainty in determining point B was taken in the form $\delta\text{Fr}_B = (\text{Fr}_B - \text{Fr}'_B)/\text{Fr}_B$, where Fr_B and Fr'_B are the Froude numbers at points B and B' (i.e., determined from the lag and radar measurements), respectively.

Figure 2 shows the plots of $S_r = M[rms(\delta r_d]$ (dashed curve) and $S_B = M[\delta\text{Fr}_B]$ (solid curve) as functions of the distance from the radar to the inertial travel start point. Here, $M[*]$ is the operator of averaging over the data of the multiply repeated experiment, performed using the orthogonal Coiflet wavelet packet (coif4) with a four-level decomposition. The values of S_r and S_B correspond to the most favorable vessel trajectory, whereby the direction of motion coincides with the azimuthal direction to the radar, while the values of S'_r

and S'_B correspond to the must unfavorable case, when the direction of motion at the inertial travel start point is perpendicular to the azimuthal direction. Taking into account the statistical character of $rms(\delta r_d)$ and $\delta \mathrm{Fr}_B$, the average values were supplemented with the corresponding mean square deviations from the S_r, S'_r, S_B, and S'_B values: $\sigma(\delta r_d) \approx 0.002$ m/s^2, $\sigma'(\delta r_d) \approx 0.003$ m/s^2, $\sigma(\delta \mathrm{Fr}_B) \approx 0.08$, and $\sigma'(\delta \mathrm{Fr}_B) \approx 0.09$. These estimates of accuracy under the conditions of single-radar measurements are not merely quite acceptable but are also rather promising in view of the good prospects for multiposition observations. On the whole, the above results show that the proposed method [1] is well adapted to the situation of remote radar observations.

REFERENCES

1. A. S. Devyatisilny, V. M. Dorozhko, and V. M. Grinyak, Zh. Tekh. Fiz. **73** (2), 38 (2003) [Tech. Phys. **48**, 172 (2003)].
2. *Ship-Building Theory: A Handbook*, Vol. 1: *Fluid Mechanics, Ship Drag, and Ship Propulsors*, Ed. by Ya. I. Voĭtkunskiĭ (Sudostroenie, Leningrad, 1985).

Translated by P. Pozdeev

Technical Physics Letters, Vol. 29, No. 10, 2003, pp. 804–805. Translated from Pis'ma v Zhurnal Tekhnicheskoĭ Fiziki, Vol. 29, No. 19, 2003, pp. 26–30.

New Hydrogen Donors in Germanium

Yu. M. Pokotilo, A. N. Petukh, and V. V. Litvinov

Belarussian State University, Minsk, Belarus

e-mail: pokotilo@bsu.by

Received April 11, 2003

Abstract—The electrical properties of *n*-type germanium single crystals irradiated with protons were studied by measuring capacitance–voltage characteristics. The thermal treatment of irradiated samples at 200–300°C leads to the formation of highly mobile shallow donor centers. The coefficient of diffusion of these donors is equal to that of atomic hydrogen with allowance for capture on traps. It is concluded that atomic hydrogen plays the role of a shallow donor in germanium. © *2003 MAIK "Nauka/Interperiodica"*.

In recent years, hydrogen has been the most extensively studied impurity in semiconductor lattices [1]. In silicon, both the precipitation of hydrogen and its interaction with intrinsic defects leads to the formation of various types of both oxygen-containing [2] and oxygen-free [3] donor centers. In germanium, hydrogen-containing donors have been known so far only in the form of H–O complexes [4]. The behavior of hydrogen in commercial single crystal germanium is still insufficiently studied, although this knowledge would be of interest from the standpoint of production technology and radiation stability of germanium detectors. In this context, we have studied the electrical properties of germanium p^+–n structures irradiated with protons.

The experiments were performed on germanium p^+–n structures with a sharp alloyed (indium) interface and a base layer thickness of d_0 = 100–200 μm. The *n*-type base material was commercial single crystal germanium doped with antimony to $N_d = (1–2) \times 10^{13}$ cm^{-3}. Both the p^+–n structures (from the base side) and the control *p*-Ge and *n*-Ge plates (with ρ = 25–45 Ω cm) were irradiated with 300-keV protons (H^+). The mean projected range of H^+ ions with this energy in germanium amounts to 3 μm. The ion flux density was 1×10^{15} cm^{-2}.

The concentration of shallow donors in the base region of the p^+–n structures was determined by measuring the room-temperature capacitance–voltage characteristics. The deep levels were studied by deep-level transient spectroscopy (DLTS) in the temperature range from 20 to 300 K. The conductivity type was checked by thermal probe.

Irradiation of the rear side (*n*-type material) of the p^+–n structures and the control plates led to the formation of *p*-type layers to within the H^+ ion range, which was related to the formation of radiation defects predominantly of the acceptor type. However, a short (~30 min) heating of the samples to 200–250°C resulted in the conductivity type conversion ($p \longrightarrow n$) in the irradiated regions of both *n*-Ge and *p*-Ge. During further isothermal annealing, the region of excess electron density spreads beyond the irradiated layer and excess electrons are found in the vicinity of the p^+-n junction (i.e., at a depth of ~100 μm). Figure 1 shows the depth profiles of the electron density n within a 30-μm-thick layer at the p^+–n interface in various stages of isothermal annealing at 200°C. As can be seen, the excess electron density both in the initial state and in the irradiated layer of the structure increases with the duration of annealing, which is indicative of the formation of excess donor centers. The results of DLTS measurements showed that the ionization energy of these defects is $\Delta E < E_c - 0.0135$ eV.

Since the concentration of hydrogen in a 3-μm-thick layer implanted at a proton flux density of 1×10^{15} cm^{-2}

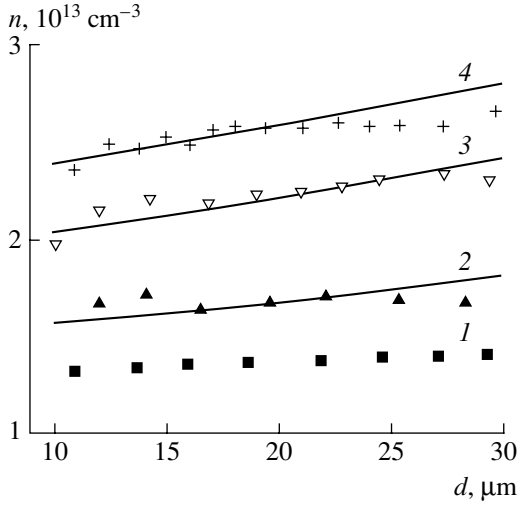

Fig. 1. Depth profiles of the electron density in the hydrogen implanted base of a germanium diode in the course of isothermal (200°C) annealing for various times t = 0 (*1*), 1720 (*2*), 3400 (*3*), and 4960 min (*4*). Solid curves show the results of calculations using Eq. (1).

is 4–5 orders of magnitude higher than the density of electrons measured in the base, the diffusion characteristics were quantitatively estimated using a solution of the Fick law in the approximation of diffusion from undepleted source [1]:

$$N_H = n - N_d = N_0[1 - \mathrm{erf}(x/(2\sqrt{Dt}))]. \quad (1)$$

Here, N_0 is the surface concentration of atomic hydrogen, $x = d_0 - d$ is the coordinate measured from the rear contact, t is the diffusion time, and D is the diffusion coefficient. An analysis of the experimental data in Figs. 1 and 2 (the latter presenting the dynamics of donor formation at a fixed point in the base layer (at d = 20 μm) in terms of Eq. (1) showed that a satisfactory agreement between the experimental values of $N_H(x, t)$ and the calculated curves for the annealing temperatures of 200 and 250°C is achieved with the diffusion coefficients $D = 1.5 \times 10^{-10}$ and 8×10^{-10} cm^2/s and the surface concentrations $N_0 = 4.2 \times 10^{13}$ and 6.6×10^{14} cm^{-3}, respectively. These D values are about three orders of magnitude lower than those calculated for atomic hydrogen (2.6×10^{-7} cm^2/s at 200°C and 6.2×10^{-7} cm^2/s at 250°C) using an expression for the temperature dependence of the diffusion coefficient determined by mass spectrometry near the melting point [5].

On the other hand, the obtained estimates of the diffusion coefficient agree in the order of magnitude with the diffusion coefficient of atomic hydrogen at a temperature of 300–350°C, which were determined from experimental data on the passivation of defects in germanium treated in a hydrogen plasma [6]. Our results in combination with the data from [6], presented in the inset in Fig. 2, can be described by the following relationship of the activation type:

$$D = 6.43 \times 10^{-3} \exp(-0.72\ \mathrm{eV}/kT)\ [\mathrm{cm}^2/\mathrm{s}]. \quad (2)$$

It can be suggested that the diffusion of atomic hydrogen in our case is also limited by trapping and should be described by an effective diffusion coefficient decreased by a factor of [H]/[H_r], where [H] is the free hydrogen concentration and [H_r] is the total concentrations of implanted hydrogen [1]. According to [7], the role of traps can be played by oxygen atoms and dimers in the lattice cites, which form donor states upon trapping hydrogen. However, the H–O complexes are stable only below 150°C [4]. The concentration of oxygen dimers in commercial germanium at 250°C is only ~10^{11} cm^{-3} [8], while the concentration of donors observed at this temperature near the irradiated sample surface amounts to 6.6×10^{14} cm^{-3}. Thus, the observed hydrogen-containing donors do not involve oxygen.

According to the Hall model [6], the role of traps can also be played by hydrogen atoms proper, through the formation of electrically inactive low-mobility molecular hydrogen. In this case, the diffusion coefficient of hydrogen also decreases approximately by three orders of magnitude in the temperature intervals studied, while the surface concentration N_0 of atomic hydrogen virtually coincides with that reported in [6]. Taking this into account, we may conclude that hydrogen atoms can play the role of donors in the germanium lattice.

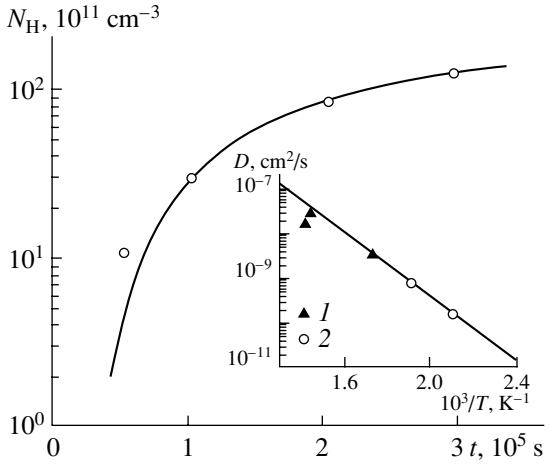

Fig. 2. A plot of the concentration of donors N_H formed at a depth of 20 μm from the *p–n* junction of a germanium diode versus the duration of isothermal (200°C) annealing. Symbols present the experimental data; the solid curve shows the results of calculations using Eq. (1). The inset shows plots of the diffusion coefficient of (*1*) hydrogen (data from [6]) and (*2*) donor centers in germanium versus reciprocal temperature.

REFERENCES

1. S. J. Pearton, J. W. Corbett, and M. Stavola, *Hydrogen in Crystalline Semiconductors* (Springer-Verlag, Berlin, 1992).
2. B. N. Mukashev, Ch. A. Abdulin, and Yu. V. Gorelkinskiĭ, Usp. Fiz. Nauk **170** (2), 143 (2000).
3. V. P. Markevich, M. Suezawa, and K. Sumino, J. Appl. Phys. **76**, 7347 (1994).
4. E. Haller and W. L. Hansen, Adv. Phys. **30** (9), 93 (1981).
5. R. C. Frank and J. E. Thomas, J. Phys. Chem. Solids **16**, 144 (1960).
6. R. N. Hall, IEEE Trans. Nucl. Sci. **NS-21**, 260 (1974).
7. P. Deak, B. Schröder, A. Annen, and A. Scholtz, Phys. Rev. B **48**, 1924 (1993).
8. V. V. Litvinov, L. I. Murin, L. Lindström, *et al.*, Fiz. Tekh. Poluprovodn. (St. Petersburg) **35**, 900 (2001) [Semiconductors **35**, 864 (2001)].

Translated by P. Pozdeev

Technical Physics Letters, Vol. 29, No. 10, 2003, pp. 806–809. Translated from Pis'ma v Zhurnal Tekhnicheskoĭ Fiziki, Vol. 29, No. 19, 2003, pp. 31–39.

Dependence of the Transient Process Duration on the Accuracy of Determination in Dynamical Systems with Quasiperiodic Behavior

A. A. Koronovskiĭ

State Scientific Center "College," Saratov State University, Saratov, Russia

e-mail: alkor@cas.ssu.runnet.ru

Received April 10, 2003

Abstract—A method for determining the transient process duration in a dynamical system with quasiperiodic behavior is described. An analytical expression is obtained that relates the average transient process duration to the accuracy of determination of this parameter. *© 2003 MAIK "Nauka/Interperiodica".*

Any time series generated by a dynamical system contains an initial part, called a transient process, in which the system behavior is different from that exhibited by the same system as $t \longrightarrow \infty$. As a rule, the period of time corresponding to the transient process is insignificant (within ten or several tens of the characteristic time scales of the system) and is not taken into consideration, all attention being concentrated on the asymptotic (established) regimes. However, in some cases, the transient processes are worth studying for various reasons. First, an analysis of the transient process can sometimes provide valuable information about the system and its dynamics (important, e.g., for reconstruction of a system from its time series [1, 2]), which cannot be extracted from an analysis of the established regimes. Second, the transient process can be very long [3, 4], representing an essential part of the system dynamics. Moreover, in cases when the dynamical system is modeling a real physical system operating in a pulsed regime, the entire system dynamics represents a transient process. Finally, the transient process can be of independent interest as a physical phenomenon obeying certain laws [5, 6]. For example, the so-called transient chaos extensively studied in recent years (see, e.g., [7–12] and references therein) is essentially a transient process.

Thus, transients in dynamical system bear some information about these systems and obey certain laws. Since, formally speaking, the imaging point in the phase space never reaches an attractor within a finite period of time and only asymptotically tends to this attractor as $t \longrightarrow \infty$, the transient process duration depends on the accuracy ε of determination of the time when this process is considered terminated.

Recently, a method for determining the transient process duration has been proposed for dynamical systems exhibiting periodic behavior and applied to several maps [13–16]. Dependence of the process duration on the characteristics of the attractor, the accuracy of determination, and the initial conditions was studied and the mechanisms responsible for the possible complication of this dependence were established. All the results obtained in [13–16] are also applicable to dynamical systems with discrete time: using the Poincaré section procedure, any flow system can be reduced to a map with the dimension lower by one than that of the initial dynamical system [17–20].

In the case of a system exhibiting irregular behavior (featuring quasiperiodic or chaotic oscillations), the situation is complicated because the number of attractor points (or the number of points in the Poincaré section for a flow system) becomes infinite [21, 22]. The aim of this study is to consider the transients of dynamical systems occurring in a regime of quasiperiodic oscillations. For this purpose, we will consider a two-dimensional dynamical system with discrete time known as the Zaslavsky map [23–26],

$$\begin{aligned} x_{n+1} &= x_n + \Omega + \frac{k}{2\pi}\sin(2\pi x_n) + dy_n, \mod 1, \\ y_{n+1} &= dy_n + \frac{k}{2\pi}\sin(2\pi x_n), \end{aligned} \tag{1}$$

with the control parameters $d = 0.3$, $k = 0.5$, and $\Omega = 0.22$ selected so that the system would occur in the state of quasiperiodic oscillations. Figure 1 shows a phase portrait of system (1) for the set of control parameters indicated.

The transient process duration will be determined by analogy with the case of a system occurring in the state of chaotic oscillations [22]. According to this, the region of initial conditions containing the attractor is covered with a lattice of period (step) ε. Then, an initial point (x_0, y_0) point in the attraction basin is selected and the map (1) is iterated a sufficiently large number of times M (so as to exceed the maximum transient pro-

1063-7850/03/2910-0806$24.00

cess duration T_{max}).[1] After accomplishing M iterations (i.e., when the transient process can be considered as terminated), we begin to count the number of cells visited by the imaging point during the iterative procedure. The cells covering the attractor points will be referred to as the attractor cells [22]. The iterative procedure has to involve a sufficiently large number of steps, so that the number of attractor points covered by the attractor cells is as large as possible. After termination of the iterative procedure, we obtain a basis array of such attractor cells. Once the cells belonging to the attractor are known, the transient process duration can be determined as follows: if the initial point (x_0, y_0) falls within an attractor cell at an iteration step corresponding to K discrete time units, the transient process duration determined for the given initial condition to within a preset accuracy ε is K. Obviously, correct determination of the transient process duration requires finding a possibly large number of attractor cells. The number of iterations required to completely cover the attractor (or the attractor coverage time T_c) strongly depends on the accuracy ε of determination of the transient process duration.

Now let us study how the transient process duration $T(\varepsilon)$, determined for the same control parameters and initial conditions, depends on the ε value. For periodic regimes in one-dimensional maps, the relation between the transient process duration and the accuracy ε is as follows [16]:

$$T_\varepsilon(x_0) = T_{\varepsilon 1}(x_0) + \tau \log_{|\mu|}\left(\frac{\varepsilon}{\varepsilon_1}\right), \qquad (2)$$

where $T_\varepsilon(x_0)$ and $T_{\varepsilon 1}(x_0)$ are the transient process durations determined with different accuracies ε and ε_1, respectively, for the same initial conditions x_0; τ is the period of oscillations ($\tau = 1$ for an immobile stable point, $\tau = 2$ for a cycle of period 2, etc.); and μ is the multiplicator of a stable cycle. The latter quantity is determined as a product of the derivatives of functions $f(x)$ calculated at the points x_i^0 ($i = \overline{1, \ldots, \tau}$) of the given stable cycle:

$$\mu = \prod_{i=1}^{\tau} f'(x_i^0). \qquad (3)$$

Note that, owing to stability of the cycle with period τ, the absolute value of the corresponding multiplicator μ is smaller than unity.

An expression analogous to relation (2), obtained by averaging over all possible initial conditions, describes the average transient process duration $\langle T \rangle$ on the accuracy of its determination:

$$\langle T_\varepsilon \rangle = \langle T_{\varepsilon 1} \rangle + \tau \log_{|\mu|}\left(\frac{\varepsilon}{\varepsilon_1}\right). \qquad (4)$$

[1] In this study, $M = 10^4$.

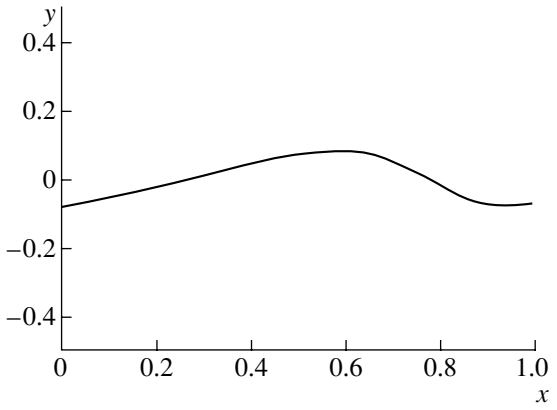

Fig. 1. A quasiperiodic attractor on the plane of initial conditions (x_0, y_0) for the Zaslavsky map (1) with the control parameters $d = 0.3$, $k = 0.5$, and $\Omega = 0.22$.

Relation (4) is also applicable to two-dimensional (and, in the general case, to multidimensional) maps exhibiting periodic dynamics [27]. In the case of two-dimensional maps, the periodic cycles are characterized by two multiplicators, μ_1 and μ_2, which are eigenvalues of the monodromy matrix

$$\mathbf{M} = \prod_{i=1}^{\tau} \begin{pmatrix} \frac{dx_{n+1}}{dx_n} & \frac{dy_{n+1}}{dx_n} \\ \frac{dx_{n+1}}{dy_n} & \frac{dy_{n+1}}{dx_n} \end{pmatrix}\Bigg|_{(x_i^0, y_i^0)}, \qquad (5)$$

calculated for the elements (x_i^0, y_i^0) of the cycle of period τ. A relation of type (2) for the two-dimensional map involves a multiplicator with the maximum absolute value: $\mu = \max(|\mu_1|, |\mu_2|)$.

In cases when the map exhibits a quasiperiodic behavior, relation (2) cannot be used, because the concept of multiplier is inapplicable to nonperiodic regimes. In such cases, the stability of attractors is characterized by the spectrum of Lyapunov exponents λ_i (for details, see [26]). The Lyapunov exponents can be used for the description of both periodic and nonperiodic attractors. For a periodic cycle of period τ, the Lyapunov exponent is related to the corresponding multiplicator by the formula [26]

$$\lambda = \frac{1}{\tau}\ln|\mu|. \qquad (6)$$

Accordingly, relation (2) for a periodic regime can be written in these terms as

$$\langle T_\varepsilon \rangle = \langle T_{\varepsilon 1} \rangle + \frac{\ln(\varepsilon/\varepsilon_1)}{\lambda}, \qquad (7)$$

where λ is the maximum negative Lyapunov exponent (i.e., that possessing the minimum absolute value), cor-

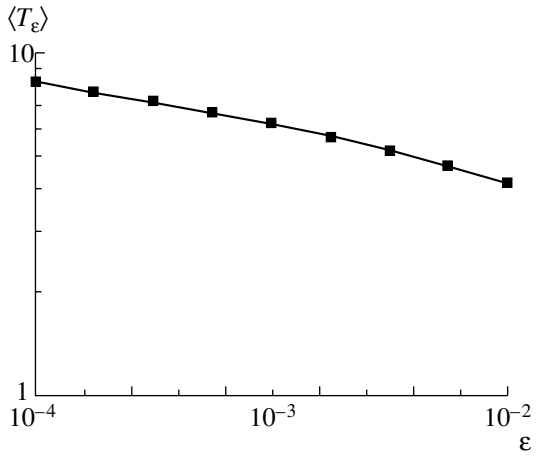

Fig. 2. A double logarithmic plot of the average transient process duration $\langle T_\varepsilon \rangle$ versus determination accuracy ε for a Zaslavsky map in the regime of quasiperiodic oscillations (the control parameters are the same as in Fig. 1). Black squares represent the values of $\langle T_\varepsilon \rangle$ determined by numerical calculation; solid curve is described by formula (7).

responding to the maximum (in absolute value) multiplicator of the cycle of period τ.

Now, we can apply relation (7) to description of the average transient process duration as a function of the accuracy ε for the maps exhibiting quasiperiodic oscillations. Indeed, all assumptions concerning the system behavior used in deriving this relation [16, 27] are valid: there are two directions in the vicinity of the attractor, in which the system is characterized by the corresponding Lyapunov exponent, and termination of the transient process with a preset accuracy ε is determined by the maximum negative Lyapunov exponent.

The above considerations are illustrated by Fig. 2 showing a plot of the average transient process duration $\langle T_\varepsilon \rangle$ as a function of the determination accuracy ε for a map exhibiting quasiperiodic oscillations with the control parameters indicated above. Since the basin of attraction for an attractor in the Eno map is the entire (x, y) plane and a change in the x value is determined as mod1, the average transient process duration was determined by averaging $T_\varepsilon(x_0, y_0)$ over the initial conditions within a region bounding the quasiperiodic attractor ($x_0 \in [0; 1]$, $y_0 \in [-0.5; 0.5]$). The $\langle T_{\varepsilon 1} \rangle$ value was taken equal to the average transient process duration determined with an accuracy of $\varepsilon_1 = 10^{-2}$ ($\langle T_{10^{-2}} \rangle = 4.13$). The spectrum of Lyapunov exponents λ_1 and λ_2 was numerically calculated using renormalization of the perturbation vectors and their orthogonalization by the Gram–Schmidt method [26, 28]. The moduli of the perturbation vectors were taken equal to $e = 10^{-4}$ and the total number of iterations was $N = 10^6$. For the given values of parameters of the quasiperiodic process and the calculation method, the Lyapunov exponents are $\lambda_1 = 0.0002$ and $\lambda_2 = -1.2031$. The major Lyapunov exponent λ_1 is responsible for the quasiperiodic dynamics, while the second exponent λ_2 (accounting for the phase volume contraction and the transient process duration) enters as λ into relation (7). As can be seen from Fig. 2, the proposed relation (7) fits with a good accuracy the plot of the transient process duration versus ε for the given system exhibiting a quasiperiodic behavior.

In summary, we have described a method for determining the transient process duration with a preset accuracy ε for a dynamical system in the regime of quasiperiodic oscillations. For this system, we proposed an analytical relation describing the average transient process duration as a function of ε.

Acknowledgments. The author is grateful to A.E. Khramov and A.V. Starodubov for their help in work and for fruitful discussions.

This study was supported by the Russian Foundation for Basic Research (project no. 01-02-17392) and by the Scientific-Education Center "Nonlinear Dynamics and Biophysics" at the Saratov State University (grant REC-006 from the U.S. Civilian Research and Development Foundation for the Independent States of the Former Soviet Union).

REFERENCES

1. B. P. Bezruchko, T. V. Dikanev, and D. A. Smirnov, Izv. Vyssh. Uchebn. Zaved., Prikl. Nelineĭnaya Dinam. **9** (3), 3 (2001).
2. B. P. Bezruchko, T. V. Dikanev, and D. A. Smirnov, Phys. Rev. E **64**, 036210 (2001).
3. C. Grebogi, E. Ott, and J. A. Yorke, Phys. Rev. Lett. **50**, 935 (1983).
4. L. Zhu, A. Raghu, and Y.-C. Lai, Phys. Rev. Lett. **86**, 4017 (2001).
5. V. V. Astakhov *et al.*, Radiotekh. Élektron. (Moscow) **38**, 291 (1993).
6. É. V. Kal'yanov, Pis'ma Zh. Tekh. Fiz. **26** (15), 26 (2000) [Tech. Phys. Lett. **26**, 656 (2000)].
7. C. Grebogi, E. Ott, and J. A. Yorke, Physica D **7**, 181 (1983).
8. H. E. Nusse and J. A. Yorke, Physica D **36**, 137 (1989).
9. I. M. Janosi and T. Tél, Phys. Rev. E **49**, 2756 (1994).
10. M. Dhamala, Y.-C. Lai, and E. J. Kostelich, Phys. Rev. E **64**, 056207 (2001).
11. M. Dhamala, Y.-C. Lai, and E. J. Kostelich, Phys. Rev. E **61**, 6485 (2000).
12. A. A. Koronovskiĭ, I. S. Rempen, D. I. Trubetskov, and A. E. Khramov, Izv. Ross. Akad. Nauk, Ser. Fiz. **66**, 1754 (2002).
13. A. A. Koronovskiĭ, D. I. Trubetskov, A. E. Khramov, and A. E. Khramova, Dokl. Akad. Nauk **383**, 322 (2002) [Dokl. Phys. **47**, 181 (2002)].
14. A. A. Koronovskiĭ, D. I. Trubetskov, A. E. Khramov, and A. E. Khramova, Izv. Vyssh. Uchebn. Zaved., Radiofiz. **45**, 880 (2002).

15. A. A. Koronovskiĭ and A. E. Khramov, Pis'ma Zh. Tekh. Fiz. **28** (15), 61 (2002) [Tech. Phys. Lett. **28**, 648 (2002)].
16. A. A. Koronovskiĭ, A. E. Khramov, and I. A. Khramova, Izv. Vyssh. Uchebn. Zaved., Prikl. Nelineĭnaya Dinam. **11**, 1 (2002).
17. M. Hénon, Physica D **5**, 412 (1982).
18. Z. Kaufmann and H. Lustfeld, Phys. Rev. E **64**, 055206 (2001).
19. H. G. Schuster, *Deterministic Chaos* (Physik-Verlag, Weinheim, 1984; Mir, Moscow, 1988).
20. G. P. Bystraĭ and S. I. Studentok, Izv. Vyssh. Uchebn. Zaved., Prikl. Nelineĭnaya Dinam. **10** (6), 24 (2002).
21. A. A. Koronovskiĭ, A. V. Starodubov, and A. E. Khramov, Izv. Vyssh. Uchebn. Zaved., Prikl. Nelineĭnaya Dinam. **10** (5), 25 (2002).
22. A. A. Koronovskiĭ, A. V. Starodubov, and A. E. Khramov, Pis'ma Zh. Tekh. Fiz. **29** (8), 32 (2003) [Tech. Phys. Lett. **29**, 323 (2003)].
23. G. M. Zaslavsky, *Chaos in Dynamical Systems* (Nauka, Moscow, 1984; Harwood, Chur, 1985).
24. G. M. Zaslavskiĭ, *Statistical Irreversibility in Nonlinear Systems* (Nauka, Moscow, 1970).
25. R. Z. Sagdeev, D. A. Usikov, and G. M. Zaslavsky, *Nonlinear Physics: from the Pendulum to Turbulence and Chaos* (Harwood, Chur, 1988); Russian original: G. M. Zaslavsky and R. Z. Sagdeev, *Introduction to Nonlinear Physics* (Nauka, Moscow, 1988).
26. S. P. Kuznetsov, *Dynamical Chaos* (Fizmatlit, Moscow, 2001).
27. G. B. Astaf'ev, A. A. Koronovskiĭ, A. E. Khramov, and A. E. Khramova, Izv. Vyssh. Uchebn. Zaved., Prikl. Nelineĭnaya Dinam. (2003, in press).
28. G. Benettin, L. Galgani, A. Giorgilli, and J.-M. Strelcyn, Meccanica **15**, 9 (1980).

Translated by P. Pozdeev

Technical Physics Letters, Vol. 29, No. 10, 2003, pp. 810–812. Translated from Pis'ma v Zhurnal Tekhnicheskoĭ Fiziki, Vol. 29, No. 19, 2003, pp. 40–47.

Controlled Superconductivity of a Semiconductor–Superconductor Eutectic Composition

G. I. Isakov

Institute of Physics, National Academy of Sciences of Azerbaijan, Baku, Azerbaijan

e-mail: gudrat@physics.ab.az

Received April 11, 2003

Abstract—The electrical properties of a GaSb–V_2Ga_5 eutectic composition have been studied. This system comprises long oriented whiskers of a superconducting V_2Ga_5 phase formed by directed crystallization in a semiconducting GaSb matrix. The properties of samples can be controlled by varying the angle between the directions of electric current and whiskers. The observed features of the temperature dependence of the resistivity and the possibility of controlling the properties of the eutectic system are explained by the formation of discrete superconducting regions comprising linked Josephson junctions of the superconductor–semiconductor–superconductor type (*S*–*Sm*–*S*–*Sm*–*S*…), whiskers consisting of linked microscopic bridges (*S*–*S*'–*S*–*S*'–*S*…), and infinite clusters comprising combinations of the above two components (*S*–*S*'–*S*–*Sm*–*S*–*S*'–*S*…). © *2003 MAIK "Nauka/Interperiodica".*

Introduction. Developing methods of control over the properties of materials is the basic problem studied by applied physics and encountered in scientific and industrial instrument building. Previously [1], the possibility of controlling the tensometric properties of a eutectic composition of the semiconductor–metal type was reported. In recent years, much attention has been devoted to studying the dependence of the electrical properties of high-temperature superconductors on the angle of misorientation in the Josephson junctions [2–4].

Among the Josephson junctions of various types, of special interest are systems of the superconductor–semiconductor–superconductor type (*S*–*Sm*–*S*). This interest is related primarily to the possibility of controlling the properties of the semiconductor layer by doping and by applying electric and magnetic fields [5–8].

In an early work [9], the Josephson effect was observed in a semiconductor–superconductor eutectic composition. This Letter presents original data on the superconducting properties of a GaSb–V_2Ga_5 composition of this type and on the possibility of controlling these properties by various methods. The superconducting phase (V_2Ga_5) accounts for 4 vol % of the GaSb–V_2Ga_5 eutectic studied. In the course of directed crystallization, this superconducting phase forms long oriented whiskers in the GaSb matrix [10]. The results of this study can be useful in developing both low-and high-temperature superconductors and related Josephson structures.

Experimental results. The temperature dependence of the resistivity ρ of a GaSb–V_2Ga_5 eutectic composition was measured for various angles between the directions of electric current (*I*) and whiskers (*X*). For this purpose, the samples were cut in the form of rectangular parallelepipeds so that the angle between the direction of whisker growth (*X*) and the sample height (*h*) had the values α = 0°, 15°, 30°, 45°, 60°, 75°, and 90°. Figures 1A–1C schematically show the structure of samples with α = 0°, 30°, and 90°, respectively. Thin lines represent whiskers of the superconducting phase, while thick lines show the possible superconducting pathways (or superconducting clusters).

Figure 2 shows the temperature dependences of resistivity of the samples with various whisker orientations indicated above. As can be seen, the resistivity of samples with α = 90°, 75°, and 60° varies with temperature in the range from 300 to 4.1 K in a manner typical of semiconductors. As the angle α decreases, the temperature dependence becomes less pronounced. For the sample with α = 45°, ρ very weakly varies with the temperature in the entire range indicated above. At *T* = 4.1 K,

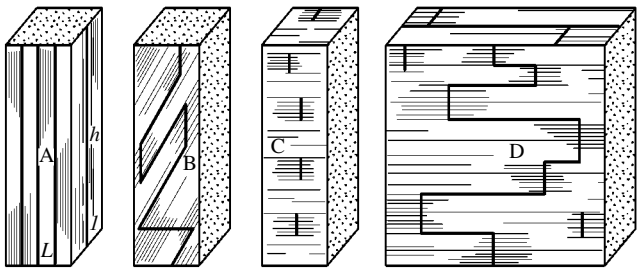

Fig. 1. Schematic diagrams illustrating the structure of samples cut from a GaSb–V_2Ga_5 eutectic composition: (A) the angle α between the directions of current and whiskers is zero (infinite superconducting cluster); (B) α = 30° (infinite superconducting cluster); (C) α = 90° (discrete superconducting regions composed of the Josephson junctions of the *S*–*Sm*–*S* type); (D) infinite superconducting cluster for arbitrary α.

the resistivities of all these samples exhibit a sharp drop, the magnitude of which increases with decreasing α.

The samples with $\alpha = 30°$, 15°, and 0°, in contrast to those mentioned above, pass to the superconducting state at $T = 4.1$ K. The temperature dependences of these samples exhibit a metal-like character.

One sample was cut in the form of a plate with square side faces parallel to the direction of crystallization (i.e., to the direction of whiskers) as depicted in Fig. 1D, where the thick solid broken line shows the possible superconducting cluster. In contrast to all samples mentioned above, this plate exhibits the superconducting transition at $T = 4$ K irrespective of the mutual orientation of current and whiskers (Fig. 3).

Discussion of results. As can be seen from the results presented above, the superconducting properties of the eutectic composition of the semiconductor–superconductor type studied can be controlled by changing the angle between the directions of whiskers and electric current and by cutting samples with various orientations.

When the electric current is passed perpendicularly to the direction of whisker growth ($I \perp X$, $\alpha = 90°$; Fig. 2, curve *7*), the semiconductorlike character of the temperature dependence of resistivity is related to the fact that V_2Ga_5 whiskers occupy only 4 vol % and rather slightly influence the properties of the semiconducting GaSb matrix (Fig. 1C). The samples with $\alpha = 30°$, 15°, and 0° can pass to the superconducting state and their $\rho(T)$ curves exhibit a metal-like character. Apparently, these samples feature the formation of superconducting clusters through the whole length at $T = 4.1$ K, while above the transition temperature, such clusters account for the metal-like conductivity. The sharp drop in the resistivity of samples with $\alpha = 90°$, 75°, 60°, and 45° at $T = 4.1$ K and an increase in the drop magnitude are related to the formation of discrete superconducting clusters (Fig. 1), the length and number of which increases with decreasing α.

In the case of $I \perp X$ ($\alpha = 90°$), a long rectangular parallelepiped of the GaSb–V_2Ga_5 composition features only contacts of the *S–Sm–S* type. Apparently, the absence of a superconducting transition in this system is explained by a large thickness of the superconducting layer (4–5 μm) between parallel whiskers. A sharp drop in the resistivity at $T = 4.1$ K suggests, and micrographs of the sample surface confirm, that whiskers are inhomogeneously distributed in the semiconducting matrix and the sample contains discrete superconducting regions forming Josephson chains of the type *S–Sm–S–Sm–S*… (Fig. 1C).

A parallelepiped sample with square side faces exhibits the superconducting transition at all angles α (including the case of $I \perp X$). In this case, infinite superconducting pathways (infinite clusters) cross the sample in the direction perpendicular to that of the whisker growth. In the direction along the whiskers ($I \parallel X$), the infinite clusters include both the aforementioned combinations and the whiskers of infinite length (Fig. 1D).

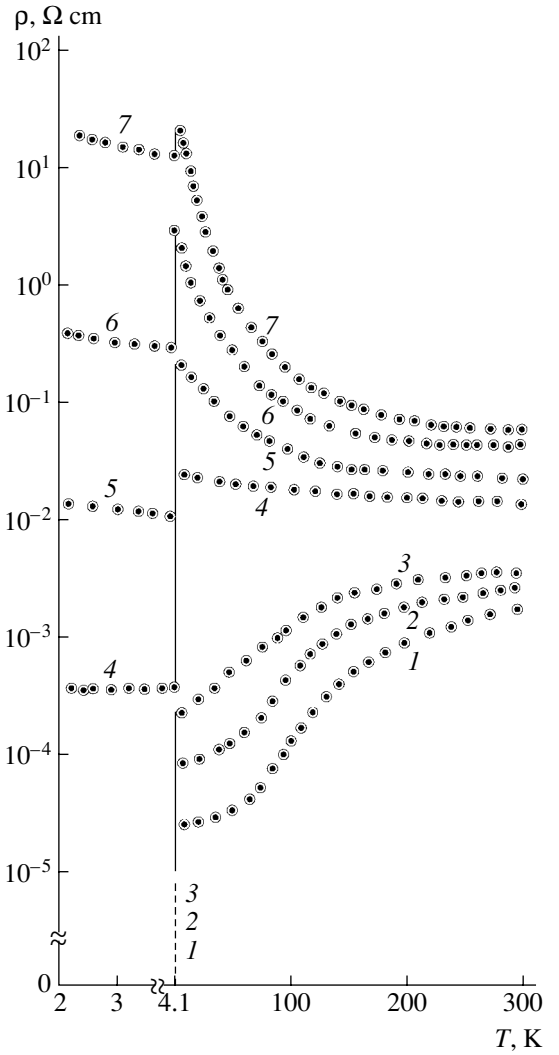

Fig. 2. Temperature dependences of the resistivity ρ of the samples of a GaSb–V_2Ga_5 eutectic composition, cut in the form of long parallelepipeds with various orientations so that $\alpha = 0°$ (*1*), 15° (*2*), 30° (*3*), 45° (*4*), 60° (*5*), 75° (*6*), and 90° (*7*).

The Josephson effect is observed both for $I \parallel X$ ($\alpha = 0°$) and for $I \perp X$ ($\alpha = 90°$) (in the latter case, provided that the transverse size L is comparable with the height h) [9]. It should be pointed out that the diameter d of a whisker can vary along its length [9], because various fluctuational processes during the growth lead to the appearance of narrowings. In the region of such a narrowing, the whisker diameter ($d \approx 5 \times 10^{-5}$ cm) is on the order of a coherence length ξ. Thus, each whisker in the eutectic composition studied comprises a sequence of microscopic bridges forming a chain of the type *S–S'–S–S'–S*… (*S'* is a microscopic bridge of variable thickness).

As can be seen from Fig. 3, the resistivities ρ of the plate measured for various angles α exhibit a strong anisotropy. In the temperature range studied, curves *1–3* ($\alpha = 0°$, 15°, 30°) show a metal-like character, while

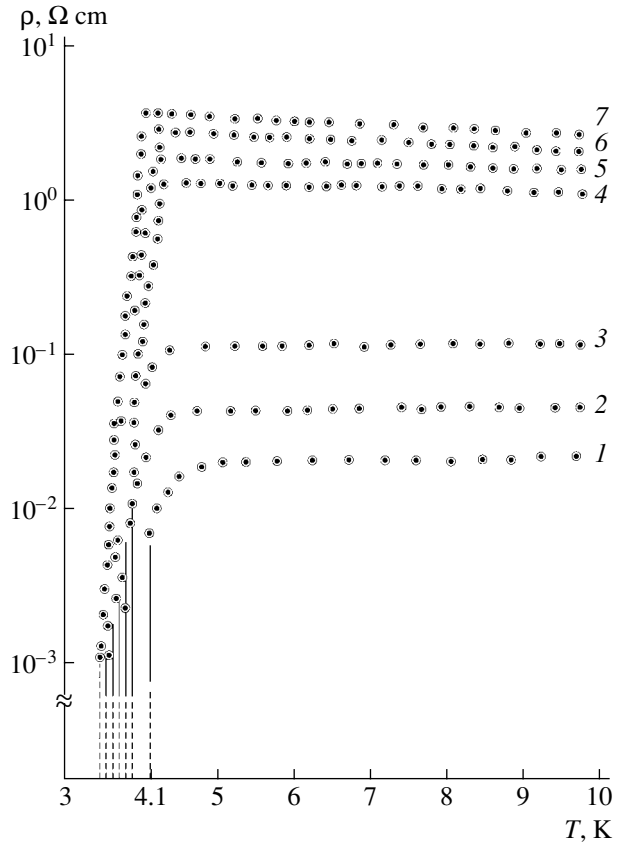

Fig. 3. Temperature dependences of the resistivity ρ of the samples of a GaSb–V_2Ga_5 eutectic composition, cut in the form of plates with $L = h$ and various orientations so that α = 0° (*1*), 15° (*2*), 30° (*3*), 45° (*4*), 60° (*5*), 75° (*6*), and 90° (*7*).

curves *4*–*7* (α = 45°, 60°, 75°, and 90°) exhibit a weak semiconductor-like behavior. Apparently, the dominating role in the transition to the superconducting state observed for α = 0°, 15°, and 30°, is played by the parallel infinite clusters comprising chains of the type *S*–*S*'–*S*–*S*'–*S*…, while for α = 45°, 60°, 75°, and 90°, the superconducting transition is determined by infinite clusters consisting of chains of the type *S*–*S*'–*Sm*–*S*–*S*'–*S*…. For α = 0°, the number of parallel infinite clusters per unit area in the transverse cross section is equal to the number of infinite whiskers (at a growth rate of v = 7 cm/h, the density of such whiskers is $n \approx 10^4$ mm^{-2}). Then, the current per unit area (mm^2) is

$$I = i_1 + i_2 + \ldots + i_n. \quad (1)$$

Assuming the average whisker diameters to be equal, we obtain

$$i_1 = i_2 = \ldots = i_n, \quad (2)$$

$$I = ni. \quad (3)$$

For α = 0°, the density of clusters is $n \approx 10^4$ mm^{-2}. As the angle α grows, the n value decreases and infinite clusters of the type *S*–*S*'–*S*–*S*'–*S*… are replaced by the clusters *S*–*S*'–*Sm*–*S*–*S*'–*S*….

Conclusions. The electrical properties of a GaSb–V_2Ga_5 eutectic composition can be controlled by varying the angle α between the directions of current and whiskers, in particular, by cutting samples with various orientations from the same ingot. In long rectangular samples with 45° ≤ α ≤ 90°, the sharp drop in the resistivity ρ at T = 4.1 K is explained by the presence of finite superconducting clusters. In the samples with 0° ≤ α ≤ 30°, the transition to the superconducting state is related to the formation of an infinite superconducting cluster.

For samples with length L (in the direction of whisker growth) equal to or greater than the height h (in the perpendicular direction), $L \geq h$, the superconducting transition is observed for all current directions and whisker orientations (for all values of α). This is explained by the formation of infinite superconducting clusters in all directions. An infinite superconducting cluster comprises Josephson junctions of the superconductor–semiconductor–superconductor type (*S*–*Sm*–*S*) connected by whiskers comprising chains of microscopic bridges (*S*–*S*'–*S*). Thus, a complete chain in the infinite superconducting cluster appears as *S*–*S*'–*Sm*–*S*–*S*'–*S*…. In the case of α = 0°, the main role is played by parallel infinite clusters comprising chains of the type *S*–*S*'–*S*'–*S*…. As the angle α increases in the interval from 0° to 90°, the total number of superconducting clusters decreases, while the contribution due to linked Josephson junctions of the type *S*–*Sm*–*S*–*Sm*–*S*… increases. The electrical properties of a square plate can be controlled both above and below the critical temperature by varying the angle α.

REFERENCES

1. G. I. Isakov, Pis'ma Zh. Tekh. Fiz. **22** (24), 70 (1996) [Tech. Phys. Lett. **22**, 1032 (1996)].
2. Yu. V. Kislinskiĭ, E. A. Stepantsov, Z. G. Ivanov, and T. Claeson, Fiz. Tverd. Tela (St. Petersburg) **43**, 581 (2001) [Phys. Solid State **43**, 602 (2001)].
3. J. A. Alarco and E. Olsson, Phys. Rev. B **52**, 13625 (1995).
4. D. Winkler, V. M. Zhang, P. A. Nilsson, *et al.*, Phys. Rev. Lett. **72**, 1260 (1994).
5. L. G. Aslamazov and M. V. Fistul', Zh. Éksp. Teor. Fiz. **81**, 382 (1981) [Sov. Phys. JETP **54**, 206 (1981)].
6. L. G. Aslamazov and M. V. Fistul', Zh. Éksp. Teor. Fiz. **83**, 1170 (1982) [Sov. Phys. JETP **56**, 666 (1982)].
7. L. G. Aslamazov and M. V. Fistul', Zh. Éksp. Teor. Fiz. **86**, 1516 (1984) [Sov. Phys. JETP **59**, 887 (1984)].
8. Th. Schapers, R. P. Muller, A. Kaluza, *et al.*, Appl. Phys. Lett. **75**, 391 (1999).
9. M. I. Aliev, G. I. Isakov, F. Yu. Aliev, and A. T. Éminzade, Dokl. Akad. Nauk SSSR **306**, 583 (1989) [Sov. Phys. Dokl. **34**, 454 (1989)].
10. M. I. Aliev and G. I. Isakov, Izv. Akad. Nauk SSSR, Neorg. Mater. **16**, 782 (1980).

Translated by P. Pozdeev

Technical Physics Letters, Vol. 29, No. 10, 2003, pp. 813–814. Translated from Pis'ma v Zhurnal Tekhnicheskoĭ Fiziki, Vol. 29, No. 19, 2003, pp. 48–51.

Measuring Hardness of Brittle Solids

A. B. Sinani

Ioffe Physicotechnical Institute, Russian Academy of Sciences, St. Petersburg, 194021 Russia
e-mail: alex@mdlab.ioffe.ru

Received April 14, 2003

Abstract—A method for determining the hardness of brittle solids under high loads is proposed. Using this technique, the hardness of inorganic glasses has been measured in a broad range of loads (1–300 N).

The conventional indentation technique used for measuring the microhardness of brittle solids (glasses, ceramics) does not always provide adequate information about the material hardness. Especially considerable difficulties arise during the investigations of heterogeneous media, where the indentation size is comparable with the dimensions of the material structure elements. Many of these problems would be solved if the hardness measurements could be performed in a broad range of indentor loads. However, the possibilities of hardness tests with high loads in brittle materials are rather restricted because of the indentation fracture. Figure 1a shows the typical pattern of the indentation fracture variation with growing load in a silicate glass.

However, direct observations [1, 2] of the process of Vickers indentor penetration into glass show that only separate cracks appear in the stage of loading, which do not significantly influence the material response as a function of the penetration depth. The main fracture of the indentation takes place during unloading and is caused by residual stresses existing in the zone of elastic-plastic deformation around the indentation.

It is possible to attempt at reconstructing the pattern under the indentor at the moment of unloading prior to the fracture by placing a thin layer of a plastic material (e.g., aluminum foil) on the sample surface. Then, the foil will retain an "impression" of the indentation, on

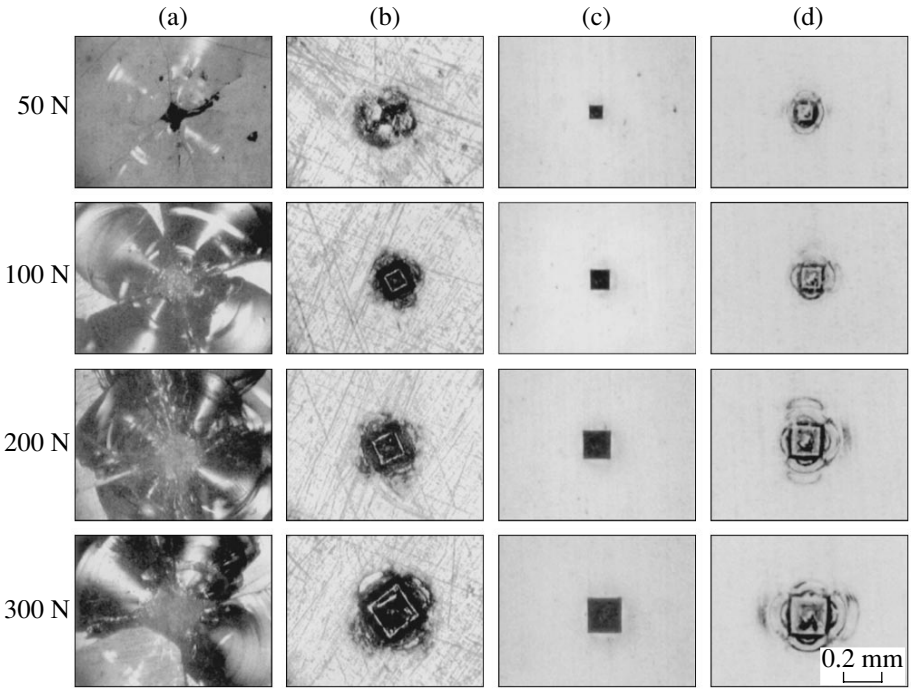

Fig. 1. Vickers pyramid indentations on the samples tested at various loads: (a) Pilkington SLS glass; (b) the same glass with a 7-μm-thick aluminum foil; (c) hardness standard; (d) the same material with the aluminum foil.

1063-7850/03/2910-0813$24.00 © 2003 MAIK "Nauka/Interperiodica"

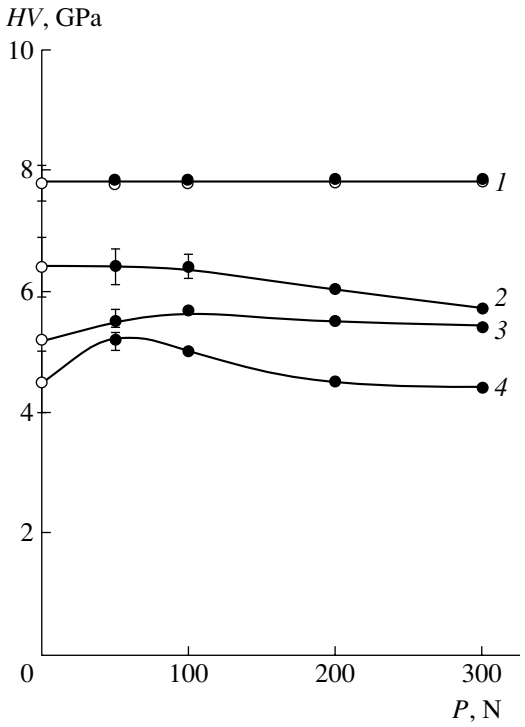

Fig. 2. Plots of the Vickers hardness versus load measured for various materials (○) without and (●) with a 7-μm-thick aluminum foil: (*1*) hardness standard; (*2*) Pilkington SLS glass; (*3*) rolled SLS glass; (*4*) lead glass.

which all the necessary measurements can be performed.

In order to check that a thin aluminum layer does not introduce significant errors into the results of hardness measurements, control tests have been performed on a hardness standard (*HV* = 7.8 GPa) with and without a 7-μm-thick aluminum foil. Figures 1c and 1d show the pattern of indentations obtained in a broad range of loads. As can be seen, the shape and dimensions of the indentations are virtually the same for the tests with and without the foil. According to the results of calculations, the values of hardness differ by no more than 3%.

Using the proposed method, the hardness tests were performed on various glasses, including two types of soda-lime-silica (SLS) glass (one of which was obtained by the Pilkington technology) and a dense flint (lead glass). Figure 1b shows an example of the impressions retained by a foil on the Pilkington glass tested in a broad range of loads. As can be seen, all impressions up to 300 N exhibit sharp contours and can be readily measured.

Figure 2 presents the plots of hardness versus load for the materials studied. As can be seen, the hardness standard shows a constant *HV* value in the entire range from 1 N (microhardness) to 300 N. Not that the *HV* values obtained with and without foil virtually coincide. For the rolled SLS and flint glasses with mechanically processed surfaces (ground and polished), the hardness versus load curves exhibit a weakly pronounced maximum. This maximum probably reflects the influence of the surface layer damage, caused by the mechanical treatment, on the microhardness. The subsequent decrease in the hardness observed with increasing load is related to the glass fracture under the indentor. As for the Pilkington glass, the surface of which was not additionally processed, the hardness is constant up to ~100 N and then starts decreasing as in other glasses studied. Note that a decrease in the hardness with increasing load is sufficiently smooth. This fact indicates that, even in brittle materials such as glass, the factor determining the resistance to indentor penetration at high loads is the plastic straining, rather than brittle fracture and crack development.

Thus, a method is proposed for the first time that allows determining the hardness of brittle solids under loads, which are two orders of magnitude higher than those used in the microhardness measurements. Using this method, it is demonstrated that, despite fracture development around the indentation, the hardness of glasses rather insignificantly decreases with increasing load.

REFERENCES

1. R. F. Cook and G. M. Pharr, J. Am. Ceram. Soc. **73**, 787 (1990).
2. R. Tandon, D. J. Green, and R. F. Cook, J. Am. Ceram. Soc. **73**, 2619 (1990).

Translated by P. Pozdeev

Technical Physics Letters, Vol. 29, No. 10, 2003, pp. 815–818. Translated from Pis'ma v Zhurnal Tekhnicheskoĭ Fiziki, Vol. 29, No. 19, 2003, pp. 52–59.

Satellite Peak Splitting in the X-ray Diffraction Rocking Curves of a Crystal Modulated by Surface Acoustic Wave

V. I. Punegov

Syktyvkar State University, Syktyvkar, Komi Republic, Russia
e-mail: punegov@syktsu.ru

Received April 23, 2003

Abstract—A theory of the X-ray diffraction modulated by surface acoustic wave in a crystal has been developed in a kinematical approximation in application to double- and triple-crystal diffractometry. The proposed theory is applied to interpretation of the experimentally observed splitting of satellite peaks in the rocking curves. *© 2003 MAIK "Nauka/Interperiodica".*

Increasing interest in the investigations of X-ray diffraction and hard synchrotron radiation scattering modulated by surface acoustic waves in crystals is related to the possibility of using acoustoelectronic devices in modern communication systems. Recently, Shchelokov *et al.* [1] experimentally observed splitting of the main and satellite peaks in the X-ray rocking curves of a crystal with the surface layer subjected to an ultrasonic action. However, theoretical explanation of the observed effect based on the model of Bragg reflections from a "system of pseudoplanes" [1] is incorrect. The results of numerical calculations, from which it follows that X-ray waves propagate within a subsurface layer at a depth equal approximately to half of the acoustic wavelength, neither penetrating into the bulk of the crystal nor emerging at the surface, are also doubtful.

As will be shown below, the peak splitting reported in [1] has an interference character and is related to a gradient of the modulation amplitude damping in depth of the crystal.

In order to provide for a simpler physical interpretation of the results, we use the formalism of the most general kinematical theory of scattering applicable to triple-crystal X-ray diffractometry [2]. This approximation is also valid in the case of a strongly deformed crystal lattice.

Assuming that the front of an X-ray wave incident onto a crystal is much greater than the thickness of a surface layer under consideration, the amplitude reflection coefficient can be expressed as

$$E_h(q_x, q_z) = i\sigma_h f \int_0^l dz \exp[(iq_z - \mu)z]\Phi(q_x, z), \quad (1)$$

where μ is the linear photoelectron absorption coefficient, l is the thickness of a deformed surface layer, f is the static Debye–Waller factor, $\Phi(q_x, z)$ is the Fourier transform of the field of atomic displacements, and $\Phi(x, z) = \exp(-ihu(x, z))$. The other notations are conventional (see, e.g., [2]).

Let the atomic displacements $\mathbf{u}(x, z)$ in the lateral directions of the layer under consideration be described by a periodic function, so that $\mathbf{u}(x + \Lambda, z) = \mathbf{u}(x, z)$, where Λ is the modulation period. Then, the function $\Phi(x, z)$ can be presented in the form of a Fourier series,

$$\Phi(x, z) = \sum_{m=-\infty}^{\infty} B_m(z)\exp(-im\kappa x),$$

where $\kappa = 2\pi/\Lambda$ is the lateral modulation wave number. In the general case, the Fourier coefficients

$$B_m(z) = (2\pi)^{-1} \int_0^{2\pi} \exp[\, i(hu(\varphi/\kappa, z) + m\varphi)]d\varphi$$

describe any periodic lateral strain of the crystal lattice. These coefficients are considered as functions of z, which implies variation of the modulation amplitude in depth of the deformed layer.

If the periodic lateral modulation has the form of a harmonic function, $u(x, z) = u_0(z)\sin(\kappa x)$, the Fourier coefficients are given by the mth-order Bessel functions: $B_m(z) = J_m(hu_0(z))$. In this case, the angular distribution of the diffraction intensity is described by the relation

$$I_h(q_x, q_z) = |\sigma_h|^2 f^2 (2\pi)^{-1} \times \left| \int_0^l dz \exp[(iq_z - \mu)z] \sum_{m=-\infty}^{\infty} J_m(hu_0(z)) D(q_x - m\kappa) \right|^2. \quad (2)$$

Here, $D(q_x - m\kappa) = 2\pi\delta(q_x - m\kappa)$ for an incident X-ray

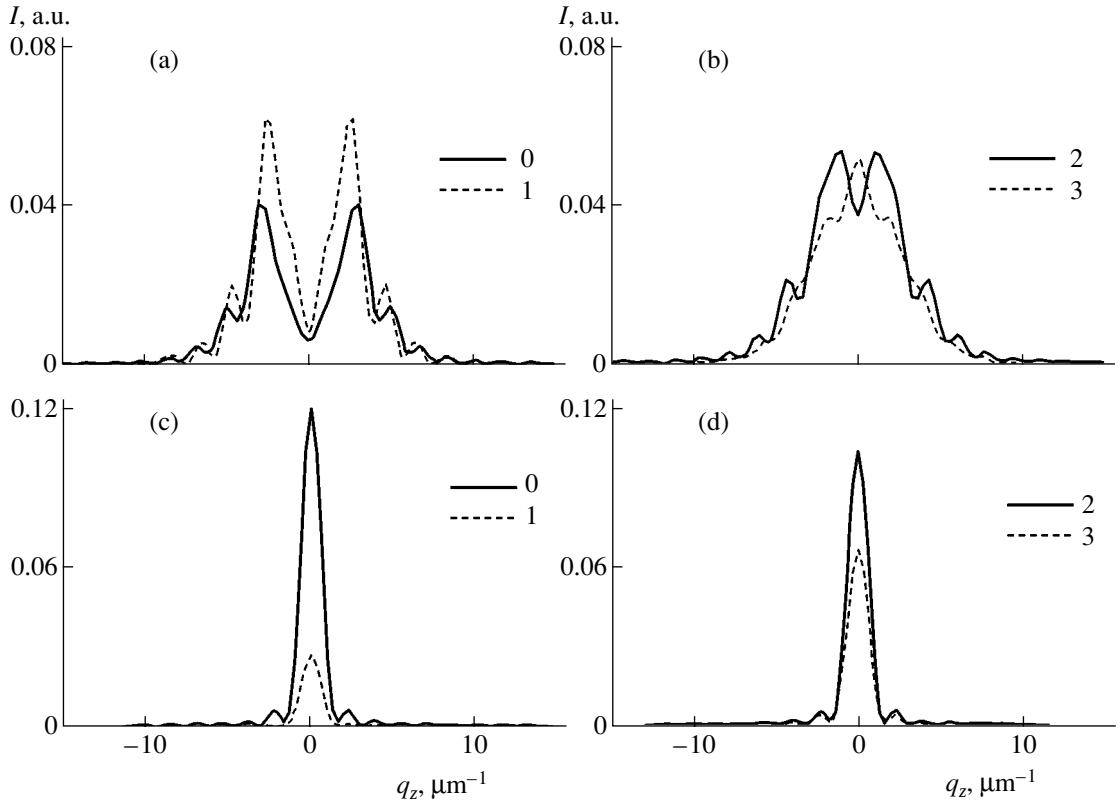

Fig. 1. Simulated rocking curves for satellite peaks in the regime of q_z scanning for (a, b) inhomogeneous and (c, d) homogeneous lateral modulation amplitude (figures indicate the satellite order).

wave with unbounded front and $|D(q_x - m\kappa)| = \sin((q_x - m\kappa)L_x)/(q_x - m\kappa)$ for the X-ray diffraction from a crystal of width L_x.

In the case of a plane incident X-ray wave with unbounded front, the intensity of scattering from the laterally modulated layer can be measured only using a triple-crystal scheme in the regime of q_z scanning in angular positions of the satellite peaks ($q_x = m\kappa$, $m = 0, \pm1, \pm2, \ldots$):

$$I_h^{(m)}(q_z) = |\sigma_h|^2 f^2 (2\pi)^{-1} \times \left| \int_0^l dz \exp[(iq_z - \mu)z] J_m(hu_0(z)) \right|^2. \quad (3)$$

Registration of the intensity of scattering using a triple-crystal scheme in the q_x scanning mode is possible only provided that the incident X-ray waver front is bounded or the X-ray beam is divergent. Under the same conditions, a double-crystal diffractometer with a wide-aperture detector is capable of measuring the integrated scattering intensity. For the double-crystal scheme, the rocking curve is calculated by integrating formula (2):

$$I_h(\eta) = \int I_h(q_x, -\eta + \cot\vartheta q_x) dq_x. \quad (4)$$

Here, η is the angular parameter usually employed in the double-crystal geometry [2] and θ is the angle between the crystal surface and the direction of the outgoing diffracted wave. Note that, using relation (2) and taking into account convolution with the instrumental function, it is possible to calculate the maps of the scattered intensity distribution in the reciprocal space [2].

From the solutions of Eq. (3), it follows that the behavior of the diffraction reflection curves of the satellite peaks is completely determined by the term $J_m(hu_0(z))$ in the integrand. If the modulation amplitude is constant across the layer, this term is independent of z and does not influence the diffraction reflection profile. In this case, all satellite peaks (including the main peak with $m = 0$) will correspond to the kinematical reflection curves for a perfect crystal. Since this also leads to the formation of a "system of pseudoplanes," the explanation of peak splitting within the framework of the model adopted in [1] is unjustified. The only reason for distortion of the reflection profile is variation of the scattering power in the depth of the crystal, related to the lattice strain gradient. This leads to a characteristic variation of the phases of X-ray waves reflected from various regions (layers) with different crystal lattice strains. In a certain sense, this approach is analogous to the method of "phase layers" developed for the crystals with a constant lattice strain gradient across a damaged surface layer [3].

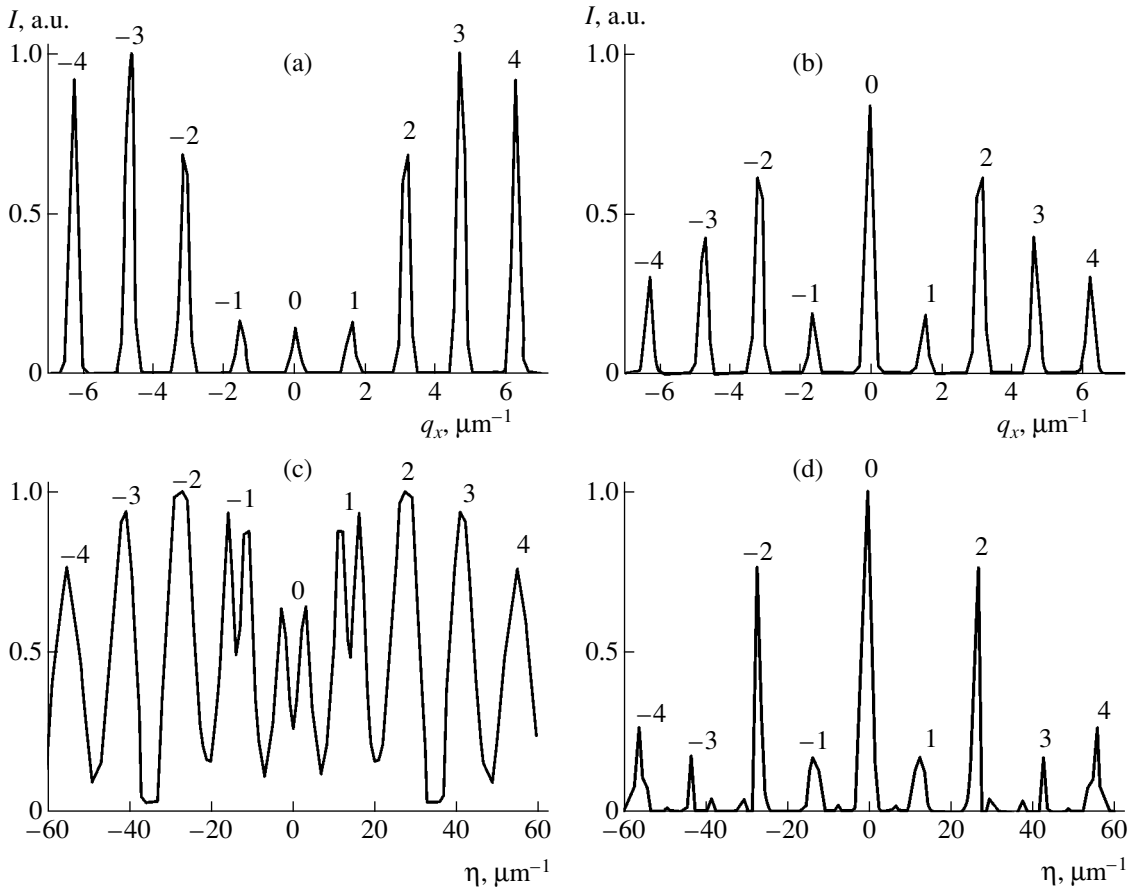

Fig. 2. Simulated (a, b) diffraction reflection curves in the regime of q_x-scanning (triple-crystal diffraction scheme) and (c, d) rocking curves (double-crystal diffraction scheme).

The above theoretical considerations can be illustrated by the results of numerical calculations performed for [104] reflection from a $LiNbO_3$ crystal exposed to a σ-polarized synchrotron radiation with $\lambda = 0.062$ nm. The modulation was produced by ultrasound with a wavelength of $\Lambda = 4$ μm in the crystal layer with a thickness of $l = 4$ μm. The surface acoustic wave modulation amplitude was assumed to exhibit exponential damping in depth, $u_0(z) = u_0 \exp(-z/l_a)$, where l_a is the acoustic wave penetration depth and u_0 is the modulation amplitude on the entrance surface. In the numerical calculation, the inhomogeneous modulation amplitude was characterized by $l_a = 2$ μm and $u_0 = 0.6$ nm; a homogeneous amplitude corresponds to $l_a \longrightarrow \infty$.

Figure 1 shows the diffraction curves in the region of satellite peaks corresponding to the q_z scanning mode in the case of inhomogeneous (a, b) and homogeneous (c, d) lateral modulation amplitude. As can be seen, the inhomogeneous modulation leads to peak splitting in the zeroth, first, and (partly) second order satellites. The third satellite exhibits no splitting. No peak splitting takes place in the case of a rather large homogeneous strain ($u_0 = 0.6$ nm).

Figure 2 shows the diffraction reflection curves obtained in the regime of q_x scanning (triple-crystal diffraction scheme) and the rocking curves (double-crystal diffraction scheme). The calculation was performed assuming a beam divergence of 0.2". As can be seen, no peak splitting takes place for the triple-crystal scheme in the q_x-scanning mode (sample rotation). At the same time, the rocking curves in the regime of double-crystal diffractometry display clear minima at the center of the main peak and the first satellites in the case of inhomogeneous modulation amplitude (Fig. 2c). Partial splitting of the third satellites in the diffraction curve of q_z scanning is not manifested in the double-crystal scheme, which is explained by the integral character of the scattered intensity measured in this scheme. However, a special feature of the double-crystal scheme with a wide-aperture detector is simultaneous (integral) registration of both the profile of individual satellite and its angular position in the diffraction pattern.

In conclusion, the proposed theory adequately describes the peak splitting in the rocking curves of X-ray diffraction from a crystal modulated by surface acoustic wave. This theory can be used to process the results of experimental X-ray diffraction measurements

for a crystal under the conditions of a strong ultrasonic action and large gradients of the acoustic modulation amplitude damping in depth of the crystal. In the case of small modulation amplitudes and the extinction lengths smaller than or comparable with the ultrasound penetration depth in the subsurface region of a crystal, the experimental data should be treated within the framework of a dynamical diffraction theory.

Acknowledgments. The author is grateful to K.M. Pavlov (Monash University, Australia) for fruitful discussion of results.

This study was supported in part by the Ministry of Education of the Russian Federation (project no. E02-3.4-302) and the Russian Foundation for Basic Research (project no. 03-02-16239).

REFERENCES

1. I. A. Shchelokov, D. V. Roshchupkin, and D. V. Irzhak, in *Proceedings of the Workshop "X-ray Optics 2003," Nizhni Novgorod, 2003* (Inst. Fiz. Mikrostrukt., Ross. Akad. Nauk, Nizhni Novgorod, 2003), pp. 279–288.
2. Ya. I. Nesterets and V. I. Punegov, Acta Crystallogr., Sect. A: Found. Crystallogr. **56**, 540 (2000).
3. V. I. Punegov and Yu. V. Vishnjakov, J. Phys. D **28**, A184 (1995).

Translated by P. Pozdeev

Technical Physics Letters, Vol. 29, No. 10, 2003, pp. 819–823. Translated from Pis'ma v Zhurnal Tekhnicheskoĭ Fiziki, Vol. 29, No. 19, 2003, pp. 60–68.

Nonreciprocal Waves in Absorbing Multilayer Systems

A. H. Gevorgyan

Yerevan State University, Yerevan, Armenia

e-mail: agevorgyan@ysu.am

Revised manuscript received April 15, 2003

Abstract—The propagation of naturally polarized light through a Fabry–Perot resonator with a layer of cholesteric liquid crystal is considered. In the presence of absorption, this system exhibits nonreciprocity even for naturally polarized light, which implies the existence of a new type of nonreciprocal reflection. An analysis of the peculiarities of this nonreciprocity shows that strongly nonreciprocal multilayer systems can be used as optical diodes or optical insulators (transmitting signals via an optical communication channel in one direction and blocking signals propagating in the opposite direction) or as systems for the accumulation of light energy. © *2003 MAIK "Nauka/Interperiodica".*

Introduction. As is known, nonreciprocity consists in a difference of the refractive indices for electromagnetic waves propagating in opposite directions (noninvariance with respect to $\mathbf{k} \longrightarrow -\mathbf{k}$ substitution). There are various mechanisms of nonreciprocity [1–19]. The theory of nonreciprocity has been developed in three directions: (i) investigation into various mechanisms of this phenomenon (this aspect is especially important for ring lasers and fiber gyroscopes [15, 16]); (ii) development of the theory of nonreciprocal reflection as a method of investigation of the internal structure of substances [10, 11]; and (iii) the search for the mechanisms of enhancement of nonreciprocal effects with a view to their possible applications, such as optical diodes, gates, or elements for light energy accumulators [12, 13, 17–19].

Venger *et al.* [14] discovered a new mechanism of nonreciprocity, which was observed in anisotropic inhomogeneous gyrotropic media and in multilayer systems with anisotropic gyrotropic layers. Recently [17], it was demonstrated that nonreciprocity is also observed in isotropic inhomogeneous gyrotropic media and in multilayer systems with isotropic gyrotropic layers. This new mechanism of nonreciprocity is related to the simultaneous presence of two factors: (i) the gradient of some parameter of the medium in the direction of light propagation and (ii) the natural or structural gyrotropy of the system.

The nonreciprocal effects were usually considered as weak and, despite their unique character, were never evaluated from the standpoint of practical use. Investigation [19] of the reflection and transmission of light in a layer of a natural gyrotropic medium exposed to an external magnetic field showed that multiple reflections in a layer of finite thickness may increase the nonreciprocity of reflection by several orders of magnitude ($\sim 10^2$–10^4) for certain wavelengths while decreasing the asymmetry of reflection for the other wavelengths. An additional mechanism increasing the nonreciprocity of reflection (or transmission) can be provided by the diffraction of light, since this phenomenon also involves the interference of a large (infinite) number of waves [17]. Indeed, it was demonstrated that some multilayer systems with structurally gyrotropic layers (featuring light diffraction on a periodic structure of the medium) are characterized by a large nonreciprocity of transmission (or reflection) and can be used as optical diodes or one-sided reflectors. An advantage of such systems is the possibility of obtaining significantly nonreciprocal transmission in the absence of even weak magnetic fields.

It was commonly accepted that the effects of nonreciprocity are of a purely polarization nature, whereby light with one polarization reflects differently from the left and right sides of a system and vice versa for light of another polarization. From this standpoint, no one optical system can be nonreciprocal for naturally polarized light, which is related to unitarity of the transfer matrix of an optical system. However, the transfer matrix is unitary only in the absence of absorption. The polarization character of nonreciprocity significantly restricts the field of possible applications of the nonreciprocal effects. In a system with absorption, the situation is cardinally different. As will be demonstrated below, such systems become nonreciprocal even for the naturally polarized light, which implies the existence of a new type of nonreciprocity.

Nonreciprocity in inhomogeneous gyrotropic media and in multilayer systems with one or several gyrotropic layers. The possibility of nonreciprocal reflection in inhomogeneous gyrotropic media follows immediately from the expansion of **D** into series with

1063-7850/03/2910-0819$24.00

respect to **E**. Restricting the consideration to terms linear in the wavevector **k** and the additive $\nabla\gamma$ representing a contribution of the inhomogeneity with respect to the optical activity parameter (the term proportional to $\nabla\varepsilon$, provided that $\nabla\varepsilon \neq 0$, may be included as well), we obtain

$$D_i = \varepsilon_{ij}^0 E_j + u\bar{\gamma}_{ijl}k_l E_j + \frac{\partial\bar{\gamma}_{ijl}}{\partial x_l}E_j, \quad B_i = \mu_{ij}H_j, \quad (1)$$

where $\bar{\gamma}_{ijl}$ is the antisymmetric tensor of optical activity. Therefore, the permittivity tensor can be represented in the following form:

$$\varepsilon_{ij}(\omega, \mathbf{k}, \nabla\gamma) = \varepsilon_{ij}^0(\omega) + i\bar{\gamma}_{ijl}(\omega)k_l + \frac{\partial\bar{\gamma}_{ijl}(\omega)}{\partial x_l}. \quad (2)$$

In view of the condition

$$\varepsilon_{ij}(\omega, \mathbf{k}, \nabla\gamma) \neq \varepsilon_{ij}(\omega, -\mathbf{k}, \nabla\gamma), \quad (3)$$

we infer that such media exhibit nonreciprocal reflection.

A common feature of these effects (optical activity and inhomogeneity) is the absence of nonreciprocity in cases of their separate manifestation. However, the optical activity is characterized by a helicoidal symmetry, whereby the state of polarization remains unchanged for the light transmitted through an optical medium and reflected back. On the contrary, the optical path difference acquired due to the inhomogeneity keeps accumulating during the light propagation in the reverse direction (axial symmetry). Should these factors be presented simultaneously, the medium would exhibit nonreciprocal reflection. It should be noted that nonreciprocity of the same kind can be related to a combination of some other factors, one of which is characterized by the axial symmetry and the other, by the helicoidal symmetry. According to the results of numerical calculations performed within the framework of the exact theory, inhomogeneous gyrotropic media are actually featuring nonreciprocal reflection.

It would be natural to expect that nonreciprocal reflection can take place both in inhomogeneous gyrotropic media and in multilayer systems with one or several natural (structural, or artificial) gyrotropic layers. This hypothesis can be readily verified. Indeed, consider the simplest system comprising one isotropic (nongyrotropic) layer and one gyrotropic layer. It is easy to check that the transfer matrices of these layers do not commutate with each other, which is equivalent to the existence of nonreciprocity. A physical origin of this nonreciprocity is related to the dependence of reflection from the interface on the polarization state and the ability of a gyrotropic medium to rotate the polarization plane.

Consider a multilayer nonreciprocal system of the glass plate (1)–cholesteric liquid crystal (CLC)–glass plate (2) type. Let a wave with the complex amplitude $\mathbf{E}_\mathrm{i}$ be normally incident onto this system. Denoting the complex amplitudes of the transmitted and reflected fields by $\mathbf{E}_\mathrm{r}$ and $\mathbf{E}_\mathrm{t}$, we can decompose these fields into *p*- and *s*-polarized components:

$$\mathbf{E}_{\mathrm{i,r,t}} = E^p_{\mathrm{i,r,t}}\,\mathbf{n}_p + E^s_{\mathrm{i,r,t}}\,\mathbf{n}_s = \begin{bmatrix} E^p_{\mathrm{i,r,t}} \\ E^s_{\mathrm{i,r,t}} \end{bmatrix},$$

where $\mathbf{n}_p$ and $\mathbf{n}_s$ are the unit vectors of the corresponding base polarizations. Then, the problem solution can be found in the following form:

$$\mathbf{E}_\mathrm{r} = \hat{R}\mathbf{E}_\mathrm{i}, \quad \mathbf{E}_\mathrm{t} = \hat{T}\mathbf{E}_\mathrm{i}, \quad (4)$$

where $\hat{R}$ and $\hat{T}$ are the Jones matrices of the system under consideration.

According to [20], the Jones matrix of system $\hat{R}_{\mathrm{A}+\mathrm{B}}$ and $T_{\mathrm{A}+\mathrm{B}}$ comprising two layers, A (left) and B (right), is expressed through the Jones matrices of the component layers by the matrix equations

$$\begin{aligned} \hat{R}_{\mathrm{A}+\mathrm{B}} &= \hat{R}_\mathrm{A} + \tilde{\hat{T}}_\mathrm{A}\hat{R}_\mathrm{B}[\hat{I} - \tilde{\hat{R}}_\mathrm{A}\hat{R}_\mathrm{B}]^{-1}\hat{T}_\mathrm{A}, \\ \hat{T}_{\mathrm{A}+\mathrm{B}} &= \hat{T}_\mathrm{B}[\hat{I} - \tilde{\hat{R}}_\mathrm{A}\hat{R}_\mathrm{B}]^{-1}\hat{T}_\mathrm{A}, \end{aligned} \quad (5)$$

where $\hat{I}$ is the unit matrix and tilde denotes the Jones matrices for the opposite propagation direction. In particular, for a CLC layer containing on both sides with the same medium, the Jones matrices for the light incident onto the CLC layer from the left and right media are related as

$$\begin{aligned} \tilde{\hat{T}} &= \hat{F}^{-1}\hat{T}\hat{F}, \\ \tilde{\hat{R}} &= \hat{F}^{-1}\hat{R}\hat{F}, \end{aligned} \quad (6)$$

where $\hat{F} = \begin{pmatrix} 1 & 0 \\ 0 & -1 \end{pmatrix}$ for the linear base polarizations. Since the exact Jones matrices for a homogeneous planar CLC layer and for an isotropic glass layer are known (see [21, 22], respectively), we can determine the Jones matrices for the glass (1)–CLC layer–glass (2) system by doubly applying relations (5). First the CLC layer is attached from the left side to glass (2) and then glass (1) is attached (also from the left side) to the CLC layer–glass (2) system. Omitting the calculations, we proceed to an analysis of the results of numerical calculations.

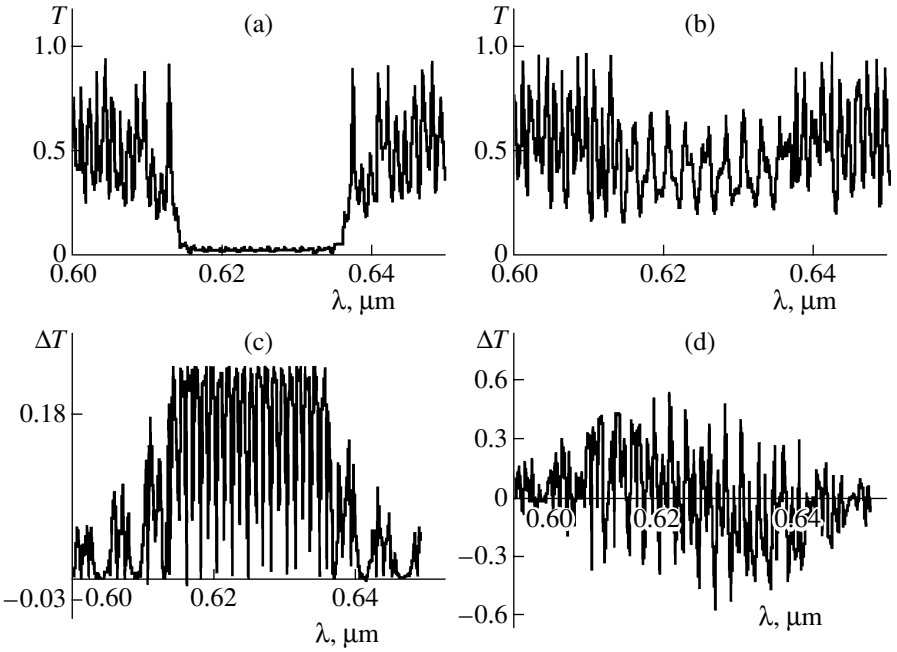

Fig. 1. The transmission coefficient T (a, b) and the transmission nonreciprocity ΔT (c, d) as functions of the light wavelength λ for the light with (a, c) clockwise circular polarization and (b, d) linear polarization incident onto a glass (1)–CLC layer–glass (2) system with the following parameters: principal CLC permittivity tensor values, $\mathrm{Re}\varepsilon_1 = 2.29$ and $\mathrm{Re}\varepsilon_2 = 2.143$; CLC helix pitch, $\sigma = 0.42$ μm; CLC layer thickness, $d = 50\sigma$; right-handed helix; refractive index of glass, $\mathrm{Re}n_1 = 1.5$ and $\mathrm{Re}n_2 = 3.5$; glass plate thicknesses, $d_1 = d_2 = 50$ μm.

Figure 1 shows the transmission coefficient T (a, b) and the transmission nonreciprocity $\Delta T = T_r - T_l$ (c, d) as functions of the light wavelength λ (T_r and T_l are the transmission coefficients for the light incident onto the system from the right and left sides, respectively). The incident light has either a clockwise circular polarization (a, c) or a linear polarization (b, d). As can be seen from Fig. 1, there are certain wavelengths for which ΔT is on the same order of magnitude as T, which suggests that the system under consideration can operate as an optical diode. For example, at $\lambda = 0.6304$ μm, we obtained $T_l = 0.5824$ and $\Delta T = -0.5280$. This result implies that the transmission in the reverse direction is about one-tenth of that in the forward direction, which confirms the optical diode character of the system.

The features of nonreciprocity in the system with absorption. In order to study the interaction of a naturally polarized light with a nonreciprocal optical system, let us pass from the Jones matrices to the Muller matrices. Here, the solution of the problem for the same glass (1)–CLC layer–glass (2) system can be written in the following form:

$$\mathbf{S}_t = \hat{M}_t \mathbf{S}_i, \quad \mathbf{S}_r = \hat{M}_r \mathbf{S}_i, \tag{7}$$

where $\mathbf{S}_i$, $\mathbf{S}_t$, and $\mathbf{S}_r$ are the 4×1 Stokes column vectors of the incident, transmitted, and reflected waves, respectively,

$$S_i = I\{1, P\cos(2\Phi_i)\cos(2\Psi_i), P\cos(2\Phi_i)\sin(2\Psi_i), P\sin(2\Phi_i)\};$$

I is the total intensity of the incident wave; Ψ_i and Φ_i are the azimuth and ellipticity of the polarization ellipse of a completely polarized component of the incident wave; P is the degree of polarization of the incident wave; and $\hat{M}_i$ and $\hat{M}_r$ are the Muller 4×4 matrices of the incident and reflected waves, respectively. The latter matrices are obtained from the Jones matrices by using the well-known rules [22]. Omitting the calculations, we proceed to an analysis of the features of nonreciprocity in the glass (1)–CLC layer–glass (2) system interacting with a naturally polarized light.

Figure 2 shows plots of the reflection nonreciprocity ΔR as a function of the wavelength of naturally polarized light ($P = 0$) for various values and characters of the optical absorption in the glass (1)–CLC layer–glass (2) system. The $|\Delta R|$ value was determined as the difference of the reflection coefficients for the light waves propagating in opposite directions. As can be seen from these data, the absorption makes the reflection nonreciprocal for the nonpolarized light (in the absence of absorption, this nonreciprocity vanishes). For certain wavelengths of the incident light, the magnitude of nonreciprocity $|\Delta R|$ significantly increases to become on the same order of magnitude as the reflection coeffi-

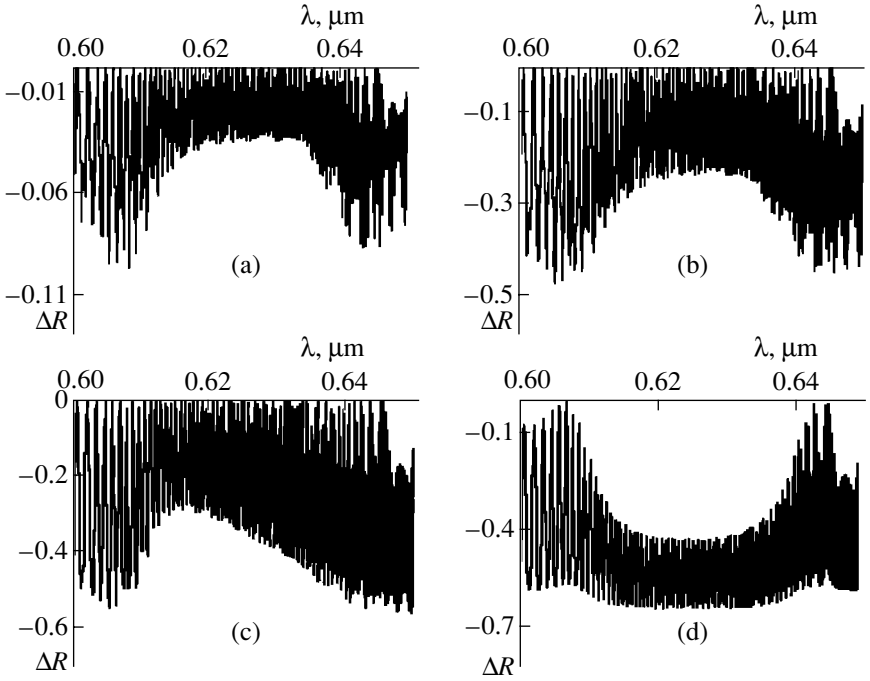

Fig. 2. Plots of the reflection nonreciprocity ΔR (determined as a difference of the reflection coefficients for the light propagating in opposite directions) as a function of the wavelength of a naturally polarized light ($P = 0$) for various characteristics of the glass (1)–CLC layer–glass (2) system ($d = 20\sigma$; $d_1 = d_2 = 1000$ μm): (a) $\mathrm{Im}\varepsilon_1 = \mathrm{Re}\varepsilon_2 = 0.001$, $\mathrm{Im}n_1 = \mathrm{Im}n_2 = 0$; (b) $\mathrm{Im}\varepsilon_1 = \mathrm{Im}\varepsilon_2 = 0.01$, $\mathrm{Im}n_1 = \mathrm{Im}n_2 = 0$; (c) $\mathrm{Im}\varepsilon_1 = 0.01$, $\mathrm{Re}\varepsilon_2 = 0$, $\mathrm{Im}n_1 = \mathrm{Im}n_2 = 0$; (d) $\mathrm{Im}\varepsilon_1 = \mathrm{Re}\varepsilon_2 = 0$, $\mathrm{Im}n_1 = 0.001$, $\mathrm{Im}n_2 = 0$.

cient R ($|\Delta R| \approx R$). This result suggests that such systems can perform the function of an optical diode, operating in the reflection mode, or act as a one-side reflector for the naturally polarized light. It should be noted that this system exhibits a singularity for $\Delta T = 0$ and $\Delta Q = -\Delta R$, whereby the nonreciprocal transmission is absent. Naturally, such system can also perform as one-side absorbers and nonreflecting absorbers.

It should be noted that these properties of absorbing nonreciprocal elements significantly expand the field of possible applications of nonreciprocal systems. In particular, there are real prospects for the creation of systems accumulating the energy of light. Such elements can be implemented in the solar energy converters into electricity, etc.

The effect of nonreciprocity with respect to the naturally polarized light, considered above for a system of the glass (1)–CLC layer–glass (2) type, has a general character and can be observed in multilayer systems with one or several gyrotropic (natural, structural, or artificial) layers in the presence of absorption.

In conclusion, it should be noted that the above theoretical results can be verified in real experiments and used for the development of a new class of optical elements, including optical diodes, one-side reflectors, one-side absorbers, and light energy accumulators. These elements can provide for the rapid progress in optoelectronics, ellipsometry, optical communications, and other fields. The numerical calculations were performed for a cholesteric liquid crystal of the cholesteryl nonanoate–cholesteryl chloride–cholesteryl acetate (20 : 15 : 6) composition with a room-temperature (24°C) helix pitch in the optical range ($\sigma = 0.42$ μm).

REFERENCES

1. R. Fuch, Philos. Mag. **11**, 647 (1965).
2. V. N. Lyubimov, Dokl. Akad. Nauk SSSR **181**, 858 (1968).
3. R. M. Hornreich and S. Shtrikman, Phys. Rev. **171**, 1065 (1968).
4. R. V. Pisarev, Zh. Éksp. Teor. Fiz. **58**, 1421 (1970) [Sov. Phys. JETP **31**, 761 (1970)].
5. W. F. Brown, Jr., S. S. Shtrikman, and D. Treves, J. Appl. Phys. **34**, 1233 (1963).
6. O. S. Eritsyan, Izv. Akad. Nauk Arm. SSR, Fiz. **3**, 217 (1968).
7. V. N. Belyĭ and A. N. Serdyukov, Kristallografiya **19**, 1279 (1974) [Sov. Phys. Crystallogr. **19**, 795 (1974)].
8. V. A. Markelov, M. A. Novikov, and A. A. Turkin, Pis'ma Zh. Éksp. Teor. Fiz. **25**, 404 (1977) [JETP Lett. **25**, 378 (1977)].
9. M. A. Novikov and A. A. Khyshov, Opt. Spektrosk. **87**, 416 (1999) [Opt. Spectrosc. **87**, 383 (1999)].
10. B. B. Krichevtsov, R. V. Pisarev, A. A. Rzhevsky, *et al.*, Phys. Rev. B **57**, 14611 (1998).
11. B. B. Krichevtsov, A. A. Rzhevsky, and H.-J. Weber, Phys. Rev. B **61**, 10084 (2000).

12. V. N. Belyĭ, S. N. Kurilkina, and S. N. Kovchur, Opt. Spektrosk. **83**, 409 (1997) [Opt. Spectrosc. **83**, 383 (1997)].
13. I. A. Andronova, G. V. Gelikonov, and G. B. Malykin, Kvantovaya Élektron. (Moscow) **26**, 271 (1999).
14. E. F. Venger, V. B. Popov, B. K. Serdega, and V. V. Shinkar, Opt. Spektrosk. **89**, 810 (2000) [Opt. Spectrosc. **89**, 746 (2000)].
15. N. V. Kravtsov and N. N. Kravtsov, Kvantovaya Élektron. (Moscow) **27**, 98 (1999).
16. I. A. Andronova and G. B. Malykin, Usp. Fiz. Nauk **172**, 849 (2002).
17. A. A. Gevorgyan, Izv. Akad. Nauk Arm., Fiz. **37**, 155 (2002).
18. A. A. Gevorgyan, Zh. Tekh. Fiz. **72** (8), 77 (2002) [Tech. Phys. **47**, 1008 (2002)].
19. A. A. Gevorgyan, Opt. Spektrosk. **91**, 812 (2001) [Opt. Spectrosc. **91**, 762 (2001)].
20. A. A. Gevorgyan, K. V. Papoyan, and O. V. Pikichyan, Opt. Spektrosk. **88**, 647 (2000) [Opt. Spectrosc. **88**, 586 (2000)].
21. A. A. Gevorgyan, Opt. Spektrosk. **89**, 685 (2000) [Opt. Spectrosc. **89**, 631 (2000)].
22. R. M. A. Azzam and N. M. Bashara, *Ellipsometry and Polarized Light* (North-Holland, New York, 1977).

Translated by P. Pozdeev

Technical Physics Letters, Vol. 29, No. 10, 2003, pp. 824–827. Translated from Pis'ma v Zhurnal Tekhnicheskoĭ Fiziki, Vol. 29, No. 19, 2003, pp. 69–76.

Reconstructing Nonautonomous System Models with Discrete Spectrum of External Action

D. A. Smirnov, I. V. Sysoev, E. P. Seleznev, and B. P. Bezruchko

Saratov Branch of the Institute of Radio Engineering and Electronics, Russian Academy of Sciences, Saratov, Russia

e-mail: sbire@sgu.ru

Received April 30, 2003

Abstract—We describe a method of constructing model differential equations using the scalar chaotic time series for systems under external action with discrete spectrum. The approach is based on taking into account the explicit time dependence in the structure of a model and approximating this dependence by trigonometric series. The proposed method is verified by numerical experiments on standard nonlinear systems driven by periodic and quasiperiodic factors of various types. *© 2003 MAIK "Nauka/Interperiodica".*

Introduction. In contrast to the dynamical modeling proceeding from first principles, when the choice of both the dynamical variables and the structure of equations is dictated by the laws of nature, the process of reconstructing model equations from the time series [1–5] is usually based only upon the researcher's intuition.[1] The wish to bring the empirical modeling out of the realm of "art" accounts for a considerable activity in the search for universal structures and technologies of reconstruction.

In cases of a single observable η, such a standard structure is offered (see, e.g., [2]) by a system of ordinary differential equations (ODEs)

$$\frac{dx_1}{dt} = x_2, \quad \frac{dx_2}{dt} = x_3, \ldots, \frac{dx_D}{dt} = f(x_1, x_2, \ldots, x_D), \quad (1)$$

where x_1 is the scalar observable η and f is a function represented by a polynomial of Kth order

$$f(x_1, x_2, \ldots, x_D) = \sum_{l_1, l_2, \ldots, l_D = 0}^{K} c_{l_1, l_2, \ldots, l_D} \prod_{j=1}^{D} x_j^{l_j}, \quad \sum_{j=1}^{D} l_j \le K. \quad (2)$$

The aspiration of these models to generality is theoretically justified, since almost any ODE system can be presented in the form of (1) (for detail, see [6]) and any continuous function f in these equations can be uniformly approximated to within any preset accuracy by an algebraic polynomial (2) (Weierstrass theorem). However, there are only a few cases of successful application of the standard approach to practical problems, especially for large K and D, because the number of coefficients is large and multiple differentiation leads to a sharp increase in the noise level.

Applicability of the standard approach can be increased at the expense of a partial loss of universality, by developing methods (technologies) oriented to a relatively narrow class of objects. In this paper, this approach is developed in application to the systems driven by a regular (possessing a discrete spectrum) external action. By this action we imply any periodic or quasiperiodic variations in the parameters or in the applied force. The premises for modeling a given object by an ODE system with a regular external action can be certain physical reasons (e.g., the presence of discrete peaks in the power spectrum of the observed time series)[2] or some aprioric information. The proposed method is based on introducing an explicit time dependence in the structure of model equations (by analogy with what was done for decreasing D in [7, 8] for a harmonically driven system) and on approximating this dependence, besides power polynomials (2), by trigonometric series.

Method of reconstruction. Consider a time series of an observable $\{\eta_i\}$ with the power spectrum containing discrete peaks at the frequencies $\omega_1, \omega_2, \ldots, \omega_m$ and their combination components. To begin with, we restrict the modeling by assuming a force character of the action driving the object and modify the standard structure of (1) by substituting

$$f(x_1, x_2, \ldots, x_D) \longrightarrow f(x_1, x_2, \ldots, x_D) + g(t), \quad (3)$$

[1] Among the extensive literature on modeling (construction and reconstruction of equations) using time series, we refer only to the original papers and domestic reviews with large lists of references.

[2] This is not a sufficient sign.

1063-7850/03/2910-0824$24.00 © 2003 MAIK "Nauka/Interperiodica"

where the function $g(t)$ describes the external action and, in the general case, is unknown. Let us represent this function by a sum of trigonometric polynomials,

$$g(t) = \frac{a_0}{2} + \sum_{j=1}^{k_1}\left(a_j\cos\left(\frac{2\pi jt}{T_1}\right) + b_j\sin\left(\frac{2\pi jt}{T_1}\right)\right) + \ldots + \sum_{j=1}^{k_m}\left(a_j\cos\left(\frac{2\pi jt}{T_m}\right) + b_j\sin\frac{2\pi jt}{T_m}\right), \quad (4)$$

where $T_j = 2\pi/\omega_j$. In the periodic case, $m = 1$, and in the quasiperiodic case, m is equal to the number of incommensurate frequencies. By analogy with the standard approach, x_1 will represent the scalar observable proper. The time series of $x_2(t_i), \ldots, x_D(t_i), \frac{dx_D(t_i)}{dt}$ are obtained by sequentially differentiating $\{x_1(t_i)\} = \{\eta(t_i)\}$ after noise filtration. In order to determine the coefficients of polynomial f and function g, we minimize by least squares the mean square of the approximation error[3]

$$\varepsilon^2 = \frac{1}{N} \times \sum_{i=1}^{N}\left(\frac{dx_D}{dt}(t_i) - f(x_1(t_i), \ldots, x_D(t_i)) - g(t_i)\right)^2 = \min. \quad (5)$$

Use of the structure according to (1), (3), and (4) introduces special features (distinct from the standard model) into the calculation of model coefficients: the parameters T_j enter into the expression for the action g in a nonlinear form and we have to minimize the approximation error ε^2 as a function of many variables by iterative methods. We employed the Levenberg–Marcquard method, although the values of linear parameters were still calculated by the linear least squares.[4] The global minimum is found by trying various initial approximations. A convenient initial approximation for T_j is offered by experimental estimates obtained from the spectra.

[3] In the general case, the parameters are estimated from data using the maximum likelihood method, least squares being a partial case of this. It was shown [9] that, in the general case, the estimates obtained by least squares can be significantly shifted. However, for a low noise level as in the case under consideration, these estimates are sufficiently accurate. For this reason, below we use the least squares method, which considerably simplifies the calculation.

[4] According the Levenberg–Marcquard method, initial approximations are chosen for all unknown coefficients and the functions f and g are linearized with respect to these coefficients in the vicinity of selected approximations, after which corrections to these approximations are obtained by linear least squares and the algorithm is repeated until attaining the minimum of ε (in the general case, a local minimum). The global minimum is found by trials with various initial approximations.

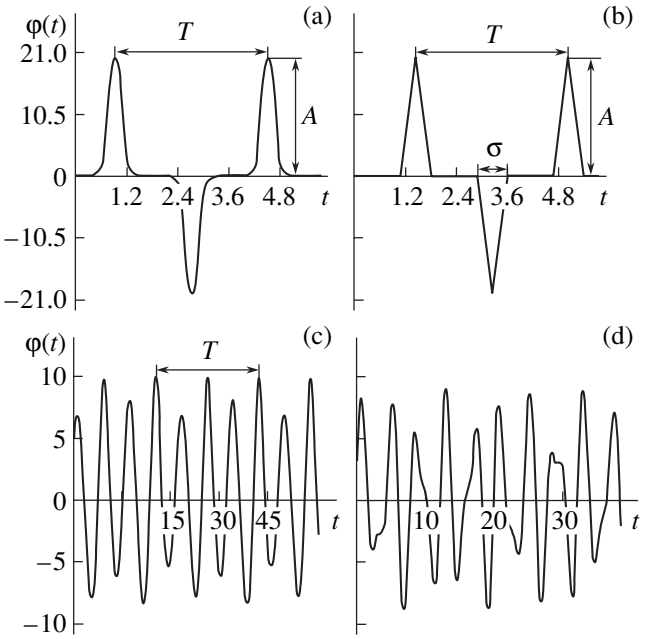

Fig. 1. Diagrams of external actions used in the numerical experiments: (a) Gaussian pulses

$$\varphi(t) = A\left(\exp\left(-\left(\frac{\tau(t)}{\sigma}\right)^2\right) - \exp\left(-\left(\frac{\tau\left(t+\frac{T}{2}\right)}{\sigma}\right)^2\right)\right), \quad (7)$$

$$\tau = (t + t_0)\bmod T - \frac{T}{2};$$

(b) triangle pulses; (c) signal with subharmonics (Rössler system [10] in the regime of period 4 with $a = 0.15$, $b = 0.2$, and $r = 5.7$); (d) quasiharmonic signal

$$\varphi(t) = A_1\sin\left(\frac{2\pi}{T_1}(t + t_0)\right) + A_2\sin\left(\frac{2\pi}{T_2}(t + t_0)\right), \quad (8)$$

where $T_1 = 4$, $T_2 = 2(\sqrt{5} - 1)$, $A_1 = 6$, and $A_2 = 3$.

Numerical experiment. In order to verify the proposed method, we performed reconstructions of the model ODEs the standard [Eqs. (1) and (2)] and modified [Eqs. (1), (3), and (4)] forms using chaotic time series obtained by integrating a nonautonomous equation of the Toda oscillator[5]

$$\frac{d^2x}{dt^2} - r\frac{dx}{dt} - 1 + e^{-x} - \varphi(t) = 0, \quad (6)$$

where $r = 0.5$ is the dissipation parameter and $\varphi(t)$ is the external action according to the variants in Fig. 1. The values of K, D, and k were chosen so as to optimize the model. The model quality criteria were the approximation error, the prediction times τ_{pred}, and the similarity

[5] The integration was performed by the fourth-order Runge–Kutta routine with a time step of $\Delta t = 0.01$.

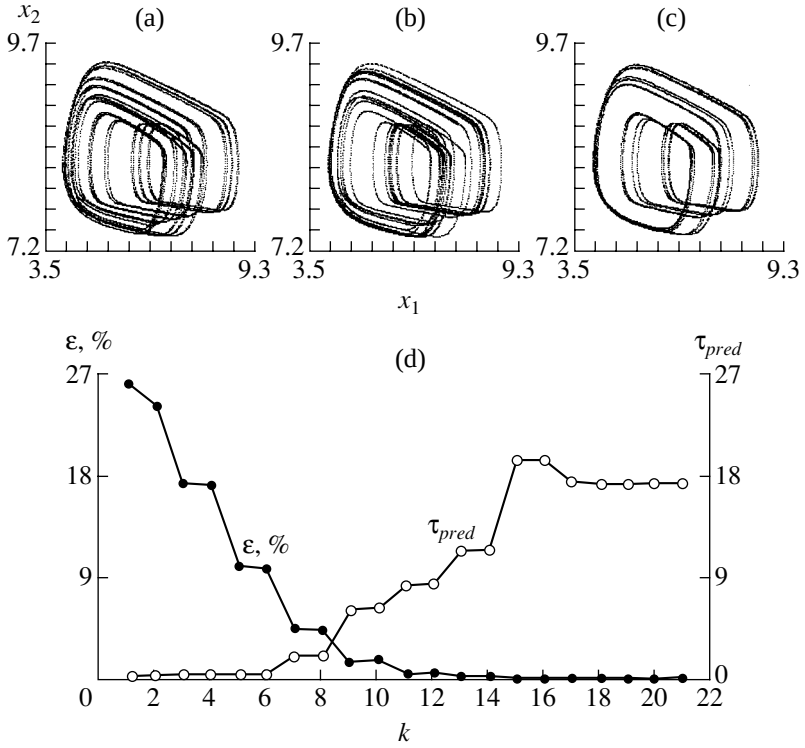

Fig. 2. Phase portraits of the object (a) and the results of modeling for $k = 15$ (b) without noise and (c) with a 1% noise. (d) The plots of ε (in %) and τ_{pred} (in driving signal periods T) versus the number of harmonics k in the approximation of external action (for the Gaussian pulses with $T = 3.6$, $A = 20$, $t_0 = 0$, and $\sigma = 0.2$).

of phase portraits of the model and object.[6] For the analysis of noise effects, the initial time series was supplemented with normal noise. Then the derivatives were calculated using an m-point smoothing second-order polynomial (the Sawitzky–Golay filter [11]) with the m value determined by trials.

A comparative analysis of the results of our numerical experiments leads to the following conclusions.

1. The standard algorithm [Eqs. (1) and (2)] does not lead to satisfactory results for any one of the external actions studied even in the absence of noise, whereas the modified structure [Eqs. (1), (3), and (4)] shows a good quality of reconstruction (provided the number of retained harmonics is sufficiently large) even in the presence of noise (Fig. 2).[7] Note that obtaining the optimum model requires a significantly longer trial series.

2. Complication of the form of external action leads to an increase in the number of terms in the trigonometric polynomial (4), but this has no negative consequences, in contrast to the standard models with high-order algebraic polynomials, whose global instability was the main cause of reverse for the standard approach. The external action in the form of triangle pulses required taking into account a very large (about 80–90) number of terms. Some successful experiments were performed even with 300–500 harmonics.

3. The presence of subharmonics in the external driving action presents no additional difficulties if the base frequency is taken equal to the minimum of the subharmonic frequencies.

4. In the case of a quasiperiodic external action (9), the nonautonomous model shows very good coincidence with the object: the phase trajectories of the object and model are practically indistinguishable.[8] The main difficulty in dealing with several trigonometric polynomials consists in that, in a certain stage of iteration, the periods of two high-order harmonics of various polynomials may become very close, which

[6] The prediction time τ_{pred} is the time for which the error of prediction does not exceed 5% of the standard deviation. This parameter is expressed in terms of the driving time scale T or the maximum possible prediction time $\tau_{\lim it}$ determined by the maximum-order Lyapunov exponent.

[7] For example, in the case of Gaussian driving function (7), the best standard model (with $D = 3$, $K = 2$) was characterized by $\varepsilon = 86.9\%$ and $\tau_{pred} = 0.078T$ at the maximum possible prediction time $\tau_{\lim it} \approx 60T$. The modified structure with $D = 2$ and $K = 8$ provides for a qualitative coincidence of the phase portraits and $\tau_{pred} = 19.24T$ already with $k = 8$ harmonics, showing the best result for $k = 15$ (Fig. 2).

[8] For $D = 2$, $K = 10$, and $m = 2$, we obtained $\varepsilon = 0.016\%$ and $\tau = 19.68T_1$ (at $\tau_{hor} = 63.7T_1$).

leads to degenerate or poorly conditioned matrix in solving the problem of estimating linear parameters. In this case, it is necessary to reduce the number of terms and increase the accuracy of initial values.

Conclusion. The results presented above show evidence of applicability of the ODE structure proposed for modeling a certain group of objects. In the case of a nonadditive (parametric or combined) action, the time dependence in the form of a finite sum of the Fourier series was introduced into all coefficients of the polynomial f (by analogy with [8]). If, unlike (1), all equations of the universal model contain unknown functions in the right-hand parts of all equations, then $g(t)$ is introduced into each of these equations. It is a remarkable fact that the quality of nonautonomous models is not impaired by using trigonometric series even of very high orders, in contrast to the use of power polynomials where the increasing order leads to instability.

Acknowledgments. This study was supported by the Russian Foundation for Basic Research (project nos. 02-02-17578 and 03-02-06858), the US Civilian Research and Development Foundation for the Independent States of the Former Soviet Union (CRDF Award No. REG-006), and the Noncommercial Program Foundation "Dynasty" (grant no. 245.662).

REFERENCES

1. J. P. Crutchfield and B. S. McNamara, Complex Syst. **1**, 417 (1987).
2. G. Gouesbet and C. Letellier, Phys. Rev. E **49**, 4955 (1994).
3. A. N. Pavlov, N. B. Yanson, and V. S. Anishchenko, Radiotekh. Élektron. (Moscow) **44**, 1075 (1999).
4. O. L. Anosov, O. Ya. Butkovskiĭ, and Yu. A. Kravtsov, Izv. Vyssh. Uchebn. Zaved., Prikl. Nelineinaya Dinam. **8**, 29 (2000).
5. A. M. Feĭgin, Ya. I. Mol'kov, D. N. Mukhin, and E. M. Loskutov, Preprint No. 508 IPF RAN (Institute of Applied Physics, Russian Academy of Sciences, Nizhni Novgorod, 1999).
6. T. Sauer, J. Yorke, and M. Casdgli, J. Stat. Phys. **65**, 579 (1991).
7. R. Hegger, H. Kantz, F. Schmuser, *et al.*, Chaos **8**, 727 (1998).
8. B. P. Bezruchko, Phys. Rev. E **63**, 016207 (2001).
9. P. E. McSharry and L. A. Smith, Phys. Rev. Lett. **83**, 4285 (1999).
10. O. E. Rossler, Phys. Lett. A **57A**, 397 (1976).
11. W. Y. Press, S. A. Teukolsky, W. T. Vetterling, and B. P. Flannery, *Numerical Recipes* (Cambridge Univ., Cambridge, 1992).

Translated by P. Pozdeev

Technical Physics Letters, Vol. 29, No. 10, 2003, pp. 828–830. Translated from Pis'ma v Zhurnal Tekhnicheskoĭ Fiziki, Vol. 29, No. 19, 2003, pp. 77–83.

The Effect of Electron Irradiation on the Electrical Properties of Ferroelectric BSTO Films

V. A. Balakin, A. I. Dedyk, S. F. Karmanenko, and M. V. Pavlovskaya*

St. Petersburg State Electrotechnical University, St. Petersburg, 197376 Russia

** e-mail: maryVP@mail.ru*

Received May 8, 2003

Abstract—We have experimentally studied the effect of a 200-eV electron beam on the capacitance, loss factor, and tunability factor of planar capacitor structures based on ferroelectric (Ba,Sr)TiO_3 films. A significant drop in the level of dielectric losses with a slight decrease in the capacity upon irradiation to a dose of 10^{14} and 10^{15} cm^{-2} was observed in film structures for the first time. The mechanisms of the observed effects and the role of structural defects are discussed. © *2003 MAIK "Nauka/Interperiodica".*

The effect of electron irradiation on ferroelectric materials has been most exhaustively studied for bulk ceramic materials [1–4]. To our knowledge, no data have yet been reported on the influence of this factor upon thin-film ferroelectric structures. However, from the standpoint of practical microwave electronics, thin ferroelectric films are presently of the most interest. In connection with this, we have studied the effect of electron bombardment on the electrical properties of ferroelectric $Ba_{0.6}Sr_{0.4}TiO_3$ (BSTO) films.

The BSTO films were obtained by RF cathode sputtering of a powder-synthesized target of the corresponding composition in oxygen at a pressure of 15–20 Pa, followed by thermal treatment in oxygen. Films with thicknesses within 0.5–1.0 μm were deposited onto polycor (polycrystalline corundum, Al_2O_3) and LAO (lanthanum aluminate, $LaAlO_3$) substrates. The metal electrodes (copper over chromium sublayer) were deposited by dc magnetron sputtering. The dielectric characteristics were measured for the planar capacitor structures prepared by photolithography and chemical etching [5]. The gap width in the planar capacitors was within 5–10 μm and the gap length was varied from 0.6 to 0.8 mm.

The capacitance–voltage (*C–U*) characteristics and the loss factor ($\tan\delta$) were measured at a frequency of $f = 1$ MHz in a range of voltages U from –200 to +200 V at room temperature (T = 300 K). The permittivity of the BSTO films was estimated using the method of partial capacitance [6], which takes into account the contributions from substrate and surrounding space to the capacitance of a planar capacitor structure.

The planar capacitors were irradiated with an electron beam generated by a static accelerator with thermoemission cathode (All-Russia Research Institute of Experimental Physics, Sarov). The samples were irradiated by 200-eV electrons to a total dose of 10^{14}, 10^{15}, or 5×10^{16} cm^{-2}. During the exposure, special measures were taken to avoid overheating and electrostatic charging of the samples. The effects of increasing discrete doses were studied on the same samples, with the electrical measurements performed after each irradiation cycle.

Figures 1 and 2 show the experimental data for one of the samples on a LAO substrate. The permittivity of this sample was $\varepsilon \approx 1900$. The *C–U* characteristic of this sample upon electron irradiation virtually completely coincided with the curve presented in Fig. 1. A comparison of these curves showed that the exposure did not influence the dielectric hysteresis. As a result of the irradiation, the coefficient of controllability (deter-

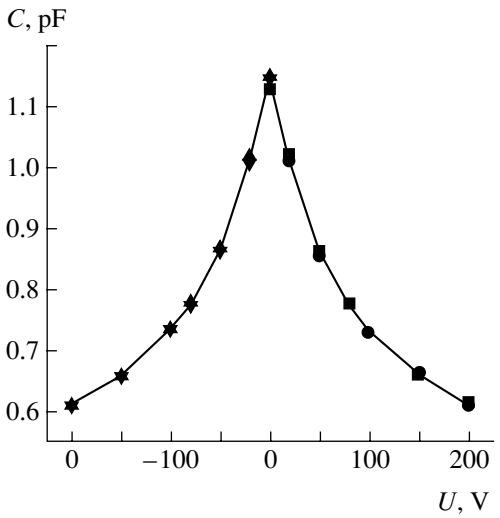

Fig. 1. The capacitance–voltage characteristic of a ferroelectric BSTO-film-based planar capacitor before electron irradiation.

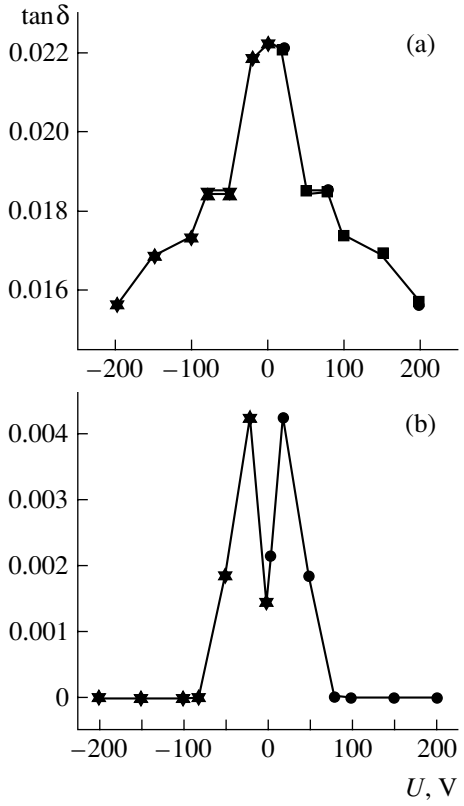

Fig. 2. The plots of $\tan\delta$ versus bias voltage for a ferroelectric BSTO-film-based planar capacitor (a) before and (b) after electron irradiation to a total dose of 5×10^{16} cm^{-2}.

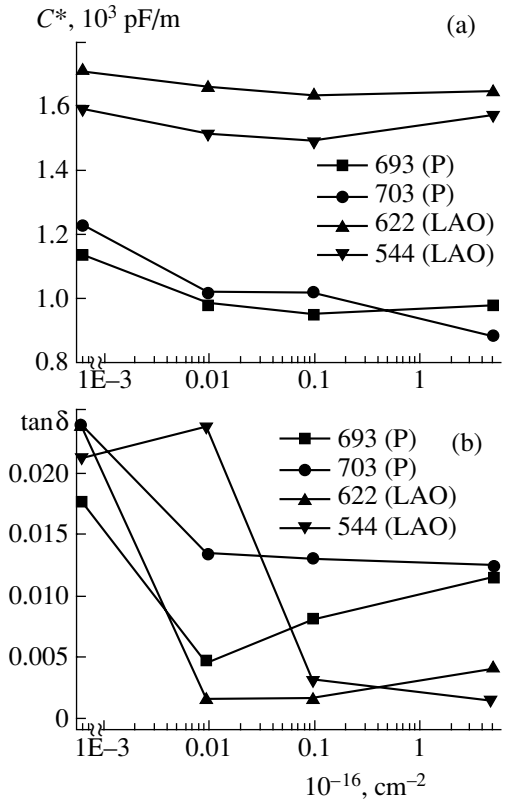

Fig. 3. Plots of the (a) linear capacitance and (b) $\tan\delta$ versus total electron irradiation dose for the ferroelectric BSTO-film-based planar capacitors on various substrates (LAO—lanthanum aluminate; P—polycrystalline corundum).

mined as the ratio of the initial capacitance to that at a maximum bias voltage, U = 200 V) decreased from 1.85 to 1.82.

An important experimental result was that the loss factor of irradiated samples was about ten times lower than that before irradiation (cf. Figs. 2a and 2b). For the given planar BSTO capacitor, the loss factor amounted to $\tan\delta = 1.5 \times 10^{-3}$ at $U = 0$ (Fig. 2b) and decreased to $\tan\delta < 5 \times 10^{-4}$ for the structures biased above 80 V. Prior to the exposure, $\tan\delta$ exhibited a monotonic decrease with increasing bias voltage; after the electron irradiation, the curve acquired a more complicated nonmonotonic shape, but even the maximum value of $\tan\delta$ (observed at U = 20 V) did not exceed 5×10^{-3}.

Figure 3 shows the plots of linear capacitance and loss factor versus irradiation dose for the planar BSTO film capacitors on different substrates. The initial values of C^* and $\tan\delta$ refer to the samples before irradiation. As can be seen, the most pronounced changes in the dielectric characteristics of all capacitors were produced by the exposures to 10^{14} and 10^{15} cm^{-2}. After the electron irradiation to these doses, the capacitance, permittivity, loss factor, and tunability acquired their minimum values.

The levels of capacitance C and permittivity ε of the films on LAO substrates were higher than those for the analogous samples on polycor. The relative changes in C and ε upon irradiation were lower (~5%) for the films of LAO substrates, while those for the samples deposited onto polycor reached 18%. Prior to exposure, the loss factor was ~0.02 for all samples. After the irradiation to 10^{14} and 10^{15} cm^{-2}, the level of losses in most cases exhibited a nearly tenfold decrease and varied from 5×10^{-3} to 5×10^{-4}.

A slight decrease in the capacitance and tunability experimentally observed for the samples irradiated to 10^{14} and 10^{15} cm^{-2} can be explained by accumulation of the radiation defects. Apparently, these are the Frenkel defects representing oxygen ions displaced into interstitial sites. This conclusion is based on the fact that the electron energy used in our experiments was close to a threshold for the oxygen displacement (160 keV [2]). Owing to a small thickness of the BSTO films studied (0.5–1 μm), there were no manifestations of the stopping effects leading to inhomogeneous distribution of the defects and space charge across the sample. It should be noted that the stopping effects, accompanied by a several-fold decrease in the permittivity, in BSTO ceramics with a thickness of 0.2–0.15 mm were observed even for an electron energy of 150 keV [3].

Thus, the high values of permittivity and tunability in our samples were retained just owing to a small (as compared to the aforementioned ceramics) thickness of the BSTO films.

A significant decrease in $\tan\delta$ (from 0.02 to 5×10^{-4}–5×10^{-3}) after the irradiation to 10^{14} and 10^{15} cm^{-2} is probably related to a compensation of the charge of oxygen vacancies as a result of the injection of electrons, which also decreases the probability of conductivity by the hopping mechanism.

According to some experimental data [2–4], a decrease in the capacitance and $\tan\delta$ in irradiated bulk ceramic samples was reversible. It was pointed out [2] that the radiation defects can be eliminated by applying an external electric field with a strength of 7×10^5 V/m. In our experiments, the film samples were subjected to a multiply repeated action of fields with a strength of up to ~10^7 V/m, but the values of C, ε, and $\tan\delta$ acquired by the samples as a result of irradiation remained unchanged.

Thus, we have practically important results indicative of an increase in the quality of ferroelectric film capacitor structures, which was not (and, apparently, could not be) observed for the bulk ceramic samples: electron irradiation to a dose of 10^{14} and 10^{15} cm^{-2} decreases the loss factor by a factor above ten ($\tan\delta \sim 10^{-3}$ at a frequency of 1 MHz), while rather insignificantly (within 5–17%) changing the values of C, ε, and the tunability factor.

REFERENCES

1. S. P. Solov'ev, I. I. Kuz'min, and V. V. Zakurkin, *Barium Titanate* (Nauka, Moscow, 1973).
2. V. V. Zakurkin, S. P. Solov'ev, and I. I. Kuz'min, Izv. Akad. Nauk SSSR, Ser. Fiz. **35**, 1148 (1971).
3. E. V. Peshikov, *Radiation Effects in Ferroelectrics* (Fan, Tashkent, 1986).
4. V. N. Lomasov, Élektron. Tekh., Ser. Radiodet. Radiokomp. **4** (77), 13 (1989).
5. S. F. Karmanenko, A. I. Dedyk, N. N. Isakov, *et al.*, Pis'ma Zh. Tekh. Fiz. **25** (19), 50 (1999) [Tech. Phys. Lett. **25**, 780 (1999)].
6. O. G. Vendik, *Ferroelectrics in Microwave Technology* (Sov. Radio, Moscow, 1979).

Translated by P. Pozdeev

Technical Physics Letters, Vol. 29, No. 10, 2003, pp. 831–832. Translated from Pis'ma v Zhurnal Tekhnicheskoĭ Fiziki, Vol. 29, No. 19, 2003, pp. 84–87.

Creating a System of Aspects of a Three-Dimensional Scene

N. M. Ganzherli* and D. F. Chernykh

Ioffe Physicotechnical Institute, Russian Academy of Sciences, St. Petersburg, 194021 Russia

** e-mail: nina@holo.ioffe.rssi.ru*

Received April 24, 2003

Abstract—We consider two schemes of creating a matrix of the holograms of aspects of a three-dimensional stage. The holographic variant is supplementary to the method of photographic registration of the system of aspects described previously. © *2003 MAIK "Nauka/Interperiodica".*

Previously [1–3], a method of creating three-dimensional (3D) images has been developed, according to which the image of a given scene is formed by a matrix of aspects focused into points. In the first step, a system of aspects is formed and, in the projection step, the aspects are transilluminated with a focused laser beam. Scanning over a screen, the beam forms a matrix of bright dots and, as a result, the viewer observes a 2D image localized on the screen, the configuration of which changes depending on the point of observation in the same manner as during observation of the real 3D object. This gives rise to the illusion of a 3D-character of the projected image.

It was pointed out that the process of scanning over the screen with a system of focused aspects is equivalent to simultaneous scanning of the screen with a system of independent thin light beams, each beam projecting its own aspect of the stage. A variant of display was considered, which reproduced only horizontal parallax of a 3D pattern. In this case, the viewing zone has to be extended in the vertical direction using a one-dimensional diffusion screen.

In this paper, we will consider two schemes for creating a holographic system of aspects of a 3D scene. The holographic variant is supplementary to the photographic method of creation of the matrix of aspects described previously.

In the first experiment, we recorded the linear Leith holograms of a 3D scene comprising several objects O and mirrors M_1 and M_2 used for additional backlighting and increasing the scene depth effect (Fig. 1). The objects represented two 6-cm-high busts made of white porcelain, arranged at various distances from mirrors and the recording medium H. The objects O were illuminated by a part of the collimated beam, which was incident onto mirror M_1 and provided backlighting of the objects upon reflection. The part of the collimated beam reflected from mirror M_1 formed a reference beam. The recording medium H (photographic plates for holography of the PFG-03M type, Russia) was placed in the plane of intersection of the reference and object beams.

Immobile slit diaphragm S, positioned in front of the recording plate, cut a narrow horizontal band from the incident beam, so that the recorded holograms had the form of strips with a height of 1.5–2 mm and a length of up to 75 mm. Further reduction in the strip height led to the loss of resolution in the record. The recording plate was gradually moved in the vertical direction relative to the horizontal slit, which allowed a matrix of linear holograms to be recorded. A 9×12 cm plate accommodated up to 40 linear holograms, each recording either a sequential change in the mutual arrangement of objects in the 3D scene or a new object. Each elementary portion of a linear hologram can be considered as an aspect of the 3D scene. Illuminated with a reference beam, the matrix of linear holograms yielded a 3D scene image. The horizontal eye movement gave a stage viewing angle on the order of 45°, while passage from one linear hologram to another produced the impression of changing scene. A disadvantage of this scheme is the relatively small viewing angle in the horizontal direction.

The second series of experiments was based on recording a sequence of Fourier holograms, each one imaging a separate aspect of the 3D scene. A laser beam

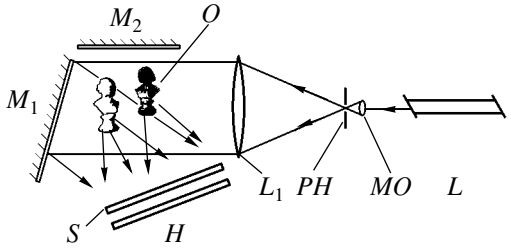

Fig. 1. A system for recording a matrix of linear Leith holograms of a 3D scene: (L) laser; (M_1, M_2) mirrors; (MO) microobjective; (O) objects; (L_1) lens; (H) recording medium; (PH) pinhole; (S) slit diaphragm.

1063-7850/03/2910-0831$24.00 © 2003 MAIK "Nauka/Interperiodica"

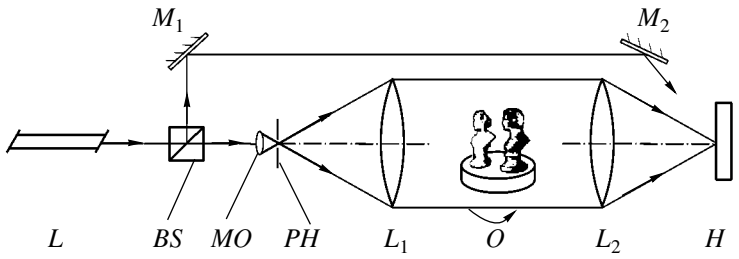

Fig. 2. A system for recording a sequence of Fourier holograms of a 3D scene: (*L*) laser; (*BS*) beam splitter; (M_1, M_2) mirrors; (*MO*) microobjective; (*O*) objects on a rotary platform; (L_1, L_2) lenses; (*H*) recording medium; (*PH*) pinhole.

collimated with microobjective *MO* and lens L_1 illuminated a 3D scene of objects *O* mounted on a rotary platform. Then the light was focused by the second lens L_2 onto the plane of recording medium *H* (photographic plates for holography of the PFG-03M type), where it also intersected with the reference beam. The reference beam represented an unexpanded laser beam, incident onto the recording medium either from the same side as the object beam or in the opposite direction.

Each subsequent hologram recorded the next scene aspect differing by the angle of platform rotation with a 1° or 2° step, depending on the desired resolution. The recording plate was displaced in the horizontal direction by a fixed distance slightly greater then the hologram size. The holograms were recorded near the focal plane of the second lens, rather than exactly in this plane, in order to reduce the nonlinear effects. Each hologram in the sequence can be considered as an aspect of the 3D scene. When the sequence of holograms is illuminated with a reference beam in the form of a bright line, the horizontal eye movement produced an impression of rotating scene. A special feature of this scheme is that the reference beam spreads in the plane perpendicular to the direction of recording of the sequence of holograms. This eliminates noises related to the possible superposition of the conjugate images of other holograms onto the real image at the stage of reconstruction.

A variant of this scheme corresponds to the case of nontransparent objects. Reconstruction of the image on a light background is accompanied by the formation of shadows, which change their mutual arrangement from one hologram to another, thus producing the illusion of examining the 3D scene. The viewing angle is determined by the number of recorded aspects in the sequence of holograms and by the angular step of platform rotation. In our experiments, the viewing angle varied from 55° to 110°.

Both variants proposed for the creation of matrices of the 3D scene aspects are compatible with the system of 3D image projection described in [1–3], reproducing the horizontal parallax.

Acknowledgments. This study was supported by the Russian Foundation for Basic Research (project no. 01-02-17854) and the Scientific School (project. no. 00-15-96771).

REFERENCES

1. Y. N. Denisyuk, V. B. Markov, and N. M. Ganzherli, Proc. SPIE **3011**, 45 (1997).
2. Yu. N. Denisyuk, V. B. Markov, and N. M. Ganzherli, Opt. Spektrosk. **84**, 104 (1998) [Opt. Spectrosc. **84**, 94 (1998)].
3. Yu. N. Denisyuk, N. M. Ganzherli, V. V. Orlov, *et al.*, Opt. Spektrosk. **86**, 864 (1999) [Opt. Spectrosc. **86**, 775 (1999)].

Translated by P. Pozdeev

Technical Physics Letters, Vol. 29, No. 10, 2003, pp. 833–835. Translated from Pis'ma v Zhurnal Tekhnicheskoĭ Fiziki, Vol. 29, No. 19, 2003, pp. 88–94.

On the Propagation of Perturbations in Multicomponent Media (Spherical Symmetry)

V. S. Krutikov and M. B. Rigina

Institute of Pulsed Processes and Technologies, National Academy of Sciences of Ukraine, Nikolaev, Ukraine

e-mail: ipre@iipt.aip.mk.ua

Received April 17, 2003

Abstract—Exact analytical solutions of the direct and inverse wave problems in the case of spherical symmetry were obtained for the first time by the method of inverse problems with allowance for the interaction of nonlinear arguments [8, 9]. The value of initial radius and the mobile boundary displacement can be arbitrary. It is shown that the obtained simple analytical relations can be used for the description of physical processes in continuous, multiphase, and multicomponent media, in which the density and sound velocity can vary within broad limits, depending on the initial components. *© 2003 MAIK "Nauka/Interperiodica".*

During investigations of electric discharge, it is often necessary to consider the working medium as a gas–liquid mixture. The formation and properties of such mixtures were described in [1, 2]. In describing the dynamics of a gas–liquid mixture during an electrical explosion, where the volume density of air varies from 10^{-4} to 10^{-2} and the bubble radius varies from 10 to 15 μm, the model of an equilibrium medium can be used provided that the transient process duration related to density variations (i.e., the time of the mixture relaxation related mostly to the presence of gas clusters) is small as compared to the characteristic time of external action (in this case, to the characteristic time of the active stage of the underwater electric discharge).

According to the conditions of correctness of the equilibrium approximation [3], the pressure in a system of gas bubbles with a diameter of 15 μm has to exceed 10 MPa. Thus, a quasiequilibrium description of hydrodynamic processes is possible, for example, in a bubbled gas–liquid medium under natural gas saturation conditions. The influence of gas inclusions can be described within the framework of a wave (linear) model of the equivalent continuous medium possessing an equivalent density ρ and low-frequency equilibrium sound velocity c. During the electrical explosion processing of various materials, multicomponent mixtures can be formed by introducing the processed materials and some other solids into the gas–liquid medium.

This work was aimed at obtaining exact analytical relations describing the propagation of compression waves with wavelengths exceeding the dimensions of inclusion spread in the liquid. We also evaluated the possibility of using these relations for the investigation of wave phenomena in multicomponent mixtures.

The values of ρ and c are determined by the volume content of components [4, 5]:

$$\rho = \sum_{i=1}^{n} (\rho_i \beta_i), \tag{1}$$

$$c = \rho \left(\sum_{i=1}^{n} \frac{\beta_i}{\rho_i c_i^2} \right)^{-1/2}, \tag{2}$$

where ρ_i and c_i are the density and the sound velocity in the ith component ($i = 1, 2, \ldots, n$) and β_i is the volume content of the ith component ($\sum_{i=1}^{n} \beta_i = 1$).

Previously [6–8], the applicability and the regions of correct use of the linear wave equation in solving the problem of cavity expansion in a compressible medium were considered in the one-dimension case. In direct problems, the conditions are set at a mobile boundary. In inverse problems, the conditions are known only at a certain point r_1 of the wave zone, for example, in the form of a pressure P described by an arbitrary function f:

$$P(r_1, t) = f\left(t - \frac{r_1 - r_0}{c}\right), \tag{3}$$

where t is the time and r_0 is the initial fixed radius of the mobile boundary. The values of the unknown function at other points, including the mobile boundary, and the unknown law of motion have to be determined.

In this study, the wave problem with a mobile boundary was solved by method of inverse problems with allowance of the interaction of nonlinear arguments [8, 9]. The case of cylindrical symmetry was ana-

lyzed in [9]. Below, we will consider the case of spherical symmetry.

Applying the unilateral Laplace transform to the wave equation and taking into account relation (3) and zero initial conditions, we obtain an operator equation. An exact analytical solution of this equation for an infinite medium is as follows:

$$\varphi(r,t) = \frac{r_1}{r\rho}\int_0^t f(\xi)dt; \quad \xi = t - \frac{r-r_0}{c};$$
$$\varphi(R(t),t) = \frac{r_1}{R(r)\rho}\left[\int_0^t f(\xi)dt\right]_{r=R(t)}. \tag{4}$$

The values of pressure and velocity at an arbitrary point r in the wave zone are given by the expressions

$$P(r,t) = \frac{r_1}{r}f(\xi) = F_1;$$
$$v(r,t)\frac{r^2\rho}{r_1} = \frac{r}{c}f(\xi) + \int_0^t f(\xi)dt = F_2, \tag{5}$$

while the values on the mobile boundary $R(t)$ are given by

$$P(R(t),t) = F_1(R(t),t) - \frac{1}{2}\rho v^2(R(t),t);$$
$$v(R(t),t) = F_2(R(t),t); \tag{6}$$

$$\frac{[R^3(t)-r_0^3]\rho}{3r_1} = \left[\int_0^t \frac{r}{c}f(\xi)dt + \int_0^t\int_0^t f(\xi)dtdt\right]_{r=R(t)}. \tag{7}$$

Approximating the function f in Eqs. (4)–(7) by the Lagrange polynomials of mth power,

$$f = \sum_{m=0}^{\infty} A_m \xi_1^m, \tag{8}$$

where A_m are constant coefficients, we obtain the following expressions for the pressure and velocity at a point r of the wave zone,

$$P(r,t) = \frac{r_1}{r}\sum_{m=0}^{\infty} A_m\xi^m - \frac{1}{2}\rho v^2(r,t), \tag{9}$$

$$v(r,t)\frac{\rho r^2}{r_1} = \frac{r}{c}\sum_{m=0}^{\infty} A_m\xi^m + \sum_{m=0}^{\infty}\frac{A_m}{m+1}\xi^{m+1}, \tag{10}$$

and on the mobile boundary,

$$P(R(t),t) = \frac{r_1}{R(t)}\sum_{m=0}^{\infty} A_m\xi^m - \frac{1}{2}\rho v^2(R(t),t),$$
$$\xi = t - \frac{R(t)-r_0}{c}, \tag{11}$$

$$v(R(t),t)\frac{\rho R^2(t)}{r_1} = \frac{R(t)}{c}\sum_{m=0}^{\infty} A_m\xi^m + \sum_{m=0}^{\infty}\frac{A_m}{m+1}\xi^{m+1}, \tag{12}$$

$$\frac{[R^3(t)-r_0^3]\rho}{3r_1} = \frac{R(t)}{c}\sum_{m=0}^{\infty}\frac{A_m}{m+1}\xi^{m+1} + \sum_{m=0}^{\infty}\frac{A_m m!}{(m+1)(m+2)}\xi^{m+2}. \tag{13}$$

Solutions (9)–(13) are exact (substituting into the wave equation makes the left-hand part equal zero) and universal (applicable to both direct and inverse problems).

For representing the pressure variation at a point r_1 of the wave zone in the form of a step of amplitude A_0,

$$P(r_1,t) = A_0\sigma_0\left(t - \frac{r_1-r_0}{c}\right), \tag{14}$$

where σ_0 is the unity discontinuous function of zeroth order, and using formulas (4)–(7), we obtain

$$P(r,t) = \frac{r_1}{r}A_0\sigma_0(\xi) - \frac{1}{2}\rho v^2(r,t), \tag{15}$$

$$v(r,t) = \frac{r_1}{r^2\rho}\left[\frac{r}{c}A_0 + A_0\xi\right], \quad \xi = t - \frac{r-r_0}{a}, \tag{16}$$

and the pressure and velocity on the mobile boundary $R(t)$,

$$P(R(t),t) = \frac{r_1}{R(t)}A_0 - \frac{1}{2}\rho v^2(R(t),t), \tag{17}$$

$$v(R(t),t) = \frac{r_1}{R^2(t)\rho}\left[\frac{R(t)}{c}A_0 + A_0\xi\right], \tag{18}$$

$$\frac{[R^3(t)-r_0^3]\rho}{3r_1} = \frac{R(t)}{c}A_0\xi + \frac{A_0}{2}\xi^2, \quad \xi = t - \frac{R(t)-r_0}{c}. \tag{19}$$

This exact analytical solution of the inverse problem with a mobile boundary can be used, in particular, for obtaining estimates and determining maxima of the functions under consideration.

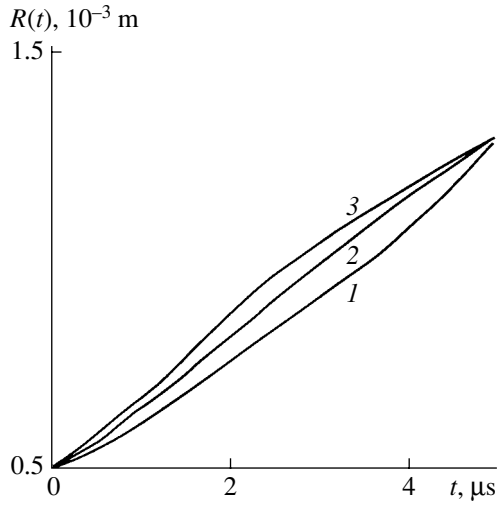

Fig. 1. Time variation of the radius $R(t)$ of the mobile boundary of a plasma cavity expanding in (*1*) water, (*2*) mixture I, and (*3*) mixture II.

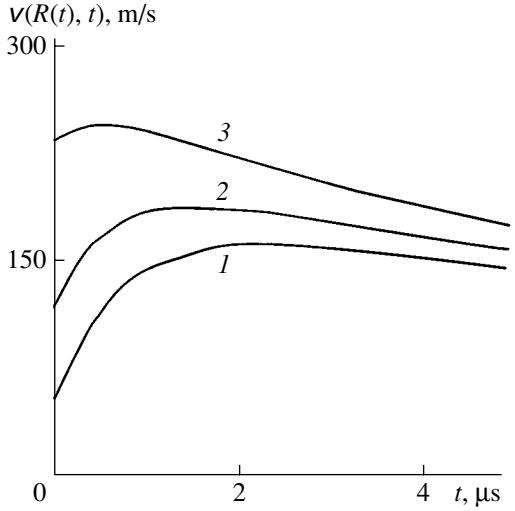

Fig. 2. Time variation of the velocity $v(R(t), t)$ of the mobile boundary of a plasma cavity expanding in (*1*) water, (*2*) mixture I, and (*3*) mixture II.

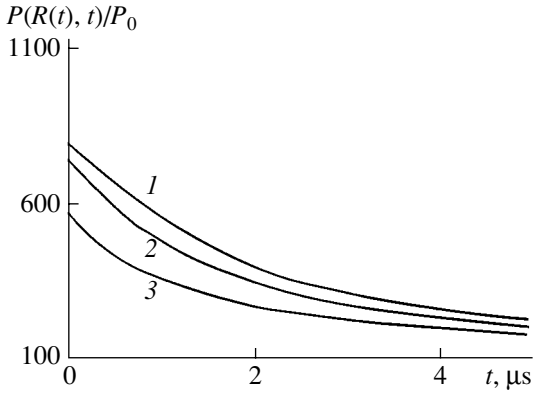

Fig. 3. Time variation of the pressure $P(R(t), t)$ (relative to the initial value P_0) at the mobile boundary of a plasma cavity expanding in (*1*) water, (*2*) mixture I, and (*3*) mixture II.

We have performed a numerical calculation of the functions $R(t)$, $P(R(t), t)$ and $v(R(t), t)$ using expressions (14)–(18) with $r_1 = 20 \times 10^{-3}$ m, $A_0 = 20$ bar = 1.96 MPa, $r_0 = 0.5 \times 10^{-3}$ m for the following media:

(i) water ($\rho = 1000$ kg/m^3, $c = 1460$ m/s); (ii) mixture I ($\rho = 840$ kg/m^3, $c = 800$ m/s) (modeling a mixture of water, air, and cellulose fibers); (iii) mixture II ($\rho = 840$ kg/m^3, $c = 400$ m/s). The results of calculations are presented in Figs. 1–3. As can be seen from a comparison with the results for water, mixtures I and II are characterized by greater radii of the mobile boundary (for mixture II, by 9% in 1 μs after the beginning of motion) and by higher velocities (in the beginning of motion, by a factor of 2 and 4 for mixtures I and II, respectively). The pressure on the mobile boundary of the plasma cavity in expanding mixtures is lower than that in water. The fact that the velocities sometimes fall beyond the limits of applicability of the wave equation was analyzed in [7].

In conclusion, the proposed method can be used for controlling wave processes, that is, to obtain a certain function of pressure and velocity at a given point of the wave zone (including the near zone and the mobile boundary) in various multicomponent mixtures. This is achieved by varying the mixture density and the sound velocity through a change in the composition and in the content of separate components of these mixtures.

REFERENCES

1. L. R. Gavrilov, *Physics and Engineering of Powerful Ultrasonics*, Vol. 3: *Fundamentals of Supersonic Technology* (Nauka, Moscow, 1970), pp. 393–426.
2. M. G. Sirotyuk, *Physics and Engineering of Powerful Ultrasonics*, Vol. 2: *Powerful Supersonic Fields* (Nauka, Moscow, 1968), pp. 167–220.
3. V. G. Kovalev, M. B. Rigina, and V. N. Tsurkin, Pis'ma Zh. Tekh. Fiz. **25** (6), 21 (1999) [Tech. Phys. Lett. **25**, 215 (1999)].
4. G. K. Batchelor, in *Mechanics: A Collection of Translated Foreign Articles* (1968), Vol. 3, pp. 65–84.
5. A. L. Anderson and L. D. Hampton, J. Am. Stat. Assoc. **67**, 1865 (1980).
6. V. S. Krutikov, *One-Dimensional Problems in the Mechanics of Continuous Media with Moving Boundaries* (Naukova Dumka, Kiev, 1985).
7. V. S. Krutikov, Akust. Zh. **42**, 534 (1996) [Acoust. Phys. **42**, 471 (1996)].
8. V. S. Krutikov, Dokl. Akad. Nauk **364**, 17 (1999) [Math. Dokl. **59**, 10 (1999)].
9. V. S. Krutikov, Dokl. Akad. Nauk **368**, 755 (1999) [Dokl. Phys. **44**, 674 (1999)].

Translated by P. Pozdeev

Technical Physics Letters, Vol. 29, No. 10, 2003, pp. 836–837. Translated from Pis'ma v Zhurnal Tekhnicheskoĭ Fiziki, Vol. 29, No. 20, 2003, pp. 1–4.

Evaluation of the Photoelectron Contribution to the Efficiency of Open Discharge

A. R. Sorokin

Institute of Semiconductor Physics, Siberian Division, Russian Academy of Sciences, Novosibirsk, 630090 Russia

e-mail: IFP@isp.nsc.ru

Received May 6, 2003

Abstract—Estimates of the energy necessary to provide for the emission of a single photoelectron from a cathode in open discharge show that (i) the discharge cannot be maintained at the expense of photoemission and (ii) the contribution of photoelectrons to the energy efficiency of the electron beam formation is negligibly small.

The author reckons that the recent series of papers [1–5] have exhaustively answered the question as to whether open discharge with a grid anode is a discharge of the new, photoelectron, type or it is merely a kind of glow discharge. Indeed, the unsoundness of all principal arguments for a photoelectron nature of the open discharge was convincingly demonstrated, and it was shown that the efficiency of the electron beam formation in the open discharge calculated with allowance of only the atom-induced electron emission [1] coincides with the experimentally measured energy efficiency [5]. However, the absence of calculations or estimates of the direct contribution to this efficiency due to photoelectrons emitted from the cathode may leave a sense of dissatisfaction and does not exclude the new attempts to prove a photoelectron nature of open discharge. The aim of this paper is to fill the gap. This goal is most simply reached by estimating the energy w_s necessary to provide for the emission of a single photoelectron from the cathode.

1. First, let us obtain an estimate of w_s from below for the conventional open discharge with a usual grid anode. Consider an open discharge with a small cathode area (~1 cm^2), for which the main properties of open discharges were studied by various researchers (this and subsequent assumptions are not of principal significance and only simplify the estimation procedure), and take into account that the discharge characteristics do not change upon decreasing to 1 cm the length of the electron beam drift region behind the grid [6–9]. In this case, only about 1/6 of the total radiation emitted from the drift space volume of 1 cm^3 will strike the cathode. Assuming that the excitation of a resonance level (21.2 eV), expected to give a maximum contribution to the photoemission, and the ionization of helium (24.6 eV) are produced with equal efficiencies and using the photoemission coefficient $\gamma_V = 0.1$ [10], we can estimate the necessary energy consumption as w_s = (21.2 + 24.6 eV) $6 \times 10 \approx 2.7$ keV. Real energy losses, e.g., for a photoelectron with an energy of w = 3 keV emitted from a discharge gap with the width d into the drift region at p_{He} = 8 Torr and dw/dx = 47 eV/cm [11], amount to w_{rs} = 47 eV. In the gap (d = 0.5–1 mm), the losses are several times lower.

Thus, the real losses of photoelectrons traveling to a collector cannot account for their self-reproduction, and the photoelectron contribution to the energy efficiency is negligibly small. Moreover, the probability of ionization of an atom by keV-energy electrons is several times the probability of excitation of a resonance state, so that a real w_s is significantly higher than the above estimate. For aluminum cathode, $\gamma_V = 0.03$ [10] and w_s additionally increases about three times.

2. The discharge cell proposed in [11–13] contains a grid structure of quartz plates with a 3×5 mm cross section and a spacing of a = 2–3 mm. The anode rods with a diameter of 2 mm are arranged on the edges of plates, at a distance of 6 mm from the cathode. It was suggested that ions recombine on the walls of the grid structure, not contributing to the anode current, and that the entire discharge current is carried by photoelectrons emitted from the cathode, with an energy efficiency of up to 99.88%.

In order to obtain a lower estimate of w_s in this system, let us assume that all ions contribute to the photoemission upon radiatively recombining on the surface of quartz plates and let the radiation losses on the plates be negligibly small. Then, unlike the case considered above, where w_s = 2.7 keV, the necessary losses amount to ~$0.5w_s$ = 1.35 keV. At an applied voltage of U = 850 V, for which the measurements gave the efficiency 99.2% [13], photoelectron discharge is principally impossible. Allowance for radiation screening by the plate walls will only increase the necessary losses w_s. Since the grid geometry is unfavorable for cathode irradiation by light from the drift region, this factor can be ignored. For atoms excited in the grid cavities

(a = 2 mm), only about 5% of the emitted radiation strikes the cathode.

Thus, the contribution of photoelectrons to the efficiency of the electron beam formation in the device under consideration is negligibly small. Moreover, the conditions of discharge studied in [11–13] cannot provide for a high efficiency at the expense of atom-induced electron emission either, even assuming that all the applied voltage drops in the cathode region. This is evidence of an incorrect method used for determining the efficiency, as confirmed [3] by a detailed analysis.

3. For comparison, let us calculate the efficiency using the formula derived [1] for γ in a usual open discharge at U = 3 kV. According to this formula, ions originating from the anode plasma and passing the cathode fall region generate (together with related fast atoms) 3.6 electrons per projectile, which corresponds to an efficiency of 78%. This estimate is valid if the entire voltage drop U is concentrated in the cathode fall region; otherwise, a real potential profile in the discharge gap has to be taken into account [1]. The description provided in [1] was justified in detail in [5], where it was pointed out that the calculations should be performed using the electron emission coefficients γ determined in a technical vacuum ($\gtrsim 10^{-7}$ Torr). Using the γ values determined under ultrahigh vacuum conditions ($<10^{-9}$ Torr), we have to neglect the emission due to fast neutrals in the range of applied voltages of interest for the open discharge, leaving only the contribution due to ionized atoms. This would result in a sharp drop of the electron beam formation efficiency. Obviously, the conditions of ultrahigh vacuum are never realized in practice, even prior to filling the discharge chamber with a working gas.

The justification given in [5] for the calculations performed in [1] can be supplemented by the following illustrative example. It was demonstrated [9] that a discharge featuring ion-induced electron emission from a cathode as the only secondary emission process cannot be initiated when the applied voltage exceeds a certain threshold. This is related to a drop in the ionizing ability of electrons in a strong electric field, caused by the electron runaway effect. For example, in helium at pd = 1.5 Torr cm, this threshold voltage amounts to ~1.5 kV [9]. This value coincides with the estimates obtained using the calculated discharge initiation curves [14, 15], which exhibit rightward bending to form a loop instead of the traditional left branch of the Paschen curve. Only allowance of the cathode bombardment with fast neutrals [14], which make the determining contribution to the electron emission, provided for a coincidence of the calculated curve with the experimental left branch of the Paschen curve. Note that the calculations in [14] were performed for the same values of emission coefficient γ [16] as those used in [1], that is, the values determined under technical vacuum conditions.

4. Thus, the above estimates show that the contribution of photoemission to the total electron emission from a cathode is negligible small. These estimates, together with the results obtained in [1–5], lead to a final conclusion: open discharge is a kind of glow discharge based, according to the commonly accepted notions, on the ionization processes and the atom-induced electron emission from the cathode. A practically important inference is that the extensive published material (more than 100 publications) concerning open discharge directly refers to glow discharge, primarily in the region of medium pressures (from several Torr up to atmospheric pressure [17]) not studied previously for the electron beams of glow discharge.

REFERENCES

1. A. R. Sorokin, Pis'ma Zh. Tekh. Fiz. **26** (24), 89 (2000) [Tech. Phys. Lett. **26**, 1114 (2000)].
2. A. R. Sorokin, Pis'ma Zh. Tekh. Fiz. **28** (9), 14 (2002) [Tech. Phys. Lett. **28**, 361 (2002)].
3. A. R. Sorokin, Pis'ma Zh. Tekh. Fiz. **29** (4), 86 (2003) [Tech. Phys. Lett. **29**, 171 (2003)].
4. A. R. Sorokin, Pis'ma Zh. Tekh. Fiz. **29** (10), 15 (2003) [Tech. Phys. Lett. **29**, 404 (2003)].
5. A. R. Sorokin, Pis'ma Zh. Tekh. Fiz. **29** (17), 1 (2003) [Tech. Phys. Lett. **29**, 701 (2003)].
6. P. A. Bokhan and G. V. Kolbychev, Zh. Tekh. Fiz. **51**, 1823 (1981) [Sov. Phys. Tech. Phys. **26**, 1057 (1981)].
7. A. R. Sorokin, Pis'ma Zh. Tekh. Fiz. **21** (20), 37 (1995) [Tech. Phys. Lett. **21**, 832 (1995)].
8. A. R. Sorokin, Zh. Tekh. Fiz. **68** (3), 33 (1998) [Tech. Phys. **43**, 296 (1998)].
9. S. V. Arlantsev, B. L. Borovich, V. V. Buchanov, *et al.*, J. Russ. Laser Res. **16** (2), 99 (1995).
10. M. A. Zav'yalov, Yu. E. Kreĭndel', A. A. Novikov, and L. P. Shanturin, *Plasma Processes in Electron Guns* (Énergoatomizdat, Moscow, 1989).
11. A. P. Bokhan and D. É. Zakrevskiĭ, Pis'ma Zh. Tekh. Fiz. **28** (11), 21 (2002) [Tech. Phys. Lett. **28**, 454 (2002)].
12. P. A. Bokhan and D. E. Zakrevsky, Appl. Phys. Lett. **81**, 2526 (2002).
13. A. P. Bokhan and D. É. Zakrevskiĭ, Pis'ma Zh. Tekh. Fiz. **28** (2), 74 (2002) [Tech. Phys. Lett. **28**, 73 (2002)].
14. K. N. Ul'yanov and V. V. Chulkov, Zh. Tekh. Fiz. **58**, 328 (1988) [Sov. Phys. Tech. Phys. **33**, 201 (1988)].
15. A. N. Tkachev and S. I. Yakovlenko, Pis'ma Zh. Éksp. Teor. Fiz. **77** (5), 264 (2003) [JETP Lett. **77**, 221 (2003)].
16. H. C. Hayden and N. G. Utterback, Phys. Rev. **135**, A1575 (1964).
17. A. R. Sorokin, Pis'ma Zh. Tekh. Fiz. **29** (9), 42 (2003) [Tech. Phys. Lett. **29**, 373 (2003)].

Translated by P. Pozdeev

Technical Physics Letters, Vol. 29, No. 10, 2003, pp. 838–840. Translated from Pis'ma v Zhurnal Tekhnicheskoĭ Fiziki, Vol. 29, No. 20, 2003, pp. 5–11.

Peculiarities of the Electric Conductivity of $As_2S_3\langle Au\rangle$ and $As_2S_5\langle Au\rangle$ Glasses

A. A. Babaev, I. K. Kamilov, P. P. Khokhlachev, S. B. Sultanov*, and E. I. Terukov

Institute of Physics, Dagestan Scientific Center, Russian Academy of Sciences, Makhachkala, Dagestan, Russia

Ioffe Physicotechnical Institute, Russian Academy of Sciences, St. Petersburg, 194021 Russia

** e-mail: sult@datacom.ru*

Received May 7, 2003

Abstract—The temperature dependences of the dc conductivity in glasses of the $(As_2S_3)_{1-x}Au_x$ and $(As_2S_5)_{1-x}Au_x$ systems (0.04 at. % $\geq x \geq 0$) are reported for the first time. The curves show an anomalous behavior in the temperature interval of 360 K > T > 300 K and exhibit a break for glass compositions with a low gold content. A model explaining the existence of impurity conductivity is proposed. © *2003 MAIK "Nauka/Interperiodica".*

Introduction. As is known, the electric conductivity of semiconducting chalcogenide glasses significantly decreases upon the transition from crystalline to glassy state and becomes independent of the concentration of impurities. In the glassy state, the temperature dependence of the conductivity exhibits no characteristic break reflecting the change from intrinsic to impurity conductivity. The absence of this break, that is, the lack of the electrical activity of impurities in glassy samples, was explained [1, 2] by the fact that all valence electrons of dopant atoms in a disordered structure are involved in the formation of bonds with the neighboring atoms. As a result, the character of an impurity (donor or acceptor) is not manifested in the glassy material.

The influence of metal impurities on the physical properties of chalcogenide glasses were mostly studied in stoichiometric compositions, which typically (with few exceptions) exhibit increased susceptibility to crystallization. The amount of a dopant was usually so large that it was difficult to decide whether an increase in the conductivity is related to the appearance of impurity energy levels or to a decrease in the bandgap width of the semiconductor (representing essentially a new compound). However, there are some data showing that impurities can significantly affect the physical properties of chalcogenide glassy semiconductors [3]. Although the number of investigations devoted to the behavior of impurities in chalcogenide glasses is continuously increasing, the main problems related to the search for impurities effectively influencing the properties of these materials and to the explanation of anomalous behavior observed for most of the other impurities still remain unsolved.

Previously [4, 5], we reported on the new emission bands in the photoluminescence spectra of nonstoichiometric $GeS_3\langle Bi\rangle$ and $As_2S_5\langle Au\rangle$ glasses with small concentrations of impurities. These preliminary results stimulated further investigations aimed at determining the temperature dependence of conductivity in these glassy semiconductors of both stoichiometric and nonstoichiometric compositions of the $(As_2S_3)_{100-x}Au_x$ and $(As_2S_5)_{100-x}Au_x$ systems with 0.04 at. % $\geq x \geq 0$. To our knowledge, no special investigations of the effect of minor impurities on the conductivity of stoichiometric and nonstoichiometric glasses have been reported so far.

Experimental. The glassy semiconductors were synthesized by alloying the initial high-purity (not worse than 99.999%) components in evacuated (10^{-4} Torr) quartz ampules. The process was conducted for 4 h at 950°C with continuous stirring, after which the samples were quenched in air. The glassy state was identified by the amorphous character of the X-ray diffraction, a conchoidal fracture pattern, and the absence of microinclusions on the sample surface examined in a microscope of the Neofot type.

The dc conductivity σ of the synthesized glasses was measured using the method of pressed contacts. According to this, plane-parallel plates with a thickness of d = 0.85–2 mm were pressed between soft graphite disks (10 mm in diameter) tightly fixed in copper holders. The resistance of a disk with the holder was 0.2 Ω and leakage currents were minimized.

Results and discussion. Figures 1 and 2 show the experimental temperature dependences of the electric conductivity of glasses of the two systems studied. The conductivity of undoped As_2S_3 and As_2S_5 obeys the law $\sigma = \sigma_0 \exp(-E_a/kT)$ with the same activation energy. The curves of the samples with a gold content of x =

0.00001 at. % and above exhibit breaks and, hence, are characterized by two activation energies.

As the gold content increases to 0.01 at. %, the conductivity of all glasses grows by two orders of magnitude, the activation energy drops by 0.3 eV, and the softening temperature decreases by 20 K and 10 K in As_2S_3 and As_2S_5 based glasses, respectively. Note that the doped compositions containing 0.02 at. % gold, as well as the undoped As_2S_3 and As_2S_5 glasses, are characterized by a single activation energy. In the temperature interval of 360 K > T > 300 K, the curves of doped glasses exhibit an anomaly, whereby the conductivity significantly increases with the temperature, passes through a maximum, and sharply drops to a minimum level, which is several orders of magnitude lower than 10^{-11} Ω^{-1} cm^{-1}. As the temperature increases further (T > 360 K), the conductivity of doped glasses increases again (with two activation energies). It should be noted that repeated measurements of the $\sigma(T)$ curve for the same sample lead to disappearance of the conductivity in the temperature interval of 360 K > T > 300 K after several heating–cooling cycles.

These experimental results are indicative of the appearance of an electrically active impurity level and the usual impurity conductivity related to this level. Below we describe a possible qualitative pattern explaining the temperature behavior of conductivity, in particular, the appearance of the second slope.

In a disordered structure, the distances between neighboring atoms exhibit random variations. Small fluctuations of the interatomic distances are equiprobable with respect to both contraction and extension. However, a strong increase in the repulsion between atoms for relatively large deviations makes the situation of strong extension more probable. This extension is related to the incorporation of Au atoms with a large atomic radius into the glass structure. Let us attribute all changes in the density of a sample in the glassy state to the presence of large extensions. The density of samples containing Au impurity is lower by several percent than that of the initial (undoped) composition. Assuming the difference to be entirely due to the presence of extended regions (microvoids), we can estimate the total volume fraction of these voids as $(\rho_I - \rho_L)/\rho_I \approx 0.01$, where ρ_I and ρ_L are the densities of initial and doped glassy semiconductors. Occurring at the boundary of such a microvoid, a dopant atom (in our case, Au atom) cannot use all valence electrons for forming bonds (at least, because the nearest neighbor on one side is at a distance exceeding the characteristic bond length). Thus, the dopant atom occurring in the microvoid can create an electrically active impurity level. This impurity level will be "bound" to the edge of an energy band responsible for a decrease in the bandgap width E_g, since both the appearance of the new level and the decrease in E_g are related to the bonds between the dopant atom and the matrix atoms. The former effect is caused by a small fraction of dopant atoms falling within the microvoids, while the latter effect is produced by the major fraction of dopant atoms incorporating into the volume and saturating all their valence bonds.

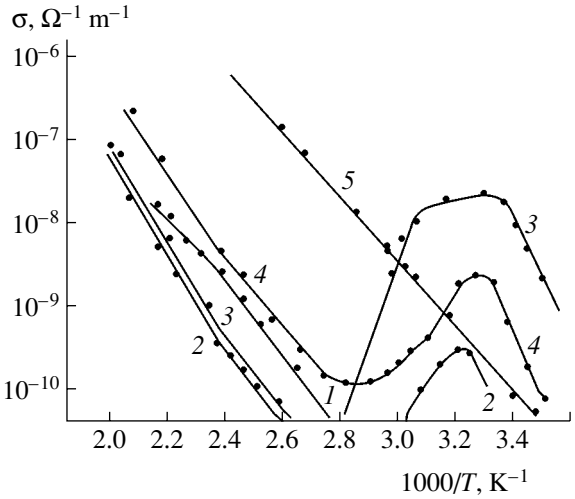

Fig. 1. The temperature dependence of the dc conductivity for glasses of the $(As_2S_3)_{1-x}Au_x$ system with various x (at. %): (*1*) 0; (*2*) 0.00001; (*3*) 0.0001; (*4*) 0.01; (*5*) 0.02.

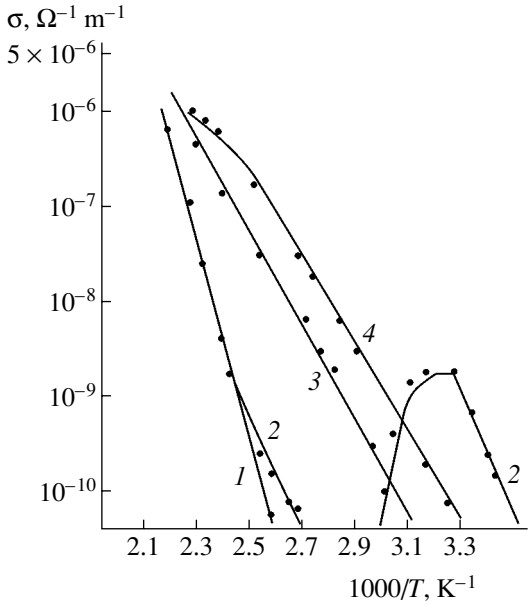

Fig. 2. The temperature dependence of the dc conductivity for glasses of $(As_2S_5)_{1-x}Au_x$ system with various x (at. %): (*1*) 0 and 0.00001; (*2*) 0.0001; (*3*) 0.02; (*4*) 0.04.

A reduction in the density of slightly doped glasses leads initially to a decrease in the conductivity. As the concentration of impurity grows further, the material density apparently begins to increase (Fig. 3). Figure 3 shows plots of the conductivity versus doping level x for glasses of the $(As_2S_3)_{1-x}Au_x$ system; analogous curves were obtained for the $(As_2S_5)_{1-x}Au_x$ system. Note that the conductivity of a glassy semiconductor

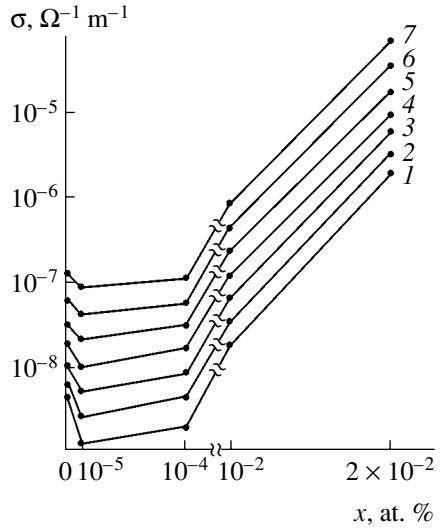

Fig. 3. Plots of the conductivity versus doping level x for glasses of the $(As_2S_3)_{1-x}Au_x$ system measured at various temperatures (K): (*1*) 433.8; (*2*) 449.3; (*3*) 459.6; (*4*) 469.7; (*5*) 479.8; (*6*) 489.7; (*7*) 499.5.

with the composition $(As_2S_3)_{0.99999}Au_{0.00001}$ is lower than that of the initial As_2S_3 glass. We believe that donor- and acceptor-like centers in the doped glasses appear in pairs. Such pairs probably comprise an Au^+ ion (donor) and a charged dangling bond D^- occurring at the opposite ends of the same microvoid. At a small impurity concentration, these pairs do not annihilate: elimination of a microvoid requires simultaneous rearrangement of a large number of atoms. Such a rearrangement more probably takes place at increased impurity concentrations and corresponds to the curves with a single activation energy.

Conclusions. In the cases under consideration, the major proportion of dopant atoms incorporated into the glass matrix saturate their valence bonds. Such atoms are electrically inactive and form a series of solid solutions with decreased semiconductor bandgap width. A small fraction of dopant atoms, falling within the microvoids, cannot saturate their valence bonds and remain electrically active. These dopant atoms lead to the formation of an impurity level responsible for the impurity conductivity. Since the impurity level formation and the bandgap width reduction are related to atoms of the same impurity (differing only by the nearest environment), the new level has to be "bound" to the edge of an energy band responsible for a decrease in the bandgap width E_g.

Apparently, the optical bandgap width and the dc conductivity activation energy have to monotonically decrease with increasing x, while the difference between these values must remain constant. This rule, observed in the films deposited by RF magnetron cosputtering [6], was predicted in [7]. In order to confirm the existence of impurity conductivity in gold-doped glasses, it is necessary to measure the optical bandgap width and check for the aforementioned rule in bulky chalcogenide glassy semiconductors.

Thus, the proposed model of doping relates the appearance of electrically active impurity states to the formation of rigid microscopic regions (microvoids) in bulk chalcogenide glassy semiconductors, the structure of which hinders saturation of all valence bonds of a dopant atom falling within such a microvoid.

Acknowledgments. This study was supported by the Russian Foundation for Basic Research, project no. 03-02-17598.

REFERENCES

1. A. I. Gubanov, Zh. Tekh. Fiz. **27**, 2510 (1957) [Sov. Phys. Tech. Phys. **2**, 2335 (1957)]; Fiz. Tverd. Tela (Leningrad) **3**, 2336 (1961) [Sov. Phys. Solid State **3**, 1694 (1961)].
2. N. Mott, Adv. Phys. **16**, 49 (1967).
3. K. D. Tsendin, *Electron Phenomena in Glass-Like Semiconductors* (Nauka, St. Petersburg, 1996).
4. A. A. Babaev, S. B. Sultanov, and A. M. Askhabov, in *Proceedings of the 2nd International Conference on Amorphous and Microcrystalline Semiconductors, St. Petersburg, 2000*, p. 119.
5. A. A. Babaev, T. N. Mamontova, and E. I. Terukov, Fiz. Khim. Stekla **8** (5), 135 (1992).
6. T. F. Mazets and K. D. Tsendin, Fiz. Tekh. Poluprovodn. (Leningrad) **24**, 1953 (1990) [Sov. Phys. Semicond. **24**, 1214 (1990)].
7. B. L. Gel'mont and K. D. Tsendin, Fiz. Tekh. Poluprovodn. (Leningrad) **17**, 1040 (1983) [Sov. Phys. Semicond. **17**, 655 (1983)].

Translated by P. Pozdeev

Technical Physics Letters, Vol. 29, No. 10, 2003, pp. 841–842. Translated from Pis'ma v Zhurnal Tekhnicheskoĭ Fiziki, Vol. 29, No. 20, 2003, pp. 12–15.

Spherical Silicon Nanoparticles Formed in Aluminum Melt

Yu. P. Volkov, V. B. Baiburin*, and N. P. Konnov

Saratov State Technical University, Saratov, Russia

** e-mail: bai@sstu.saratov.su*

Received March 25, 2003; in final form, May 28, 2003

Abstract—Nanoparticles formed from silicon dissolved in melted aluminum were observed by transmission electron microscopy. The nanoparticles possess a spherical shape with the diameter ranging from several dozen nanometers to 1.5 nm. © *2003 MAIK "Nauka/Interperiodica".*

In recent years, there has been considerable interest in studying carbon structures with characteristic dimensions on a nanometer scale (nanotubes, fullerenes, etc.) [1], developing new methods for the synthesis of such nanostructures, and searching for possible fields of application. Although silicon is also theoretically capable of forming such structures [2], no data on the observation of spherical silicon nanoparticles have been reported so far to the best of our knowledge.

Below, we describe a method for obtaining spherical silicon nanoparticles and present the results of investigation of such structures by transmission electron microscopy (TEM). The proposed method is based on the well-known phenomenon whereby solid silicon dissolves in the melts of some metals, in particular, aluminum [3]. The choice of aluminum is related to the absence of a chemical interaction between dissolved silicon and the solvent [3], which excludes the formation of new compounds.

A small amount (~0.04 g) of a high-purity aluminum (99.99% Al) was placed onto the surface of a polished single crystal plate cut from an 0.38-mm-thick (111)-oriented EDKB-10-2b grade silicon wafer. The plate was placed into a vacuum deposition system (Hitachi HUS 5GB) and heated by electric current (~10–20 A) up to the melting temperature of aluminum in a vacuum on the order of 10^{-5} Torr. When the metal was melted, the current was immediately switched off, the melt was allowed to cool, and the plate was extracted from the vacuum chamber. Then, the aluminum was etched in a large amount of a 60% solution of hydrochloric acid (reagent grade) in distilled water (the process was carried out for five days). As a result, the aluminum ball was completely etched off to leave a porous silicon ball.

This silicon ball was isolated from the etchant and repeatedly rinsed in distilled water in order to remove residual acid and water-soluble aluminum salts. Finally, the ball was destroyed by ultrasonic treatment (44 kHz, 10 min) in distilled water and a drop of this suspension was placed onto a copper grid for electron microscopy coated with a ~20 nm thick Formvar film. The samples were dried in air and studied in a transmission electron microscope (Hitachi HU-12A) with a nominal resolution of 0.2 nm, operating at an accelerating voltage of 75 kV.

The results of TEM observations revealed, besides silicon fragments of irregular shapes and various dimensions, a significant amount of rounded and spherical particles with sizes ranging from several thousand to a few nanometers. Figure 1a presents an electron micrograph displaying spherical silicon nanoparticles and Fig. 1b shows the pattern of electron microdiffraction from such particles. The latter pattern consists of two parts, one obtained at a small exposure to reveal the structure of inner rings and the other at a large exposure to image the less intense external rings. The interplanar spacings (calculated using the middle diameters of the diffraction rings determined with a ~10% accuracy) amount to 0.33 nm (111), 0.19 nm (220), 0.16 nm (311), 0.12 nm (422), and 0.093 nm (531). Owing to the close diameters of the (211) and (311) rings and a large difference in brightness, the two rings probably appear as merged into one. The tabulated values [4] of interplanar spacings are as follows: 0.3138 nm (111), 0.1920 nm

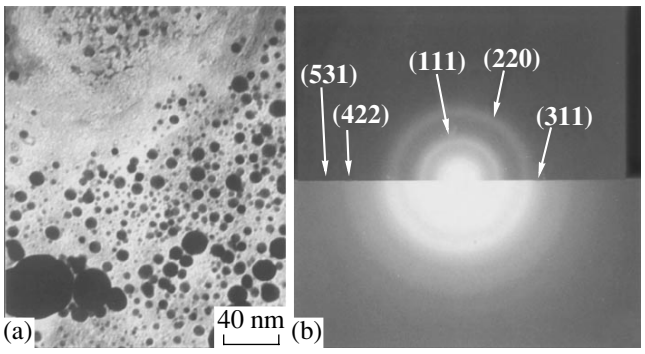

Fig. 1. (a) A TEM micrograph showing nanoparticles of various dimensions formed from silicon dissolved in melted aluminum (top right corner displays silicon particles of irregular shape); (b) the pattern of electron microdiffraction from spherical silicon nanoparticles.

1063-7850/03/2910-0841$24.00 © 2003 MAIK "Nauka/Interperiodica"

(220), 0.1638 nm (311), 0.1108 nm (422), and 0.0918 nm (531).

The diffraction rings also display point reflections due to silicon crystals of various orientations. The point reflections observed in the vicinity of the (111) ring correspond to the following interplanar spacings (determined to within 3%): reflections on the ring, 0.308 nm (close to a tabulated value for the (111) plane); and a remote reflection, 0.27 nm. Some diffraction patterns exhibited reflections on the internal side of the (111) ring, which corresponded to a distance of 0.373 nm. The presence of reflections corresponding to distances different from those known in silicon is probably related to the residual aluminum chloride formed in the course of etching and not removed by rinsing. The point reflections on the (220) ring correspond to the interplanar spacing of 0.185 nm, and a more distant reflection, to 0.17 nm (close to the tabulated values for the (222) and (311) planes, respectively).

The dimensions of small nanoparticles were close to the theoretically calculated diameters of silicon fullerenes Si_{60} (1.5 nm [2]), while coarse particles seem to represent a "silicon soot" analogous to the carbon soot known to be composed of spherical particles [5]. We believe that further investigation into the structure and properties of spherical silicon nanoparticles will show whether they possess a regular structure analogous to that of carbon fullerenes.

REFERENCES

1. R. F. Curl and R. E. Smalley, Sci. Am., No. October, 54 (1991).
2. Bao-Xing Li, Pei-Lin Cao, and Duan-Lin Que, Phys. Rev. B **61**, 1685 (2000).
3. M. Hansen and K. Anderko, *Constitution of Binary Alloys* (McGraw-Hill, New York, 1958; Metallurgizdat, Moscow, 1962).
4. L. I. Mirkin, *Handbook of X-ray Analysis of Polycrystalline Materials* (Plenum Press, New York, 1964; Fizmatgiz, Moscow, 1961).
5. V. I. Berezkin, Fiz. Tverd. Tela (St. Petersburg) **42**, 567 (2000) [Phys. Solid State **42**, 580 (2000)].

Translated by P. Pozdeev

Technical Physics Letters, Vol. 29, No. 10, 2003, pp. 843–845. Translated from Pis'ma v Zhurnal Tekhnicheskoĭ Fiziki, Vol. 29, No. 20, 2003, pp. 16–20.

Calculation of the Stress Intensity Factor for a Hydrogenated Plastic Crystal with a Crack

D. N. Karpinskiĭ* and S. V. Sannikov

Institute of Mechanics and Applied Mathematics, Rostov State University, Rostov-on-Don, 344104 Russia

** e-mail: karp@math.rsu.ru*

Revised manuscript received June 4, 2003

Abstract—Time variation of the stress intensity factor in the tensile mode is calculated for a hydrogenated plastic crystal with a crack. The calculation takes into account the influence of dissolved interstitial hydrogen on the evolution of plastic deformation at the crack tip, determined by the competition of mechanisms related to (i) incommensurate dimensions of dissolved hydrogen atoms and interstitial voids in the crystal lattice and (ii) a decrease in the yield point caused by the hydrogen-induced plasticity. The numerical results for an α-Fe crystal are presented. © *2003 MAIK "Nauka/Interperiodica".*

The results of investigations performed in recent years elucidated some peculiarities in the pattern of crack growth in hydrogenated metals [1]. In particular, it was established that the formation of dislocation pileups at the crack tip in a crystal proceeds under the action of the total stress created by the crack, the dislocations formed in the plastic zone, and the interstitial hydrogen atoms [2, 3]. The dissolved hydrogen produces "screening" of elastic fields of the crack and dislocations in the vicinity of the crack tip.

This study was aimed at estimating the effect of hydrogen dissolved in a body centered cubic (bcc) crystal on the evolution of plastic deformation at the crack tip. The analysis is performed in terms of the notions formulated in [3]. Previously [4], we performed an analogous calculation based on the model [5] taking into account the plasticizing effect of interstitial hydrogen. It was of interest to compare the results of calculations performed within the framework of models [3] and [5]. It should be noted that dissolved hydrogen produces a two-fold action upon the development of plastic straining. On the one hand, compressive elastic stresses due to interstitial hydrogen atoms (dilatation mechanism) produce screening of the elastic fields of the crack and dislocations, thus reducing the mobility of the latter; on the other hand, the dissolved hydrogen decreases the yield point (plasticization mechanism), thus increasing the mobility of dislocations. This paper is devoted to an analysis of the competitive influence of the two mechanisms.

Let us consider a two-dimensional problem concerning evolution of the plastic deformation at the tip of a crack with a length of $2l$ situated in the {100} cleavage plane of an infinite bcc crystal with a lattice parameter a. A homogeneous tensile stress $\sigma_a(t)$ (mode 1) applied to the crystal planes $y = \pm\infty$ is monotonically increased up to a certain limit sufficient for plastic straining of the crystal but not for initiating the crack growth. When the load $\sigma_a(t)$ reached this maximum level σ_{max}, the calculation was performed in the regime of stress relaxation at the crack tip, which corresponds to a constant external tensile stress. The crystal is assumed to contain uniformly distributed sources of dislocations emitting rectangular loops in the easy slip planes. The concentration of stresses at the crack tip, followed by their relaxation through plastic deformation, results in a considerable density of effective dislocations in this region (excess dislocations of the same sign among those with parallel Burgers vectors), which gives rise to an elastic field significantly influencing the development of plastic straining.

In what follows, we assume that plastic deformation of the bcc crystal proceeds by the mechanism of the thermoactivated slip of perfect dislocations with the Burgers vector $\mathbf{b} = a/2\langle 111\rangle$ along the easy slip planes {100} (mixed dislocations). The calculation takes into account only edge components of the mixed dislocations. Intersecting the $0xy$ plane, the {100} planes form two families of the slip lines in the directions determined by the vectors $\mathbf{b}_k$ ($k = 1, 2$).

The rate of the plastic deformation caused by the motion of dislocations at the crack tip is [6]

$$\frac{d\varepsilon^k(\mathbf{r}, t)}{dt} = \dot{\varepsilon}_0 \exp\left[-\frac{U_0\{1 - [\sigma_e^k(\mathbf{r}, t)/\tau_0]^{1/2}\}}{k_B T(\mathbf{r}, t)}\right] \operatorname{sgn}\sigma_e^k(\mathbf{r}, t), \quad (1)$$

where U_0 is the activation energy, k_B is the Boltzmann constant, T is the absolute temperature, and $\dot{\varepsilon}_0$ and τ_0

1063-7850/03/2910-0843$24.00 © 2003 MAIK "Nauka/Interperiodica"

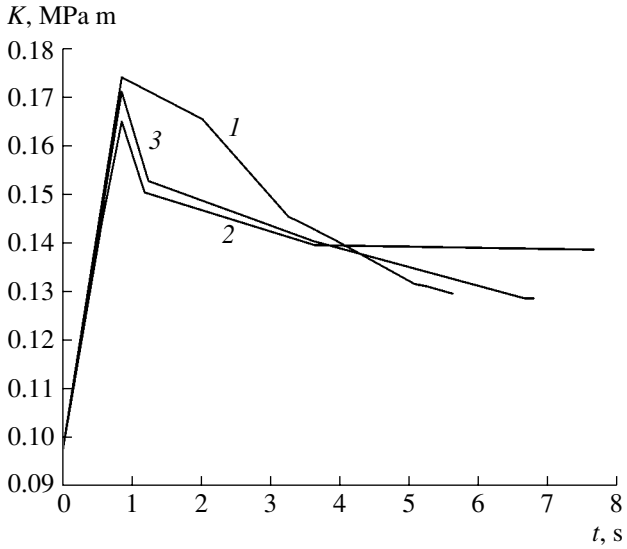

Time variation of the stress intensity coefficient for a plastic crack in a bcc crystal containing interstitial hydrogen atoms with an initial concentration of $c_0 = 1.25 \times 10^{-4}$. The calculations were performed (*1*) with neglect of the hydrogen-induced plasticity, or (*2*) with neglect of the dilatation effect caused by interstitial hydrogen, or (*3*) with both these mechanisms taken into account.

are constant coefficients. The effective stress $\sigma_e^k(\mathbf{r}, t)$ in the easy slip planes is determined as [7–9]

$$\sigma_e^k(\mathbf{r}, t) = \sigma^k(\mathbf{r}, t) - \sigma_s(\mathbf{r}, t)\,\mathrm{sgn}\,\sigma^k(\mathbf{r}, t) \quad \text{for } |\sigma^k(\mathbf{r}, t)| > |\sigma_s(\mathbf{r}, t)|; \qquad (2)$$

$$\sigma_e^k(\mathbf{r}, t) = 0 \quad \text{for } |\sigma^k(\mathbf{r}, t)| < |\sigma_s(\mathbf{r}, t)|,$$

where

$$\sigma^k(\mathbf{r}, t) = \sigma_k^c(\mathbf{r}, t) + \sigma_k^l(\mathbf{r}, t) + \sigma_k^t(\mathbf{r}, t) \qquad (3)$$

is the shear stress in the planes of easy slip and

$$\sigma_s(\mathbf{r}, t) = \sigma_0 + \sigma_f(\mathbf{r}, t) \qquad (4)$$

represents the stress opposing the plastic shear, which is related to the lattice friction σ_0 and the local straining σ_f of the material; $\sigma_k^c(\mathbf{r}, t)$ is the Westergard stress; $\sigma_k^l(\mathbf{r}, t)$ is the long-range elastic stress created by dislocations of the same sign in the plastic zone; and $\sigma_k^i(\mathbf{r}, t)$ is the elastic shear stress produced by interstitial hydrogen atoms [3].

The migration of interstitial hydrogen atoms under the action of a hydrostatic component of the effective stress tensor $\sigma_{ii}^e(\mathbf{r}, t)$ is described by the equation of mechanodiffusion (see, e.g., [4]),

$$\frac{\partial c(\mathbf{r}, t)}{\partial t} = D\nabla^2 c(\mathbf{r}, t) + \frac{Dc(\mathbf{r}, t)}{k_B T(\mathbf{r}, t)} \nabla c(\mathbf{r}, t) \nabla V(\mathbf{r}, t), \qquad (5)$$

where D is the diffusion coefficient, $V(\mathbf{r}, t) = \Delta v \sigma_{ii}^e(\mathbf{r}, t)$, Δv is a change in the unit cell volume related to the presence of interstitials in the crystal lattice. The initial and boundary conditions for Eq. (5) were formulated by analogy with those used in [4]. Finally, it is assumed that a crack is filled by the ideal gas.

By jointly solving Eqs. (1)–(5), we determined distributions of the effective stresses $\sigma_e^k(\mathbf{r}, t)$ and the concentration of interstitial hydrogen $c(\mathbf{r}, t)$ at various moments of time *t*. The calculation was performed for a preset value of the maximum crack tip stress intensity factor $K_I^{\max}$ (upon reaching this value, the load on the crystal remained constant) and terminated at the time $t = t_f$ such that $\sigma_e^k(\mathbf{r}, t_f) = 0$ in the entire vicinity of the crack tip.

The evolution of plastic deformation and the migration of interstitial hydrogen at the crack tip in a loaded crystal of α-Fe were calculated for the following parameters: $2l = 10^{-3}$ m; $K_I^{\max} = 0.2$ MPa m$^{1/2}$; $a = 2.876 \times 10^{-10}$ m; $U_0 = 0.9$ V; $\tau_0 = 330$ MPa; $\sigma_0 = 18$ MPa [6]; $T = 300$ K; $D = 4.88 \times 10^{-12}$ m^2/s [10]; $Dv = 3 \times 10^{-30}$ m^3; the other parameters were selected as in [4].

Based on these data, we calculated the time variation of the stress intensity factor. It was assumed that the crack tip stress intensity factor can be expressed as [4, 7]

$$K(t) = K^c(t) + K^p(t) + K^i(t), \qquad (6)$$

where $K^c(t)$ is the stress intensity factor with neglect of the plastic deformation at the crack tip, $K^p(t)$ is a correction for the plastic deformation, and $K^i(t)$ is the contribution due to stresses generated by interstitial hydrogen [3].

The time variation of the stress intensity factor calculated for a crystal containing interstitial hydrogen atoms with an initial concentration of $c_0 = 1.25 \times 10^{-4}$ is shown in the figure. The calculations were performed with neglect of the plasticization mechanism (curve *1*) or the dilatation mechanism (curve *2*), or with both mechanisms taken into account (curve *3*). The final points of these curves correspond to the time of arrest (t_f) of the development of plastic deformation (ε^k). A comparison of curves *1–3* shows that neglect of the plasticization mechanism significantly decreases the stress relaxation at the crack tip and the time to arrest of the plastic deformation. Allowance of the plasticization mechanism leads to a significant decrease in the stress intensity factor (≈5%, cf. curves *2* and *3*) at the moment of maximum loading t_m. Note also that the plasticization mechanism significantly (by ~20%) increases the maximum deformation $\varepsilon_{\max}$ in the plastic zone. From this we conclude that, for the physical parameters selected, the plasticization mechanism plays the main

role in the evolution of plastic deformation at the crack tip in a hydrogenated crystal.

REFERENCES

1. Eng. Fract. Mech. **68** (4) (2001).
2. T. Magnin, A. Chambreuit, and J. P. Chateau, Int. J. Fract. **79**, 147 (1996).
3. J. P. Chateau, D. Delafosse, and T. Magnin, Acta Mater. **50**, 1523 (2002).
4. D. N. Karpinskiĭ and S.V. Sannikov, Fiz. Tverd. Tela (St. Petersburg) **42**, 2171 (2000) [Phys. Solid State **42**, 2236 (2000)].
5. N. M. Vlasov and V. A. Zaznoba, Fiz. Tverd. Tela (St. Petersburg) **41**, 451 (1999) [Phys. Solid State **41**, 404 (1999)].
6. W. A. Spitzig, Acta Metall. **18**, 1275 (1970).
7. D. N. Karpinskiĭ and S. V. Sannikov, Prikl. Mekh. Tekh. Fiz. **34** (3), 154 (1993).
8. D. N. Karpinskiĭ and S. V. Sannikov, Fiz. Tverd. Tela (St. Petersburg) **37**, 505 (1995) [Phys. Solid State **37**, 273 (1995)].
9. D. N. Karpinskiĭ and S. V. Sannikov, Fiz. Met. Metalloved. **85** (2), 121 (1998).
10. F. R. Brotzen and A. Seeger, Acta Metall. **37**, 2985 (1989).

Translated by P. Pozdeev

Technical Physics Letters, Vol. 29, No. 10, 2003, pp. 846–847. Translated from Pis'ma v Zhurnal Tekhnicheskoĭ Fiziki, Vol. 29, No. 20, 2003, pp. 21–25.

Temperature Waves in a Horizontal Liquid Layer Cooled from Above

I. A. Ermolaev and A. I. Zhbanov*

Saratov State University, Saratov, Russia

** e-mail: ZhbanovAl@info.sgu.ru*

Received May 12, 2003

Abstract—Waves in a thermal boundary layer were obtained by numerically modeling the natural thermogravitational convection in the infinite horizontal layer of a liquid cooled from above. The waves are generated via a mechanism related to the loss of stability and periodic separation of the upper, heavier and cooler liquid layer (penetrative convection). *© 2003 MAIK "Nauka/Interperiodica".*

Perturbations developed in a convective flow may acquire the form of periodic waves traveling down the flow in a thermal boundary layer. In the case of a thermogravitational convection, these waves were experimentally observed [1, 2] and numerically modeled [3] in a vertical liquid layer. Analogous waves in oblique layers were studied in [4]. The temperature waves generated under the conditions of a confined boundary layer were experimentally observed in [5, 6] and numerically modeled in [7, 8].

In our study, oscillatory regimes accompanied by the generation of temperature waves in a boundary layer were obtained by numerical modeling of thermogravitational convection in the horizontal layer of a liquid cooled from above. This situation corresponds to the Rayleigh–Benard problem in a formulation different from classical: the lower boundary is maintained at a constant temperature and the upper boundary is characterized by constant heat removal, both boundaries being solid and impermeable.

In order to determine the flow and temperature fields, we used dimensionless, nonstationary two-dimensional convection equations in the Boussinesq approximation, written in the velocity vortex–stream function–temperature variables [9]. The scales of length, time, velocity, and temperature are represented by H, H^2/ν, ν/H, and q_0H/λ, where H is the layer thickness, ν is the kinematic viscosity coefficient of the liquid, λ is the thermal conductivity of the liquid, and q_0 is the thermal flux scale. The infinite layer was modeled using a convective cell with a horizontal size L, symmetric boundary conditions on the side walls, and adherence conditions on the horizontal boundaries.

The problem was solved by the Galerkin method of finite elements in a weak formulation. The temperature, velocity vortex, and stream function were approximated by a linear combination of time-independent basis set functions (form functions) on linear triangle finite elements. The time approximation was performed within a fully implicit scheme. The Boussinesq equations were solved by sequential time steps, each beginning with the calculation of a temperature field. This was followed by determination of the boundary conditions for the velocity vortex (Woods' formula) and solving the corresponding equation. Finally, the velocity vortex field was corrected and the stream function field was determined. The algorithm was implemented as a finite element program and employed as described in [10].

The numerical calculations were performed for a liquid with the Prandtl number Pr = 100 ($\mathrm{Pr} = \nu/\chi$, where χ is the thermal diffusivity). The dimensionless temperature on the lower boundary was $\theta = 0$ and the dimensionless density of the thermal flux on the upper boundary was $q_0 = -1$. Variable parameters included the modified Grashof number Gr and the L/H ratio ($\mathrm{Gr} = g_y\beta q_0 H^4/\lambda\nu^2$, where g_y is the gravitational acceleration component across the flow and β is the temperature coefficient of volume expansion).

At the initial moment of time, the equilibrium liquid layer was subjected to thermal perturbation of a special type forming a double-vortex flow in the convection cell, in which "warmer" volumes of liquid were ascending along the side walls, while "colder" volumes were descending at the center. At small Gr and L/H values, a stationary spatiotemporal "roll" convection was established in the system. An increase in the Grashof number and the relative cell length led to the appearance of and increase in the asymmetry of vortices. Finally, at Gr = 50 and $L/H = 2.75$, waves in the thermal boundary layer appeared in the establishment stage. As the layer was cooled, the waves exhibited damping and only at $\mathrm{Gr} \geq 250$ and $L/H \geq 3.25$ a self-sustained oscillatory regime was observed. A relatively low Grashof number (Gr = 250 at Pr = 100) allows the flow to be considered as two-dimensional. Further increase in the L/H value led to breakage of the double-vortex flow pattern and the

1063-7850/03/2910-0846$24.00 © 2003 MAIK "Nauka/Interperiodica"

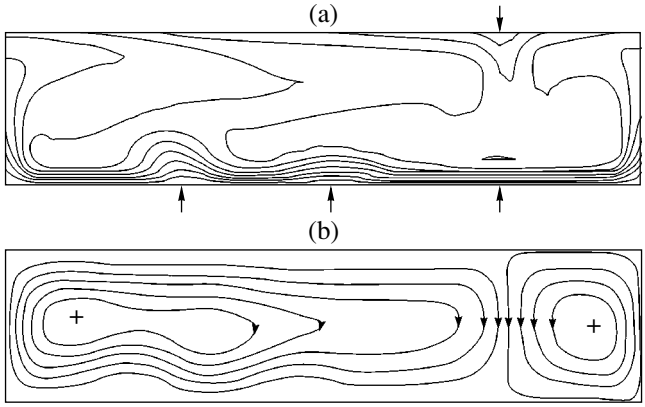

Fig. 1. Instantaneous values of the (a) temperature and (b) flow fields for Gr = 250 and $L/H = 3$.

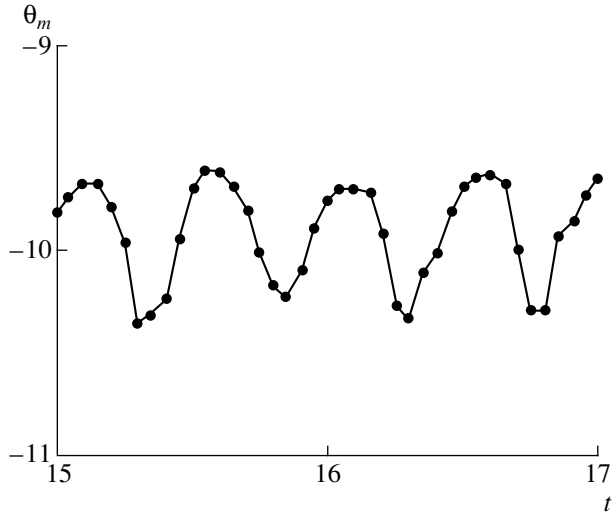

Fig. 2. Time variation of the minimum dimensionless temperature in a system with Gr = 250 and $L/H = 3.25$.

formation of three or four vortices in the cell already at $L/H = 3.5$.

It should be noted that the mechanism of the temperature wave generation in the boundary layer under consideration is related to the cyclic separation of convection elements (called thermics) from the cooled surface and is caused by instability of the upper, cooler and heavier liquid layer. The temperature waves appear provided that the convection cell is sufficiently long (i.e., that the horizontal size of a vortex is sufficiently large), which is due to a relatively slow development of oscillatory perturbations. Thus, the domain of existence of the regime of self-sustained oscillations accompanied by the generation of temperature waves in the boundary layer in the space of Gr and L/H variables is rather small. This domain is bounded with respect to L/H by a slow growth of the oscillatory perturbations, on the one hand, and by the instability of vortices with large horizontal dimensions, on the other hand.

Figure 1 shows (a) isotherms and (b) stream lines of the temperature and flow fields, respectively, at a certain time in the establishment stage for Gr = 250 and $L/H = 3$. A minimum in the temperature profile is observed on the upper boundary at the thermic base (indicated by the arrow on top). The problem formulation and parameters provide for the existence of a rather thin thermal boundary layer at the lower boundary (Fig. 1a), which becomes unstable with respect to thermal perturbations related to the periodic separation and descent of the colder (and, hence, heavier) liquid layer. Figure 1a shows a moment corresponding to the motion (right to left) of two waves and the onset of formation of the third wave (indicated by arrows at the lower boundary). The wave velocity is about 6 dimensionless units (for a 10^{-2} m thick layer of transformer oil, this velocity amounts to approximately 6×10^{-4} m/s).

Figure 2 shows the pattern of established oscillations of a minimum dimensionless temperature. The period of these oscillations, corresponding to the period of thermic generation, amounts approximately to 0.5 dimensionless time units (for a 10^{-2} m thick layer of transformer oil, this period is on the order of 50 s).

REFERENCES

1. J. E. Hart, J. Fluid Mech. **47**, 547 (1971).
2. A. G. Kirdyashkin, A. I. Leont'ev, and N. V. Mukhina, Izv. Akad. Nauk SSSR, Mekh. Zhidk. Gaza, No. 5, 170 (1971).
3. G. Z. Gershuni, E. M. Zhukhovitskiĭ, L. E. Sorokin, and E. L. Tarunin, Izv. Akad. Nauk SSSR, Mekh. Zhidk. Gaza, No. 1, 94 (1974).
4. R. V. Birikh, G. Z. Gershuni, E. M. Zhukhovitskiĭ, and R. N. Rudakov, *Hydrodynamics* (Permsk. Gos. Univ., Perm, 1974), Vol. 5, pp. 139–148.
5. G. F. Shaidurov, Int. J. Heat Mass Transf. **2**, 280 (1961).
6. V. D. Zimin and V. G. Shaidurov, Izv. Akad. Nauk SSSR, Mekh. Zhidk. Gaza, No. 5, 188 (1975).
7. G. Z. Gershuni, E. M. Zhukhovitskiĭ, and E. L. Tarunin, Izv. Akad. Nauk SSSR, Mekh. Zhidk. Gaza, No. 5, 56 (1966).
8. K. H. Winters, J. Heat Transfer **109**, 894 (1987).
9. G. Z. Gershuni and E. M. Zhukhovitskiĭ, *Convective Stability of Incompressible Fluid* (Nauka, Moscow, 1970).
10. I. A. Ermolaev and A. I. Zhbanov, Inzh.-Fiz. Zh. **75** (5), 96 (2002).

Translated by P. Pozdeev

Technical Physics Letters, Vol. 29, No. 10, 2003, pp. 848–850. Translated from Pis'ma v Zhurnal Tekhnicheskoĭ Fiziki, Vol. 29, No. 20, 2003, pp. 26–32.

The Distribution of Creep Activation Energies in Oriented Polyethylene Films

V. I. Vettegren*, V. A. Marikhin, L. P. Myasnikova, E. M. Ivan'kova, and P. N. Yakushev

Ioffe Physicotechnical Institute, Russian Academy of Sciences, St. Petersburg, 194021 Russia
St. Petersburg State Technical University, St. Petersburg, 195251 Russia
** e-mail: Victor.Vettegren@mail.ioffe.ru*
Received May 15, 2003

Abstract—The "flow" creep in oriented polyethylene was studied using a Doppler velocity meter. The activation energy of the creep process was evaluated and it was established that there are three activation barriers for creep in the material studied. The most probable values, the scatter, and the relative concentration of these barriers in polyethylene samples were determined. © *2003 MAIK "Nauka/Interperiodica".*

As is known, the flow creep rate $\dot{\varepsilon}$ in solids depends on the temperature T and the mechanical stress σ as described by the formula [1–3]

$$\dot{\varepsilon} = \dot{\varepsilon}_0 \exp\left(-\frac{Q}{k_B T}\right), \quad (1)$$

where $\dot{\varepsilon}_0 = (10^{12}–10^{14})$ s^{-1}, Q is the stress-dependent creep activation energy, and k_B is the Boltzmann constant.

It was believed for a long time that the creep activation energy is constant for a given material. However, the results of high-precision measurements performed using a Doppler velocity meter for a series of unoriented amorphous polymers showed that the Q value increases with stress in the region of small deformations, then exhibits a decrease and remains virtually unchanged on further loading [4–7]. It was suggested that maximum activation barriers (physical knots) are encountered in the creep at small deformations, after which the barrier height ceases to change. Recently, the same unique experimental technique revealed a pronounced scatter of the flow creep rate in ultrahigh molecular weight polyethylene samples deformed in the dead load mode [8, 9].

We have studied the flow creep stage in polyethylene (PE) films of two types, prepared by gel technology (from solution) and by hot pressing (from melt). The films were oriented using the band drawing technique. The creep rate $\dot{\varepsilon}$ was measured with the aid of a Doppler velocity meter [4], one mirror of which was fixed on the moving clamp to monitor deformation of the sample. The $\dot{\varepsilon}$ value was determined using a deformation increment base of 0.3 μm (half-wavelength of the laser radiation employed). Figure 1a shows a fragment of the creep rate versus deformation curve for one of the PE samples studied.

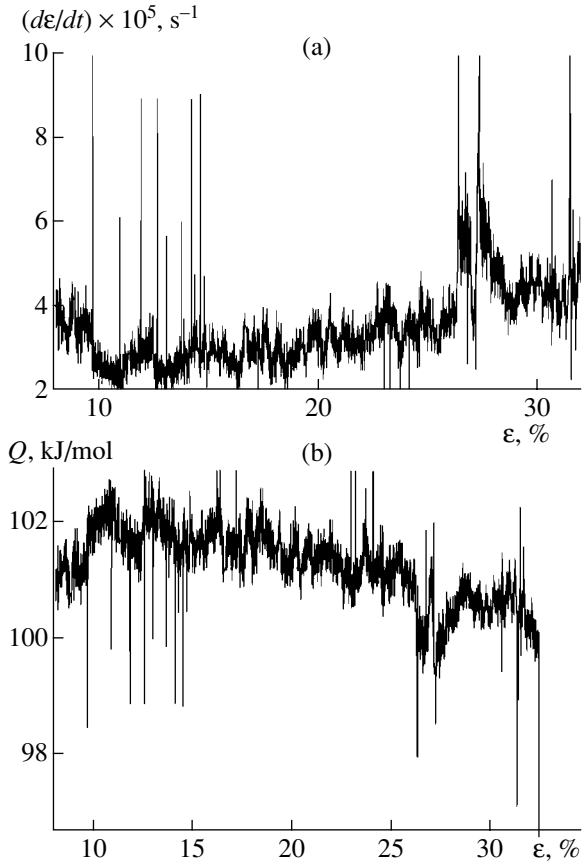

Fig. 1. Plots of the (a) creep rate and (b) activation energy versus deformation for PE films prepared by gel technology and oriented by drawing to $\lambda = 64$.

1063-7850/03/2910-0848$24.00 © 2003 MAIK "Nauka/Interperiodica"

We observed a scatter in the creep velocities described in terms of Eq. (1), which indicated that the activation energy

$$Q = k_B T \ln \frac{\dot{\varepsilon}_0}{\dot{\varepsilon}} \quad (2)$$

exhibits oscillations about a certain average value. This is illustrated in Fig. 1b showing a fragment of the Q versus $\dot{\varepsilon}$ curve calculated using Eq. (1). The scatter was relatively small: for a sample prepared by gel technology and oriented to a draw ratio of $\lambda = 64$, the creep activation energy was $Q = 96 \pm 5$ kJ/mol. Thus, the activation barrier height in this sample varies within 6% of the average value. In the other samples, the activation energy scatter also did not exceed 6% of the average Q value.

However, it was found that, even within this small scatter, not all values of the activation energy are equiprobable: the distribution density of the activation barrier heights exhibits clearly pronounced maxima (Fig. 2). This pattern indicates that there are most probable values of the activation energy. Thus, it was established that the distribution of the activation energies of creep in PE depends on the draw ratio and on the technology of unoriented film preparation (from solution or melt), that is, on the supermolecular structure of the polymer studied.

This conclusion does not contradict the previous results, from which it was concluded that the activation energy for creep in oriented polymers is independent of their supermolecular structure. Indeed, the width of the energy scatter interval (within 6% of the average value), in which the distribution depends on the polymer structure, falls within the limits of uncertainty of the traditional creep measurements (determining the average creep rate in the flow part of the creep curve, followed by calculating the activation energy as determined by formula (2)).

According to our data for a PE sample prepared by gel technology and then oriented by drawing to $\lambda = 120$, the activation barrier height distribution exhibits three narrow peaks possessing the Gaussian shapes (Fig. 2a). The analogous distribution for a PE sample obtained by hot pressing and drawn to $\lambda = 4.5$ shows two narrow peaks superimposed on a broad maximum (Fig. 2b); these peaks also correspond to the Gauss distribution. Finally, the distribution of the activation energies of creep in a PE sample prepared by gel technology and drawn to $\lambda = 64$ displays a single maximum (Fig. 2c). However, an analysis of the shape of this maximum showed that it represents a superposition of three overlapping peaks. Assuming these to have the Gaussian shapes, we performed deconvolution and determined the positions, halfwidths, and intensities of the components.

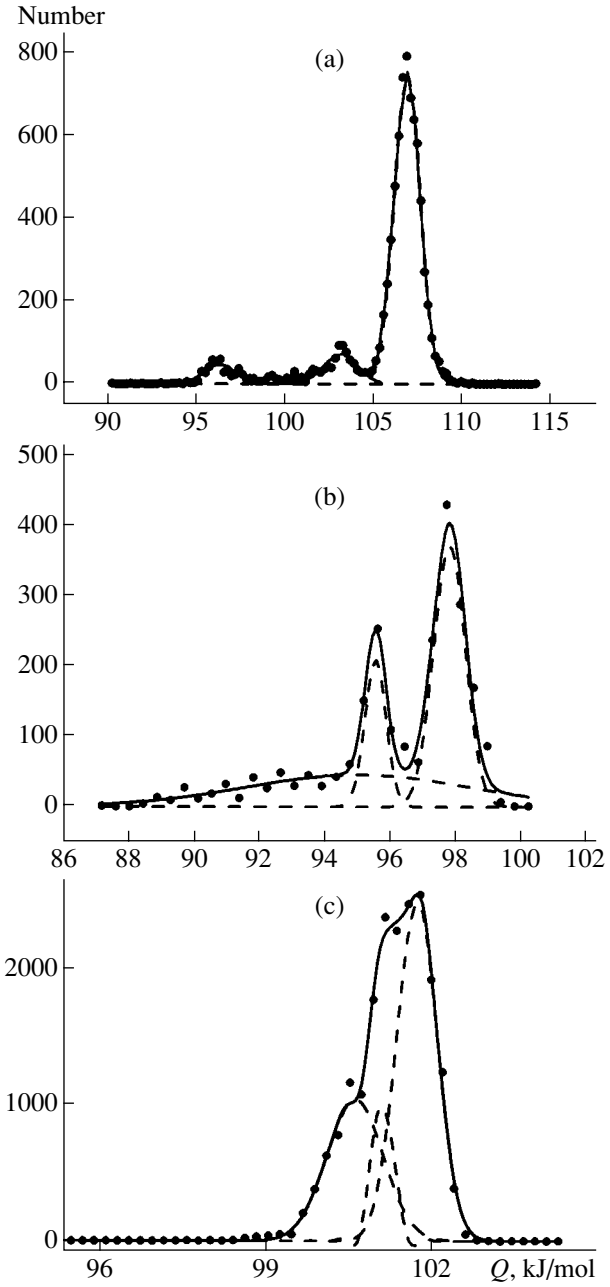

Fig. 2. Distributions of the activation energy of creep in PE film samples prepared by various methods: (a) gel technology ($\lambda = 64$); (b) gel technology ($\lambda = 120$); (c) hot pressing ($\lambda = 4.5$). Dashed curves show the results of approximation by Gaussian components, solid curves show the sum of components.

During our creep tests, the load was selected so as to provide that the creep rate would be approximately equal in the samples of three types mentioned above. However, the analysis of results showed that the average values of the creep rate are somewhat different (within 3%). Subsequently, the activation energies were

Most probable creep activation energies in oriented polyethylene films

Film technology and draw ratio (λ)	Activation barrier parameters			
	peak no.	peak position, kJ/mol	peak halfwidth, kJ/mol	relative intensity, %
Gel technology (λ = 64)	1	101.7	0.73	56
	2	101.1	0.34	12
	3	100.6	1.02	32
Gel technology (λ = 120)	1	100.5	1.46	83
	2	96.9	1.89	10
	3	90.5	1.79	7
Hot pressing (λ = 4.5)	1	97.8	0.97	45
	2	95.6	0.65	17
	3	95.0	6.83	38

corrected (multiplied or divided by the corresponding factor) for this difference. The corrected activation energies (at the distribution peaks) and their halfwidths and relative intensities are presented in the table. As can be seen from these data, the method of sample preparation (from melt or solution) and the draw ratio influence the peak energies, halfwidths, and relative intensities. Therefore, the PE film technology affects both the number of creep activation barriers and their relative heights and scatter around the average value.

In conclusion, high-precision measurements of the creep rate in oriented polyethylene film samples show that there are three most probable values of the activation energy of this process. Apparently, the existence of activation barriers of three different types is related to certain features in the fine structure of the polymer studied. This question will be considered in detail in the following paper.

Acknowledgments. The authors are grateful to N.N. Peschanskaya for fruitful discussion of results.

This study was supported in part by the Russian Foundation for Basic Research (project no. 03-05-64831) and by the Ministry of Education of the Russian Federation (project no. TO2-6.3-2706).

REFERENCES

1. V. R. Regel', A. I. Slutsker, and É. E. Tomashevskiĭ, *Kinetic Nature of the Hardness of Solids* (Nauka, Moscow, 1975).
2. A. S. Krauss and H. Eyring, *Deformation Kinetics* (Wiley, New York, 1975).
3. V. A. Petrov, A. Ya. Bashkarev, and V. I. Vettegren', *Physical Basis for the Prediction of Destruction of Constructional Materials* (Politekhnika, St. Petersburg, 1993).
4. V. A. Stepanov, N. N. Peschanskaya, and V. V. Shpeĭzman, *Strength and Relaxation Phenomena in Solids* (Nauka, Leningrad, 1984).
5. N. N. Peschanskaya, A. B. Sinani, and V. A. Stepanov, Vysokomol. Soedin., Ser. A **27**, 1513 (1985).
6. N. N. Peschanskaya and P. N. Yakushev, Fiz. Tverd. Tela (Leningrad) **30**, 2196 (1988) [Sov. Phys. Solid State **30**, 1264 (1988)].
7. N. N. Peschanskaya, Vysokomol. Soedin., Ser. A **31**, 1181 (1989).
8. N. N. Peschanskaya, Fiz. Tverd. Tela (St. Petersburg) **35**, 3019 (1993) [Phys. Solid State **35**, 1484 (1993)].
9. N. N. Peschanskaya, P. N. Yakushev, L. P. Myasnikova, *et al.*, Fiz. Tverd. Tela (St. Petersburg) **38**, 2582 (1996) [Phys. Solid State **38**, 1416 (1996)].

Translated by P. Pozdeev

Technical Physics Letters, Vol. 29, No. 10, 2003, pp. 851–852. Translated from Pis'ma v Zhurnal Tekhnicheskoĭ Fiziki, Vol. 29, No. 20, 2003, pp. 33–37.

InAs Based Multicomponent Solid Solutions for Thermophotovoltaic Converters

V. P. Khvostikov*, L. S. Lunin, V. V. Kuznetsov, V. I. Ratushny, É. V. Oliva, O. A. Khvostikova, and M. Z. Shvarts

Ioffe Physicotechnical Institute, Russian Academy of Sciences, St. Petersburg, 194021 Russia
Southern-Russia State Technical University, Novocherkassk, 346400 Russia
St. Petersburg State Electrotechnical University, St. Petersburg, 197376 Russia
** e-mail: vlkhv@scell.ioffe.rssi.ru*
Received May 12, 2003

Abstract—Photoelectric converters based on InAsSbP and GaInAsSbP solid solutions were obtained by liquid phase epitaxy. The new devices are promising elements for thermophotovoltaic generators operating at a reduced emitter temperature (~1000°C). © *2003 MAIK "Nauka/Interperiodica".*

In recent years, photoelectric converters based on narrow-bandgap (0.5–0.6 eV) solid solutions of the GaInAsSb system with GaSb and AlGaAsSb epitaxial layers (wide-bandgap windows) were developed for thermophotovoltaic (TPV) generators operating at a reduced emitter temperature (1000–1200°C) [1, 2]. The efficiency of these photoelectric elements can be improved by using solid solutions with compositions modified so as to increase the sensitivity in the long-wavelength spectral range [3]. However, such a modification of GaInAsSb solid solution is difficult, because this system features an extended immiscibility region hindering the obtaining of epitaxial layers with E_g below 0.5 eV. Promising materials for the active region of photoconverters operating at an emitter temperature about 1000°C or even below are offered by solid solutions of the InAsSbP and GaInAsSbP systems possessing lattice parameters coinciding with that of InAs [4, 5].

In a quaternary solid solution of the $InAs_{1-x-y}Sb_yP_x$ type, the bandgap width and the spin–orbit splitting energy are close in a broad range of compositions [6]. This feature is known to increase the efficiency of nonradiative recombination via the Auger process. Introducing Ga into the four-component solid solution changes the spin–orbit splitting energy and, hence, decreases the probability of Auger recombination, the main process limiting the characteristics of photoelectric conversion [7]. In addition, the results of calculations show that GaInAsSbP solid solutions with small Ga content (<10 at. %) provide for the matching of both lattice parameters and thermal expansion coefficients at the heteroboundary. This decreases the formation of dislocations negatively influencing the working properties of photoelements.

This study was aimed at the synthesis and characterization of InAsSbP and GaInAsSbP solid solutions isoperiodic with InAs, suitable for TPV conversion applications. For the obtaining of photoconverters effectively operating in the range of wavelengths above 2.2 μm, it is necessary to form InAsSbP layers with a bandgap width of 0.45–0.48 eV, which corresponds to phosphorus content in the solid solution on a level of 0.25–0.3 mol %.

Optimum technological parameters of the process of liquid phase heteroepitaxy of InAsSbP and GaInAsSbP solid solutions isoperiodic with InAs were determined based on an analysis of the liquid–solid equilibrium phase diagrams within the framework of a simple solution model. The method of analysis and the main parameters of calculations are presented in monograph [8]. Using justified values of the excess model energies of mixing, we successfully calculated the temperatures and compositions of both liquidus and solidus in the region of temperatures (T ~ 853 K) for the epitaxy of compositions isoperiodic with InAs on both sides of the binodal space.

The epitaxial growth was performed under isothermal conditions, by step cooling at a temperature of T = 843 K. The initial charge compositions were selected such that the liquid phase at the epitaxial growth temperature would be supercooled by 11–17 K relative to the liquidus temperature.

The layers of five-component solid solutions of the $Ga_xIn_{1-x}As_{1-x-y}P_ySb_z$ system lattice-matched with InAs were obtained in the region of compositions corresponding to y = 0.22–0.29 and x = 0.03–0.08. Under the isoperiodic substitution conditions, an increase in the content of gallium in the solid phase led to a decrease in the content of phosphorus, while the bandgap width of the five-component solid solution practically remained unchanged. The above range of compositions provides for the bandgap width required for the effective TPV conversion.

1063-7850/03/2910-0851$24.00

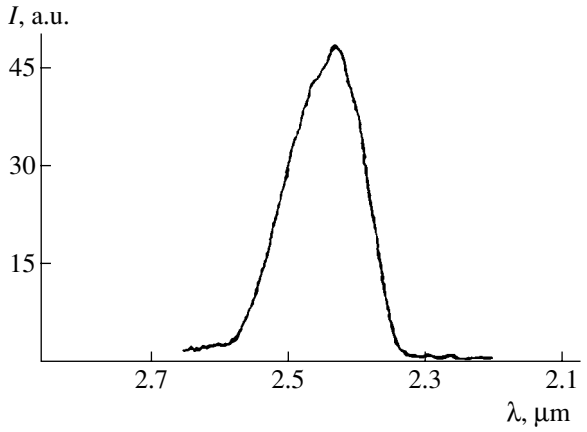

Fig. 1. The PL spectrum of a five-component solid solution $Ga_{0.08}In_{0.92}As_{0.58}Sb_{0.16}P_{0.26}$/InAs(100) at $T = 77$ K.

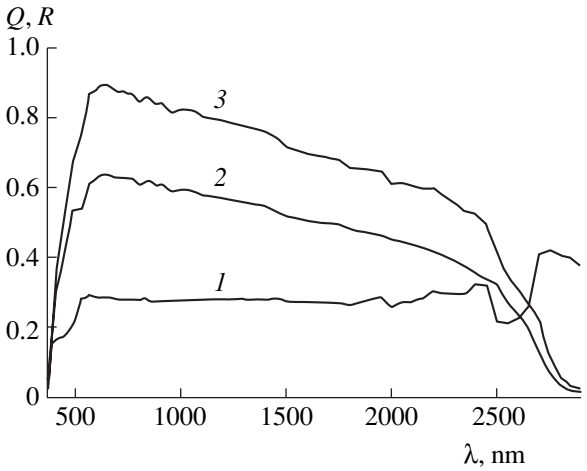

Fig. 2. The spectral characteristic of an InAsSbP/InAs heterostructure: (*1*) reflectance; (*2*) external quantum yield; (*3*) internal quantum yield.

The photoluminescence (PL) spectra of InAsSbP and GaInAsSbP solid solutions were measured at $T = 77$ K using samples cooled with liquid nitrogen. Figure 1 shows the typical PL spectrum of the epitaxial layer of a five-component solid solution isoperiodic with InAs, exhibiting emission within the wavelength interval from 2.4 to 2.7 μm. It should be noted that the intensity of emission from samples of the five-component solid solutions studied was several times that for the epitaxial layers of InAsSbP with close values of the bandgap.

The results of experiments on the growth and characterization of InAsSbP/InAs(100) heterostructures allowed us to begin with the development of high-efficiency TPV converters operating in the middle infrared wavelength range. The *p*-type conductivity region was created by method of zinc diffusion from the gas phase in a quasiclosed volume. Generated in the subsurface layer of InAsSbP, the built-in electric field of the diffusant ions draws the photoproduced charge carriers into the semiconductor bulk, thus providing a high quantum yield in the shortwave range.

Figure 2 shows the spectral characteristic of a heterostructure of the *p*-InAsSbP/*n*-InAsSbP/*n*-InAs type. The internal quantum yield with allowance of reflection losses (curve *1*) in the wavelength range from 550 to 2500 nm amounts to 50–90%. The measured values of spectral sensitivity are indicative of a high crystallographic quality of the active region of this heterostructure.

The photosensitivity of these heterostructures in the longwave range can be increased by optimizing the depth of zinc diffusion and the thickness of the InAsSbP solid solution layer and by improving the quality of heteroboundaries. Additional promising ways to increase the longwave photosensitivity are the growth of wide-bandgap layers of the rear potential barrier and the wide-bandgap window (e.g., of AlGaAsSb), as well as the use of GaInAsSbP (isoperiodic with InAs) as the active layer of a TPV converter.

To summarize, we obtained for the first time the epitaxial layers of five-component solid solutions of the $Ga_xIn_{1-x}As_{1-x-y}P_ySb_z$ system ($y = 0.22$–0.29 and $x = 0.03$–0.08) with a low gallium content (<10%). Lattice-matched with InAs, these materials have good prospects for use in optoelectronic devices.

In addition, we studied the spectral characteristics of InAsSbP/InAs heterostructures with a longwave photosensitivity threshold at 2.7 μm and an internal quantum yield of 50–90% in the wavelength range from 500 to 2500 nm.

REFERENCES

1. V. M. Andreev, V. P. Khvostikov, V. R. Larionov, *et al.*, in *Proceedings of the 26th IEEE Photovoltaics Community Conference, Anaheim, 1997*, pp. 935–939.
2. C. W. Hitchcock, R. J. Gutmann, H. Ehsani, *et al.*, J. Cryst. Growth **195**, 363 (1998).
3. M. G. Mauk, Z. A. Shellenbarger, J. A. Cox, *et al.*, J. Cryst. Growth **211**, 189 (2000).
4. T. I. Voronina, T. S. Lagunova, K. D. Moiseev, *et al.*, Fiz. Tekh. Poluprovodn. (St. Petersburg) **33**, 781 (1999) [Semiconductors **33**, 719 (1999)].
5. N. A. Charykov, A. M. Litvak, M. P. Mikhaĭlova, and Yu. P. Yakovlev, Fiz. Tekh. Poluprovodn. (St. Petersburg) **31**, 410 (1997) [Semiconductors **31**, 344 (1997)].
6. H. Mani, E. Tournie, J. L. Lazzari, *et al.*, J. Cryst. Growth **121**, 463 (1992).
7. S. J. Fonash, *Solar Cell Device Physics* (Academic, New York, 1981), p. 53.
8. V. V. Kuznetsov, P. P. Moskvin, and V. S. Sorokin, *Nonequilibrium Liquid-Phase Heteroepitaxy of Semiconductor Solid Solutions* (Metallurgiya, Moscow, 1991).

Translated by P. Pozdeev

Technical Physics Letters, Vol. 29, No. 10, 2003, pp. 853–854. Translated from Pis'ma v Zhurnal Tekhnicheskoĭ Fiziki, Vol. 29, No. 20, 2003, pp. 38–42.

Rotation of the Magnetization Vector of a Monodomain Particle under the Action of a High-Frequency Field Pulse

L. N. Kotov* and L. S. Nosov

Syktyvkar State University, Syktyvkar, Komi Republic, Russia

** e-mail: kotov@syktsu.ru*

Received May 6, 2003

Abstract—We obtained a numerical solution of the modified Hilbert equation describing rotation of the magnetization vector in a high-frequency field of large amplitude. Based on this solution, we have studied rotation of the magnetization vector of a spherical ferromagnetic monodomain particle, possessing a cubic anisotropy, from the direction parallel to an easy magnetization axis to the perpendicular direction under the action of a high-frequency magnetic field pulse. The amplitudes and the interval of frequencies of the magnetic field capable of rotating the particle magnetization vector are determined. *© 2003 MAIK "Nauka/Interperiodica".*

An alternative energy-dependent information carrier is offered by an ensemble of independent, oriented ferromagnetic monodomain particles [1, 2]. The method of reading information from such a carrier is based on excitation of the ensemble with a low-power alternating magnetic field at a ferromagnetic resonance frequency [1]. The readout process consists in scanning over a certain frequency range: the presence of a response at some frequency corresponds to logical 1, while the absence of such response corresponds to logical 0. Recording data with the aid of a high-frequency field consists in rotating the magnetization vector of a particle from the direction parallel to the easy axis to a perpendicular direction.

For the sake of simplicity, the particles are considered as independent and possessing a spherical shape. Let us consider one particle and represent its magnetic energy density as a sum of the energy density of the cubic anisotropy and the Zeeman energy density for the particle magnetic moment in an alternating magnetic field [3]:

$$\begin{aligned} U(\mathbf{m}) &= K_1(m_x^2m_y^2 + m_y^2m_z^2 + m_x^2m_z^2) \\ &+ K_2m_x^2m_y^2m_z^2 - \mathbf{M}\cdot\mathbf{h}\cdot\sin(\omega t). \end{aligned} \quad (1)$$

Here, $K_1 > 0$ and $K_2 < 0$ are the first and second constants of the cubic anisotropy, respectively; $\mathbf{h}\cdot\sin(\omega t)$ is the external alternating magnetic field with a frequency ω; $\mathbf{m} = \mathbf{M}/|\mathbf{M}|$ is the vector of direction cosines of the particle magnetization vector $\mathbf{M}$. The coordinate axes *Ox*, *Oy*, and *Oz* are assumed to correspond to the principal crystallographic axes [100], [010], and [001], respectively. In the absence of external fields, the magnetic moment occurs in one of the three stable positions with minimum energies, being parallel to one of the three easy axes.

An equation of the Hilbert type describing the motion of the particle magnetization vector can be written, after some transformations, in the following form [3]:

$$\frac{d\mathbf{m}}{dt^*} = -[\mathbf{m}\times\mathbf{H}_{\text{eff}}^*] + \alpha\left[\mathbf{m}\times\frac{d\mathbf{m}}{dt^*}\right], \quad (2)$$

where α is the dimensionless damping parameter, $\mathbf{H}_{\text{eff}}^* = -\delta U^*/\delta\mathbf{m}$ is the reduced effective magnetic field acting upon the magnetic moment, $U^*(\mathbf{m}) = U(\mathbf{m})|\mathbf{M}|/2K_1$ is the reduced free energy density, $t^* = t2\gamma K_1/|\mathbf{M}|$ is the reduced time, $\omega^* = \omega|\mathbf{M}|/2\gamma K_1$ is the reduced frequency, $\mathbf{h}^* = \mathbf{h}|\mathbf{M}|/2K_1$ is the reduced alternating magnetic field amplitude, and γ is the gyromagnetic ratio. In the spherical coordinate system, Eq. (2) is written as

$$\begin{cases} \dfrac{d\theta}{dt^*} = -\dfrac{1}{\sin\theta(\alpha^2+1)}\dfrac{\partial U^*}{\partial\varphi} - \dfrac{\alpha}{\alpha^2+1}\dfrac{\partial U^*}{\partial\theta}, \\ \dfrac{d\varphi}{dt^*} = \dfrac{1}{\sin\theta(\alpha^2+1)}\dfrac{\partial U^*}{\partial\theta} - \dfrac{\alpha}{\sin^2\theta(\alpha^2+1)}\dfrac{\partial U^*}{\partial\varphi}, \end{cases} \quad (3)$$

where θ and φ are the polar and azimuthal angles (the polar and azimuthal axes coincide with the *Oz* and *Ox* axes, respectively, of the above Cartesian system).

Let the initial magnetization vector direction be parallel to the *Oy* axis and the alternating field be applied parallel to the *Ox* axis. A solution to Eqs. (3), obtained by the Runge–Kutta method of the 4–5th order is illustrated in Fig. 1. As the amplitude of the alternating magnetic field increases, the oscillating magnetization vector deviates from the equilibrium direction, passes through an unstable equilibrium state, and acquires another stable orientation perpendicular to the initial direction. This phenomenon exhibits a resonance character: the magnetization vector rotation is observed in a certain interval of reduced frequencies $\Delta\omega^*$ called

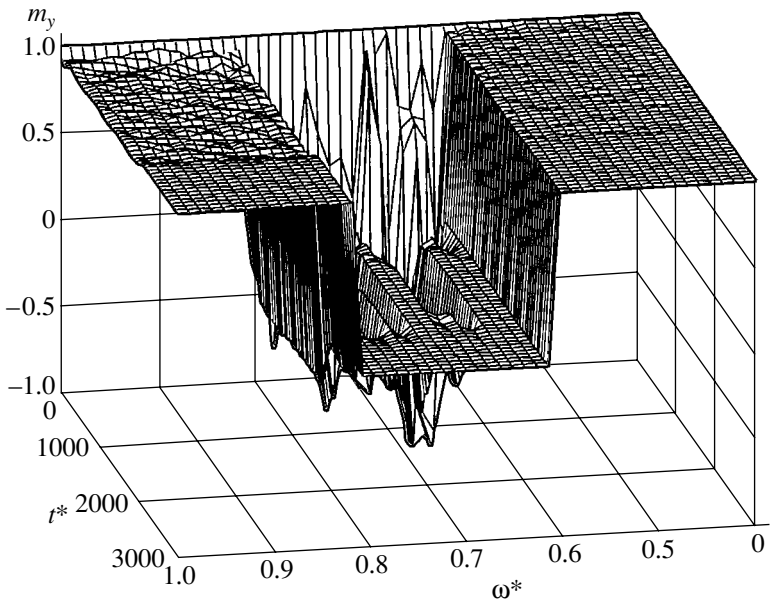

Fig. 1. The envelope surface of m_y as a function of reduced time t^* and frequency ω^* for $\alpha = 0.01$, $h^* = 0.09$, and the magnetic field pulse duration $\tau = 20/\alpha = 2 \times 10^3$ (observation time $\Delta t^* = 1.5\tau = 3 \times 10^3$).

reorientation band. The reorientation band is determined by the modulus of the reduced magnetic field amplitude h^* and the dimensionless damping parameter α. We can also introduce the reorientation threshold, representing a minimum value of h^* (at a fixed field frequency) for which the magnetization vector rotation takes place.

In all cases, the resonance rotation of the magnetization vector for a minimum reorientation threshold $h^*_{\min}$ takes place at a frequency below the reduced frequency of the ferromagnetic resonance $\omega^*_{res} = 1/\sqrt{1+\alpha^2}$. When the threshold h^* grows, the reorientation band width increases. As the damping parameter α decreases at a fixed field amplitude, the reorientation band exhibits narrowing and shifts toward higher frequencies (Fig. 2). For a very large magnetic field amplitude ($h^* \gg h^*_{\min}$), the particle magnetization vector exhibits a chaotic behavior. Under the action of the external magnetic field, this vector exhibits reorientation both in the perpendicular direction and in the directions parallel and antiparallel to the initial magnetization.

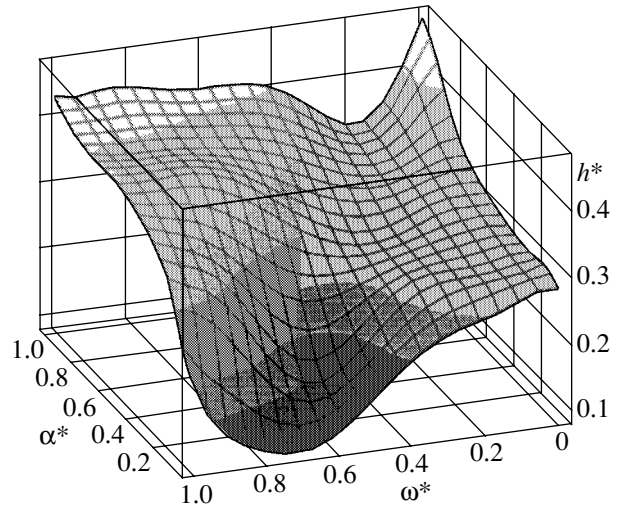

Fig. 2. The surface of reorientation threshold h^* as a function of the reduced frequency ω^* and damping parameter α for $K_2/K_1 \approx -0.16$.

Thus, based on the numerical solution of the modified Hilbert equation, we determined the conditions of rotation of the magnetization vector of a ferromagnetic monodomain particle from the direction parallel to an easy magnetization axis to the perpendicular direction under the action of a high-frequency magnetic field pulse. The results can be used for data recording in a medium representing an ensemble of independent ferromagnetic monodomain particles, the readout being effected through excitation of this ensemble by a weak alternating magnetic field [1, 2].

REFERENCES

1. L. N. Kotov, Fanur F. Asadullin, Farit F. Asadullin, in *Proceedings of the International Forum on Wave Electronics and Its Applications, St. Petersburg, 2000,* pp. 414–416.
2. L. N. Kotov and L. S. Nosov, in *Proceedings of the XVIII International School-Seminar "New Magnetic Materials of Microelectronics," Moscow, 2002* (Mosk. Gos. Univ., Moscow, 2002), pp. 734–736.
3. A. G. Gurevich, *Magnetic Resonance in Ferrites and Antiferromagnets* (Nauka, Moscow, 1973).

Translated by P. Pozdeev

Technical Physics Letters, Vol. 29, No. 10, 2003, pp. 855–857. Translated from Pis'ma v Zhurnal Tekhnicheskoĭ Fiziki, Vol. 29, No. 20, 2003, pp. 43–48.

Rigid Rotations of a Plate and the Related Speckle Displacements in the Image Plane

A. P. Vladimirov* and D. O. Popov

Institute of Engineering Science, Ural Division, Russian Academy of Sciences, Yekaterinburg, Russia

** e-mail: vap@imach.uran.ru*

Received May 13, 2003

Abstract—We describe an optical setup created for the verification of theoretical results concerning the displacement of speckles in the plane imaging a surface, which performs rotational motion. On the whole, the experimental results are consistent with the theory: there is a linear relationship between the surface rotation and the speckle displacement. The sensitivity of this method is proportional to the distance from a lens to the observation plane. *© 2003 MAIK "Nauka/Interperiodica".*

Introduction. Researchers dealing with lasers give attention to the phenomenon whereby speckles shift and change in response to the displacements, deformations, and rotations of a rough surface. These effects were summarized and generalized by Yamaguchi [1], who theoretically studied the relations between small displacements, rotations, and deformations of a surface and the speckle dynamics. Within the framework of a more general problem, these effects were studied in [2].

Using a three-dimensional diffuser model justified in [3], a relation was established between translations, deformations, and rotations of elements of a thin three-dimensional object and the displacements of speckles in the image plane. The component A_y of the vector of speckle displacement in the vicinity of some observation point is given by the formula [2]

$$A_y(\mathbf{u}_0, \Omega, \varepsilon) = mu_{y0} + \frac{Z}{L_0'}\Big\{(mu_{y0} - u_{y0}) + L_0\Big[(\varepsilon_{xy} - \Omega_z)\cdot \mathbf{l}_{sx} + \varepsilon_{yy}\mathbf{l}_{sy} + (\varepsilon_{yz} + \Omega_x) \times (\mathbf{l}_{sz} + 1) + \frac{1}{L_s}u_{x0}\mathbf{l}_{sx}\mathbf{l}_{sy} + \frac{1}{L_s}u_{y0}(\mathbf{l}_{sy}^2 - 1) + \frac{1}{L_s}u_{z0}(\mathbf{l}_{sy}\mathbf{l}_{sz})\Big]\Big\}, \quad (1)$$

where m is the lens magnification; $\mathbf{l}_{sx}$, $\mathbf{l}_{sy}$, $\mathbf{l}_{sz}$ are the components of a unit vector directed from the object to the radiation source; Z is the distance from the image plane to the observation plane; L_0' is the distance from the lens to the image plane; L_0 is the distance from the object to the lens; L_s is the distance from the radiation source to the object; u_{x0}, u_{y0}, u_{z0} are the components of the translation vector; ε_{xy}, ε_{yy}, ε_{yz} are the components of the deformation tensor; and Ω_z, Ω_x are the components of the rigid rotation tensor averaged over a region of the lens resolution.

For an undeformed flat object performing no translations, illuminated with a parallel light beam incident along the normal, formula (1) with $m = 1$ yields the relation

$$A_y = 2Z\omega_x, \quad (2)$$

where $\omega_x = \dfrac{\partial u_z}{\partial y}$ is the angle of rotation around the *0x* axis (expressed in radians). This study was aimed at experimental verification of this relationship.

Experiment. Figure 1 shows an optical scheme of the experimental setup. The distance from object *5* to lens *9* was equal to $L_0 = 168$ mm (two focal lengths of the lens). The angle between illumination and observation directions was 10°. The diameter of diaphragm *10* was 2.1 mm. The films of speckle dynamics in response to 5-s plate rotations were recorded into the memory of computer *13* for various distances L from lens *9* to TV camera *12* under otherwise identical experimental conditions. The rotation rate was $(1.52 \pm 0.04) \times 10^{-3}$ rad/s. The records were made with a monochrome camera of the STA-572 type. The radiation source was a He–Ne laser of the LGN-207F type operating at a power of 1.6 mW. The signal from the camera was fed into the computer via a videocard of the Miro Video DC30 type.

An analysis of the recorded films showed the following. There is a certain position of the camera (L = 182 mm) for which the speckles exhibit no displacement, but the pattern of speckles is subject to gradual variation. Should the camera move closer or farther from this special position, the speckles exhibit a shift, the displacement increasing with the distance from the camera to said position.

These effects were analyzed and the speckle displacements were determined by processing digitized

1063-7850/03/2910-0855$24.00

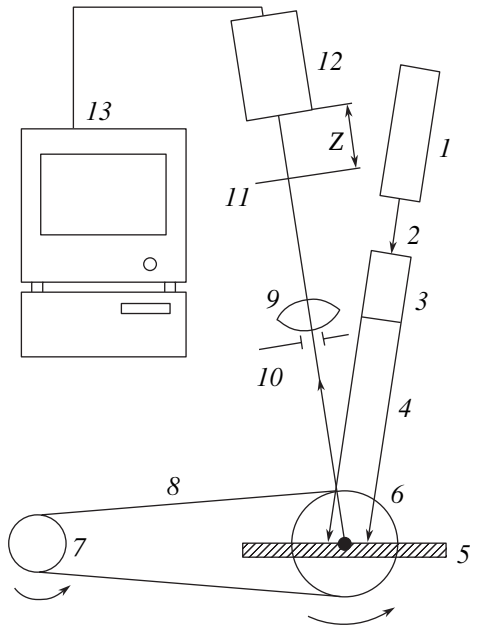

Fig. 1. An optical scheme of the experimental setup: (*1*) laser; (*2*) laser beam; (*3*) collimator; (*4*) illuminating beam; (*5*) duralumin plate; (*6*) rotating platform; (*7*) driving shaft; (*8*) belt drive; (*9*) lens; (*10*) diaphragm; (*11*) image plane; (*12*) TV camera; (*13*) computer.

records using a computer routine analogous to that described in [4]. This software allowed the operator to select an arbitrary line on the display and specify a desired frame frequency for the digital processing. The video signals were digitized along the line and the sequentially requested images were ordered top to bottom. Thus, a two-dimensional pattern was obtained in which the speckle response was visualized as varying in space (along the line) and time. When the speckles did not shift, the pattern displayed vertical lines, while displaced speckles were imaged by oblique lines.

The speckle displacements were determined as shifts of the peak of the function

$$B(m) = \frac{2}{K}\sum_{k=1}^{k/2}[I_1(k)-\bar{I}_1][I_2(k+m)-\bar{I}_2],$$

where $I_1 = I_1(n)$ and $I_2 = I_2(n)$ are the video signal intensities at two moments of time on the line selected, K is the number of pixels in the line, and top bar indicates signals averaged over the line. Figure 2 shows the typical plots of the speckle shift A_y versus plate rotation angle for various distances L from lens to camera. Figure 3 presents a plot of the speckle displacement per unit rotation angle (radian) versus lens to camera distance L constructed by the experimental data.

Discussion of results. On the whole, the experimental results are consistent with the theory. There is a special position of the observation plane at which the speckles exhibit no displacement. When the camera is moved closer or farther from this special position, the speckles exhibit a shift. The displacement of speckles is linearly dependent on the rotation angle. Also in agreement with the theory, the displacement per unit rotation angle is a linear function of the distance from the lens to the observation plane. However, the slope of this dependence (1.54 ± 0.03) differs from the theoretical value (2.0). The position of the observation plane corresponding to zero displacement also deviates by 21 mm from that predicted by the theory.

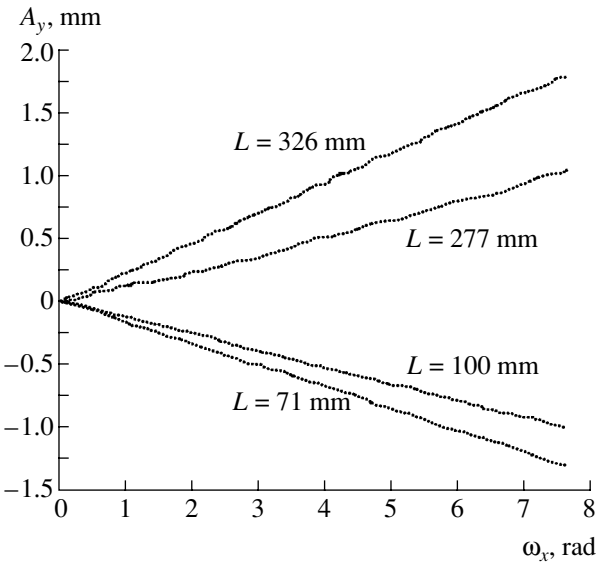

Fig. 2. The typical plots of speckle shift A_y versus plate rotation angle ω_x for various distances L from lens to camera.

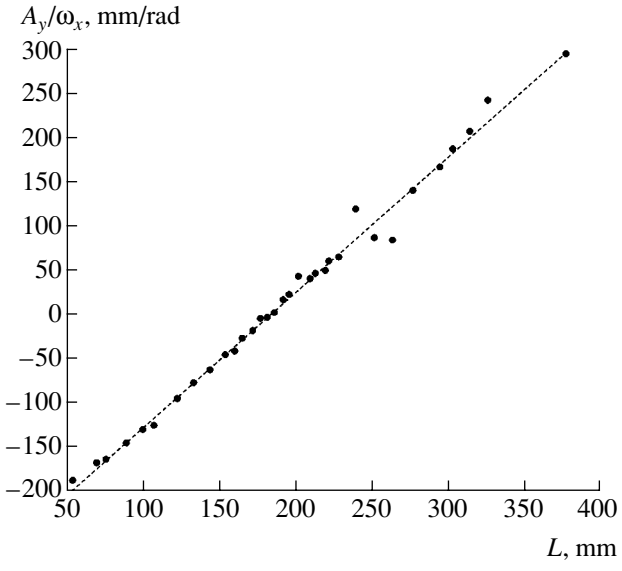

Fig. 3. A plot of the speckle displacement per unit rotation angle versus distance L from the lens to the observation plane.

The discrepancies are probably related to the fact that diaphragm *10* (Fig. 1) was spaced by 12.3 mm from the middle plane of the lens, which was not taken into account in the theoretical description. In addition, the positions of the object plane and the image plane at a magnification of $m = 1$ were visually determined in the absence of the diaphragm. With a small diaphragm, these positions may change. The plot in Fig. 3 shows two points significantly deviating from the linear relationship in the region of L between 240 and 264. The reasons for such scatter are unclear. There are probably some drawbacks in the experimental technique. This makes necessary new and more precise measurements.

Conclusions. Based on the results obtained using the experimental setup described above, we arrive at the following conclusions.

(i) For the directions of illumination and observation of an object close to the normal to the rotating sample surface, there exists an observation plane for which the speckles exhibit no displacement in the image plane.

(ii) When the observation plane is shifted along the optical axis from the above special position, the speckles exhibit displacement, the sign of which depends on the direction of shift of the observation plane.

(iii) The displacement of speckles is proportional to the rigid rotation angle.

(iv) The displacement of speckles per unit rotation angle is a linear function of the shift of the observation plane.

The above results generally agree with the theory. However, the position of the observation plane corresponding to the zero displacement of speckles and the sensitivity of the method differ from theoretically predicted values.

REFERENCES

1. I. Yamaguchi, Opt. Acta **28**, 1359 (1991).
2. A. P. Vladimirov, Doctoral Dissertation (Ekaterinburg, 2002).
3. A. P. Vladimirov, Zh. Tekh. Fiz. **68** (12), 59 (1998) [Tech. Phys. **43**, 1454 (1998)].
4. A. P. Vladimirov and E. N. Galkin, Proc. SPIE **4705**, 173 (2002).

Translated by P. Pozdeev

Technical Physics Letters, Vol. 29, No. 10, 2003, pp. 858–861. Translated from Pis'ma v Zhurnal Tekhnicheskoĭ Fiziki, Vol. 29, No. 20, 2003, pp. 49–57.

Optical Properties of Hydrogenated Amorphous Carbon Films Deposited from Glow Discharge Plasma

S. G. Yastrebov[a,*], T. Allen[b], V. I. Ivanov-Omskii[a], V. Chan[b], and S. Zukotynski[c]

[a] *Ioffe Physicotechnical Institute, Russian Academy of Sciences, St. Petersburg, Russia*
** e-mail: yastrebov@mail.ioffe.ru*
[b] *University of Tennessee at Chattanooga, 37403 Chattanooga, Tennessee, USA*
[c] *Department of Electrical and Computer Engineering, University of Toronto, Canada*

Received April 7, 2003

Abstract—Optical transmission and reflection spectra of the layers of hydrogenated amorphous carbon deposited onto fused quartz substrates from a glow discharge plasma are studied on samples of two series, which differ by the substrate temperatures (200 vs. 400°C) during deposition. The dispersion of the imaginary part of the dielectric function and the spectrum of the effective electron density of states involved in optical transitions are reconstructed. It is shown that this spectrum is adequately described by a sum of two Gaussian contours. The maximum of the first contour falls in the range of low frequencies and reflects the contribution of π electrons to the optical absorption of the material, while the second contour with the maximum in the high-frequency region is assigned to the contribution of σ electrons. © *2003 MAIK "Nauka/Interperiodica".*

1. Introduction

The layers of hydrogenated amorphous carbon (a-C:H), sometimes called diamondlike carbon, grown at different conditions may possess considerably different properties. Using methods of nondestructive testing, it is possible to assess the potential of such layers for application in one or another practical field and to modify their properties by making the necessary changes in the deposition process. Optical spectroscopy undoubtedly is among these methods, since the optical transparence is a very important characteristic of materials used, for example, for coating laser disks. Using this method, one can experimentally determine the parameters for quantitative characterization of the material produced by the given technology.

In this paper, we present the reflection and transmission spectra of a-C:H grown by a modified method of the glow discharge plasma deposition in the atmosphere of pure methane. Both the optical reflection and transmission spectra are analyzed. It is shown that the reflection spectra allow the number of the interference peaks to be determined, while the ratio between the reflection and transmission coefficients contains information on the refractive index. In addition, the transmission spectra allow one to extract information on the effective density of states created by π and σ electrons.

2. Experimental

2.1. Samples and experimental techniques. The layers of amorphous carbon were grown by a modified method of the glow discharge plasma deposition in the atmosphere of pure methane (the saddle-field glow discharge deposition method) [1]. The films were deposited onto fused quartz substrates. The substrate holder was grounded. The growth occurred at a pressure of 50 mTorr, the gas flow rate was 2.5 cm^3/s, and the discharge current was 40 mA. The substrate temperate was 200 and 400°C for samples no. 200 and no. 400, respectively. Dependences of the transmission (T) and reflection (R) coefficients on the wavelength λ were measured using a Perkin-Elmer Lambda 18 spectrophotometer in the wavelength region from 185 to 900 nm. Data on the optical properties of this material were previously reported in [2].

Figure 1 shows the transmission and reflection spectra for the two types of amorphous carbon samples and for the substrate. It is seen that the substrate makes no considerable contribution to the transmittance. The reflection spectra exhibit interference profiles. The inset in Fig. 1 shows the maxima of the reflection coefficient versus the reciprocal wavelength for both samples. It should be noted that the experimental points are in good agreement with the linear dependence extrapolated to an infinitely large wavelength.

2.2. Calculation of the film thickness and refractive index. The phase shift φ for the maximum with the number $(1 + 2\mu)$ observed in the dependence of the reflectance on the wavelength λ is [4]

$$\varphi = \pi(1 + 2\mu). \quad (1)$$

On the other hand, it is known that

$$\varphi = \frac{4\pi nd}{\lambda_{max}}, \quad d = \frac{\varphi\lambda_{max}}{4\pi n}, \tag{2}$$

where d is the film thickness, n is the refractive index, and λ_{max} is the wavelength at which the reflectance reaches its maximum.

The refractive index of the film was calculated using an equation that can be derived by neglecting absorption in the relation between the energy reflection and transmission coefficients of the air–film–substrate system [3–5]:

$$n^2 - 2(n_s R_{tm})^{1/2} n - n_s = 0. \tag{3}$$

Here, R_{tm} is the value of the function $R(\lambda_{max})/T(\lambda_{max})$ at the wavelength λ_{max} and n_s is the refractive index of the substrate. For the case displayed in Fig. 1, λ_{max} = 517 and 564 nm for samples no. 200 and no. 400, respectively. To find the refractive index, it is necessary to know the refractive index n_s of the substrate, which can be easily determined using an equation for the substrate transmittance T (Fig. 1) at the wavelength λ_{max} [3, 2],

$$Tn_s^2 + 2n_s(T-2) + T = 0. \tag{4}$$

From the two roots of this equation, 0.682 and 1.465, we choose the solution 1.465. Substituting the root of Eq. (4) and the values of $R(\lambda_{max})$ and $T(\lambda_{max})$ from Fig. 1 in to relation (3), we obtain the refractive indices of about 1.7 for both samples.

The number $(1 + 2\mu)$ of the reflection coefficient maximum was determined by plotting $(1 + 2\mu)$ versus the reciprocal wavelength. The results are shown in the inset in Fig. 1. As the initial point, we took the number of the reflectance interference maximum $(1 + 2\mu) = 1$ at the infinitely large wavelength [4]. A good agreement of the experimental points with the linear dependence confirms the correct choice of the numbers of the interference peaks. The first maximum experimentally observed for each sample is marked by an arrow in Fig. 1. It is seen that its number is 3. Substituting this number and the refractive index in to (2), we obtain the film thicknesses of 228 and 250 nm for samples no. 200 and no. 400, respectively.

2.3. Calculation of the extinction coefficients and the imaginary part of the dielectric function. The extinction coefficient k was calculated using the expression for the transmittance [5]

$$T(\lambda) = AX, \tag{5}$$

where $X = \exp\left(\frac{4\pi dk}{\lambda}\right)$ is the Bouguer term, $T(\lambda)$ is the experimental dependence of the transmittance on the wavelength (Fig. 1), and A is a preexponential factor, which we assumed to be constant because of a suppressed interference pattern observed for the transmission spectra (Fig. 1). Taking this constant into account

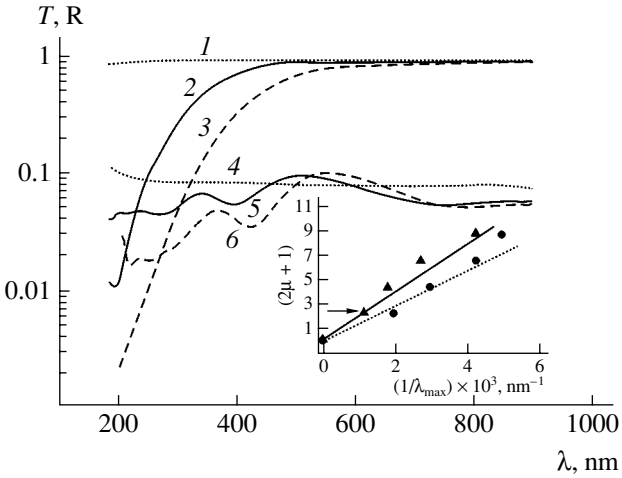

Fig. 1. (*1*) Transmission and (*4*) reflection spectra of the substrate, transmission spectra of the samples (*2*) no. 400 and (*3*) no. 200, and reflection spectra of the samples (*5*) no. 400 and (*6*) no. 200. The inset shows the plot of the number $(1 + 2\mu)$, corresponding to the interference maxima in the reflection spectra, versus the reciprocal wavelength.

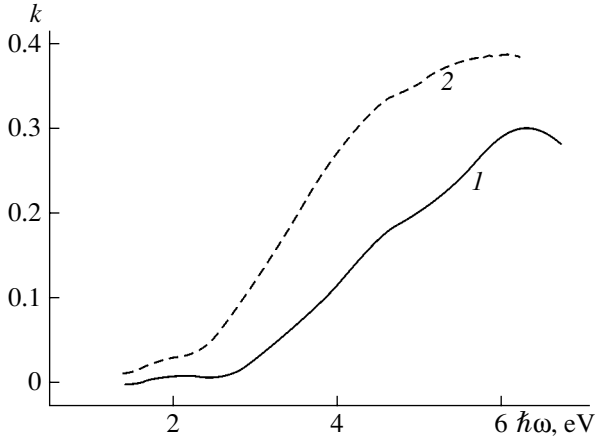

Fig. 2. Dependence of the extinction coefficients of samples (*1*) no. 200 and (*2*) no. 400 on the photon energy.

by the normalization of the transmission spectra to their maxima, we obtained a simple expression for the wavelength dependence of the extinction coefficient:

$$\frac{T(\lambda)}{A} = X, \quad k = -\ln\left(\frac{T(\lambda)}{A}\right)\frac{\lambda}{4\pi d}. \tag{6}$$

Figure 2 presents the dependence of the extinction coefficient on the photon energy $\hbar\omega$ ($\omega = \frac{2\pi c}{\lambda}$, where c is the speed of light in vacuum) obtained from experimental data using expression (6). The dispersion of the imaginary part of the dielectric function $\kappa''(\hbar\omega)$ was calculated using the expression

$$\kappa''(\hbar\omega) = 2nk(\hbar\omega). \tag{7}$$

For this calculation, we used the data given in Fig. 2 and

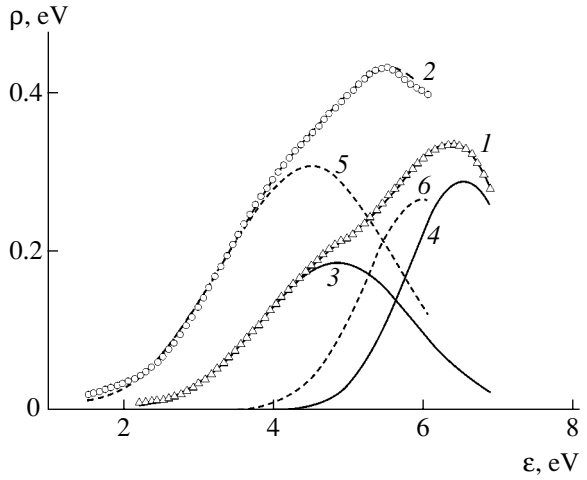

Fig. 3. Dependence of the effective density of states on the energy for the samples (*1*) no. 200 and (*2*) no. 400 and decomposition of the experimental data into two Gaussian curves for the samples (*3*, *4*) no. 200 and (*5*, *6*) no. 400. The sum of the two Gaussian distributions virtually coincides with the experimental curve. The area, the peak position, the width, and the peak height of the first and the second Gaussian distributions for the two samples are, respectively, 0.45, 4.81, 2.03, and 0.17 eV for curve (*3*); 0.56, 6.52, 1.58, and 0.29 eV for curve (*4*); 0.8, 4.47, 2.3, and 0.31 eV for curve (*5*); and 0.52, 5.97, 1.5, and 0.27 eV for curve (*6*).

ignored the dispersion of the refractive index. Indeed, as is seen from Fig. 2, the extinction coefficient in the spectral range under consideration varies within the same limits as in [5, 6], where the refractive index dispersion amounted to several percent of the value determined in the transparency region.

3. Results and Discussion

To characterize the optical properties, we use the Kramers–Kronig relations [7]

$$\kappa'(\hbar\omega) = 1 - \frac{2}{\pi}\int_0^\infty \frac{(\hbar x)\kappa''(\hbar x)d(\hbar x)}{(\hbar\omega)^2 - (\hbar x)^2} = 1 - \hbar^2\frac{4\pi e^2}{m}\int_0^\infty \frac{f(\hbar x)d(\hbar x)}{(\hbar\omega)^2 - (\hbar x)^2}. \quad (8)$$

Here, $\kappa'(\hbar\omega)$ and $\kappa''(\hbar\omega)$ are the real and imaginary parts of the dielectric function, respectively; e and m are the charge and mass of electron, respectively; $f(\hbar\omega)d(\hbar\omega)$ is the oscillator strength within the energy range $d(\hbar\omega)$; $\hbar\omega$ is the light quantum energy; and

$$f(\hbar\omega) = \frac{m}{2\pi^2\hbar^2e^2}(\hbar\omega)\kappa''(\hbar\omega) = \frac{m}{4\pi\hbar^2e^2}\rho(\hbar\omega), \quad (9)$$

where $\rho(\hbar\omega)$ is the effective density of oscillator states.

Let us find the relation between the $\rho(\hbar\omega)$, the density of states $g(\hbar\omega)$, and the function $\varphi(\varepsilon)$ of the electron energy distribution. To this end, we use the relation know as the sum rule [7],

$$N(\varepsilon) \equiv \int_0^\varepsilon f(\hbar x)d(\hbar x), \quad (10)$$

and the known expression relating the density of states $g(\hbar\omega)$ and the oscillator energy distribution function $\varphi(\varepsilon)$,

$$N(\varepsilon) \equiv \int_0^\varepsilon \varphi(\hbar x)g(\hbar x)d(\hbar x). \quad (11)$$

Here, $N(\varepsilon)$ is the total number of oscillators with the energy $\varepsilon = \hbar\omega$ per unit volume of the material. Differentiating (10) and (11), we have

$$\rho(\varepsilon) = \frac{2}{\pi}\varepsilon\kappa''(\varepsilon) = \hbar^2\frac{4\pi e^2}{m}\varphi(\varepsilon)g(\varepsilon). \quad (12)$$

In the case of degeneracy, the function $\varphi(\varepsilon)$ can be approximated by a jump function (a step), while singularities of the function $\rho(\varepsilon)$ in expression (12) characterize specific features of the density of oscillator states $g(\hbar\omega)$.

Figure 3 shows the curves plotted from the experimental data given in Fig. 2 processed in terms of expression (12). It is seen that the function $\rho(\varepsilon)$ has two pronounced features in the energy range under consideration. Namely, this dependence for both samples no. 200 and no. 400 exhibits shoulders (at about 4.7 and 4 eV, respectively) and maxima (at about 6.4 and 5.5 eV, respectively). This gives us ground to decompose the spectra of the density of states into two components. For this purpose, we use a sum of two Gaussian distributions. The result of the decomposition is shown in Fig. 3. According to the model energy spectrum of amorphous carbon [8], the Gaussian curve with the maximum in the low-frequency region (hereafter, the first Gaussian distribution) reflects the contribution of π electrons in the optical absorption, while the curve with the maximum in the high-frequency region (the second Gaussian distribution) can be assigned, according to the same model, to the contribution of σ electrons. As the layer growth temperature increases, the maximum of the first Gaussian distribution moves to lower frequencies and its amplitude grows by almost two times. According to the suggested interpretation, such behavior points to an increase in the number of π electrons with increasing temperature of the synthesis. The maximum of the second Gaussian distribution also shifts to lower frequencies with increasing growth temperature and simultaneously becomes somewhat broader. However, due to the limited spectral range of the measurements, the quantitative estimation of the change in the total number of σ electrons with increasing temperature may be insufficiently correct, which leaves an open field for further investigations.

Our analysis shows that the optical experiment allows one to determine informative parameters of amorphous carbon films, which provide for a more detailed characterization of a material depending on the film growth conditions than does simple determination of the absorption edge. In addition, the proposed approach allowed us to study the spectrum of the density of states of elementary excitations responsible for the optical absorption of amorphous carbon.

Acknowledgments. This study was supported by the Russian Foundation for Basic Research, project no. 03-02-16289.

One of the authors (T. A.) is grateful to the Research Corporation Cottrell College Science Award (grant no. CC4536), National Science Foundation (grant no. DMR0074682), and the UC Foundation, University of Tennessee-Chattanooga.

REFERENCES

1. F. Gaspari, R. V. Kruzelecky, P. K. Lim, *et al.*, J. Appl. Phys. **79**, 2684 (1996).
2. W. C. W. Chan, F. Gaspari, T. Allen, *et al.*, J. Vac. Sci. Technol. A **16**, 889 (1998).
3. M. Born and E. Wolf, *Principles of Optics* (Pergamon, Oxford, 1969; Nauka, Moscow, 1973).
4. V. I. Ivanov-Omskii, I. N. Krivorotov, and S. G. Yastrebov, Fiz. Tekh. Poluprovodn. (St. Petersburg) **29** (9), 121 (1995) [Sov. Phys. Semicond. **29**, 113 (1995)].
5. V. I. Ivanov-Omskii, A. V. Tolmatchev, and S. G. Yastrebov, Philos. Mag. B **73**, 715 (1996).
6. V. I. Ivanov-Omskii, A. Tagliaferro, G. Fanchini, and S. G. Yastrebov, Fiz. Tekh. Poluprovodn. (St. Petersburg) **36**, 117 (2002) [Semiconductors **36**, 110 (2002)].
7. L. D. Landau and E. M. Lifshitz, *Course of Theoretical Physics*, Vol. 8: *Electrodynamics of Continuous Media* (Nauka, Moscow, 1982; Pergamon, New York, 1984).
8. J. Robertson and E. P. O'Reilly, Phys. Rev. B **35**, 2946 (1987).

Translated by M. Basieva

Technical Physics Letters, Vol. 29, No. 10, 2003, pp. 862–864. Translated from Pis'ma v Zhurnal Tekhnicheskoĭ Fiziki, Vol. 29, No. 20, 2003, pp. 58–63.

Tunable Wakefield Waveguide Structure with the Possibility of Mode Selection

A. M. Al'tmark, A. D. Kanareykin, and I. L. Sheinman

St. Petersburg State Electrotechnical University, St. Petersburg, 197376 Russia

e-mail: lab@physics.etu.spb.ru

Received March 6, 2003; in final form, June 16, 2003

Abstract—The possibility to control the frequency spectrum of Cherenkov radiation in a microwave wakefield dielectric waveguide with the aid of an external ferroelectric layer has been studied. Using the proposed multilayer waveguide structure in combination with a special configuration of control electrodes, it is possible both to adjust the wake field frequency spectrum and to attenuate the modes corresponding to beam-deflecting (defocusing) fields in the waveguide. © *2003 MAIK "Nauka/Interperiodica".*

A new method for the acceleration of charged particles, which makes use of the wake fields existing behind electron bunches traveling through a dielectric waveguide structure, is now extensively studied by experimental and theoretical methods [1–4]. A complex investigation of the wakefield acceleration processes in dielectric waveguides is now underway at the St. Petersburg State Electrotechnical University in cooperation with the Argonne National Laboratory (USA).

A widely used type of dielectric waveguide [1–3] is a single-layer structure in the form of an evacuated dielectric (usually ceramic) tube with an internal vacuum channel in which electron bunches are traveling. The external surface of the dielectric tube is metal-coated. Wake field acceleration is based on the energy transfer from a high-current electron bunch to a low-current high-energy bunch. The primary high-current low-energy bunches excite a Cherenkov electromagnetic wave in the waveguide system, the longitudinal electric field component of which (with an electric field intensity of up to ~100 MV/m) is used to accelerate the secondary low-current electron bunch.

However, besides the longitudinal fields, transverse fields of comparable intensity are generated in the wakefield waveguides as well. These fields lead to deviation of the beam from the waveguide axis, whereby charged particles are lost on the walls [3], decreasing the bunch charge and leading to the surface electrical breakdown of the dielectric material.

On the other hand, the necessity of obeying the phase relations (ensuring that a low-current bunch is kept in phase with the accelerating wave) poses strict requirements on the waveguide structure parameters and the bunch positioning. By changing the permittivity of the waveguide system, it is possible to provide for the real-time control of phase relations in the wave–bunch system and to ensure the most favorable energy conditions for the acceleration process [4].

In order to solve these problems, we developed a controlled accelerator system, in which the frequency spectrum of the Cherenkov radiation in the waveguide can be modified with the aid of a thin ferroelectric film applied onto the external surface of the dielectric waveguide [5].

The aim of this study was to create an accelerating system in which the resonance frequency of the dielectric waveguide (excited either by the wake field of the electron beam or by an external microwave source) can be controlled and the transverse fields responsible for the electron beam deviation can be attenuated. Figure 1 shows a schematic diagram of the multilayer structure intended to solve this task. This waveguide structure comprises a layer of high-Q ceramic with the internal

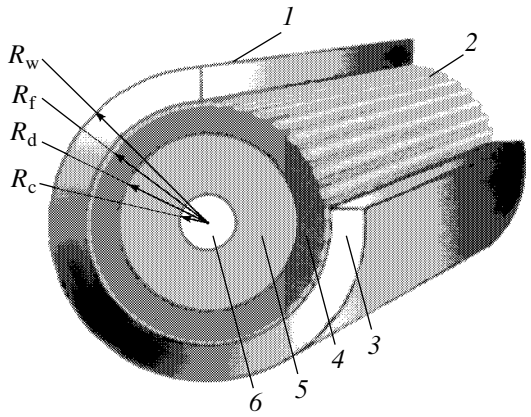

Fig. 1. A schematic diagram of the tunable wakefield waveguide accelerator with transverse deflection mode damping: (*1*) metal coating; (*2*) microstrip electrodes; (*3*) ferrite layer; (*4*) ferroelectric layer; (*5*) dielectric layer; (*6*) vacuum channel.

1063-7850/03/2910-0862$24.00 © 2003 MAIK "Nauka/Interperiodica"

vacuum channel of radius R_c and the external radius R_d, a thin ferroelectric film with the external radius R_f bearing microstrips of insulated longitudinal control electrodes, and a layer of absorbing material (ferrite) with external metal coating of radius R_w.

By applying a dc voltage to the electrodes (creating a field of up to 10 V/μm for the materials employed), it is possible to change the permittivity of the ferroelectric layer and, thus, tune the fundamental frequency of the accelerating waveguide structure. The electrodes can be created using the well-developed technology of photolithography and microetching, which is widely used to obtain microwave phase rotators and adjustable filters based on such ferroelectric films [6]. To implement this technology in our project, it is necessary to solve the following main problems.

(i) The electrode configuration has to provide for the propagation of only the fundamental accelerating mode and attenuation of the deflection modes.

(ii) The electrode system must ensure a maximum amplitude of the constant electric field penetrating into the ferroelectric layer, so as to increase the control range.

(iii) The electrode configuration should introduce the minimum possible electrodynamic losses in the microwave range.

In an accelerating waveguide structure intended to operate in a frequency range of 10–15 GHz, the microelectrode system has to possess a special topology with dimensions obeying certain requirements. For a ferroelectric control film with a thickness of 180–220 μm in a ceramic waveguide characterized by an average frequency of 13.625 GHz, the optimum calculated relation between the layer thickness h and microstrip width d is $h = 3d$ and the interelectrode spacing also has to be approximately equal to d. In the frequency interval of 10–15 GHz, the optimum value of d is 50–60 μm. A potential difference of 0.5–1 kV applied to the interelectrode gap provides for a control field strength of up to 10 V/μm inside the ferroelectric layer. The proposed longitudinal arrangement of the control microstrip electrodes will maintain only the longitudinal electric modes of the microwave wake field. In this configuration, the conducting microstrips on the ferroelectric surface can be used both as contacts for applying the constant control field and as a system of attenuation of the transverse deflection modes.

In developing the aforementioned microelectrode topology, we used the filtration method proposed by Chojnacki *et al.* [7], according to which the transverse deflection modes are attenuated by a longitudinally anisotropic (segmented) external conducting waveguide shell, rather than by a continuous isotropic external metal film. The main idea of the transverse mode attenuation by providing a purely longitudinal conductivity of the waveguide shell through application of a system of axial insulated conductors was originally proposed in [7], and the results of numerical modeling and first experiments were reported in [8].

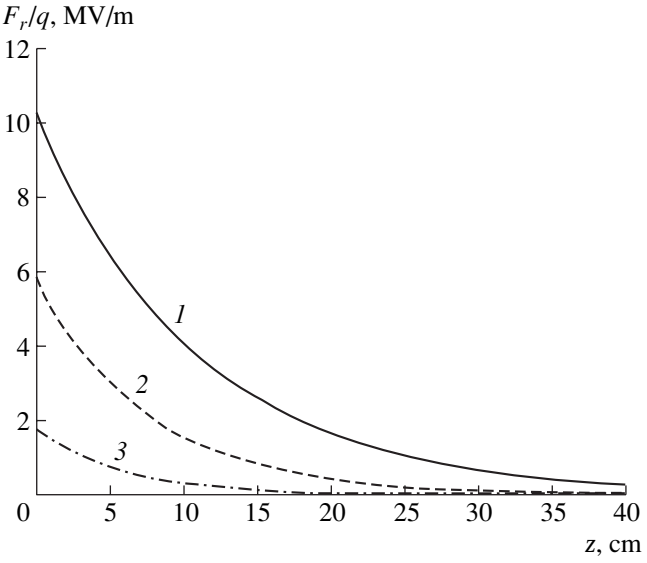

Fig. 2. Plots of the radial deflection field amplitude of the first transverse mode versus distance z behind the electron bunch for the waveguide structures with various ferrite layer thicknesses $\Delta = 0.002$ (*1*), 0.005 (*2*), and 0.05 cm (*3*).

The existence of hybrid modes in dielectric waveguides requires both axial and azimuthal surface electric currents to flow in the waveguide shell. If the external conductor admits only the axial surface current (as in our system configuration in Fig. 1), the deflection modes will be absorbed outside the waveguide space surrounded by the longitudinal electrodes (these modes will decay in the form of surface waves in an external microwave absorber). Thus, the proposed special configuration of microstrip electrodes ensures propagation of a single fundamental mode in the waveguide.

The results of numerical modeling and experiments [8] showed that the axially conducting shell does not affect the accelerating field, while ensuring exponential damping of the transverse fields over a distance of several microwave periods.

Figure 2 shows the structure of the radial field of the first transverse waveguide mode as a function of the distance z behind a bunch possessing a charge of Q = 100 nC and a length of 0.4 cm, shifted by $r_0 = 0.001$ cm relative to the waveguide axis. The calculations were performed for three values of the ferrite layer thickness Δ and the following waveguide parameters: R_c = 0.5 cm; $R_d = 0.6$ cm; $R_f = 0.6233$ cm; $R_w = R_f + \Delta$; ε_{diel} = 16; $\varepsilon_{ferroel} = 200$; $\sigma_{ferrite} = 0.1\ \Omega^{-1}\ m^{-1}$; $\mu_{ferrite} = 10$; $\varepsilon_{ferrite} = 1$. As can be seen from Fig. 2, an increase in the thickness of the ferrite layer (absorbing energy and characterized by exponential decay of the deflection mode amplitude in the waveguide) provides for an additional decrease in the deflection mode amplitude in the vacuum channel as a result of redistribution outside

the waveguide space surrounded by the longitudinal electrodes. For accelerating and accelerated electron bunches separated by $z = 23$–25 cm from each other (which corresponds to about 10λ, λ being the wavelength corresponding to the fundamental frequency of 13.625 GHz), the radial field of the first mode is attenuated by a factor of 100 and above, to become comparable with or smaller than the zero-order deflection mode field. According to our estimates, the latter does not exceed 100 V/m for the proposed geometry and, in the absence of an additional ferrite layer in the traditional waveguide, is negligibly small as compared to the radial field amplitude of the first mode.

Thus, a longitudinal electrode structure used to control the permittivity of the ferroelectric layer, in combination with an additional absorbing shell, also ensures attenuation of the transverse deflection modes. The possibility of effective control over the waveguide frequency spectrum is completely retained. The possibility of real-time adjustment of the waveguide frequency (and, hence, of the phase velocity of the accelerating wave) is a significant advantage of the ceramic waveguide structure over the standard vacuum waveguides. This opens the way to wide use of the proposed structure in systems requiring wave–beam synchronization.

Acknowledgments. This study was supported by a grant from the Ministry of Education of the Russian Federation and the Committee on Science and High School of St. Petersburg (project no. PD02-1.2-104) and by a grant from DoE SBIR (no. DE-FG02-02ER83418).

REFERENCES

1. A. D. Kanareykin, I. L. Sheinman, E. A. Nenasheva, *et al.*, in *Proceedings of the International Conference "Physics at the Turn of the 21st Century," St. Petersburg, 1998*, pp. 57–58.
2. M. Rosing and W. Gai, Phys. Rev. D **42**, 1829 (1990).
3. W. Gai, A. D. Kanareykin, A. Kustov, and J. Simpson, Phys. Rev. E **55**, 3481 (1997).
4. J. G. Power, W. Gai, and A. D. Kanareykin, AIP Conf. Proc. **569**, 605 (2001).
5. A. D. Kanareykin, I. L. Sheinman, and A. M. Al'tmark, Pis'ma Zh. Tekh. Fiz. **28** (21), 75 (2002) [Tech. Phys. Lett. **28**, 916 (2002)].
6. O. Vendik, *Ferrielectrics in Microwave Technology* (Sov. Radio, Moscow, 1979).
7. E. Chojnacki, W. Gai, C. Ho, *et al.*, J. Appl. Phys. **69**, 6257 (1991).
8. W. Gai and C.-H. Ho, J. Appl. Phys. **70**, 3955 (1991).

Translated by P. Pozdeev

Technical Physics Letters, Vol. 29, No. 10, 2003, pp. 865–866. Translated from Pis'ma v Zhurnal Tekhnicheskoĭ Fiziki, Vol. 29, No. 20, 2003, pp. 64–68.

Minority Carrier Lifetimes in Polycrystalline Silicon Treated with Liquid Metals

B. Sapaev

Physicotechnical Institute, "Solar Physics" Research and Production Corporation, Academy of Sciences of the Republic of Uzbekistan, Tashkent, Uzbekistan

e-mail: atvi@physic.uzsci.net

Received May 8, 2003

Abstract—The effect of treatment at 800°C in various liquid metal solvents (Sn, Bi, Pb) on the minority carrier lifetime τ in polycrystalline silicon has been studied. The results of dc photoconductivity measurements show evidence of the external gettering effect, the best gettering being observed when tin was used as the solvent. A 2-h treatment leads to a twofold increase in the τ value. The experimental data indicate that the external gettering effect can be used in practice. *© 2003 MAIK "Nauka/Interperiodica".*

Polycrystalline silicon (poly-Si) is a promising material for solar cells [1] due to low cost and good technological properties. However, the solar cells fabricated using poly-Si are still characterized by relatively low conversion efficiencies. This is explained by a high rate of the surface and intergranular recombination caused by the presence of various dangling bonds, by low values of the minority carrier lifetime τ, etc. In order to obtain solar cells with increased efficiency, it is necessary to improve these characteristics. This task can be solved by various methods [2].

Previously [3], it was demonstrated that the minority carrier lifetime in poly-Si can be increased by gettering impurities and inclusions from the material through treatment in liquid tin. The present study was aimed at determining the influence of the liquid metal type and the treatment duration on the characteristics of poly-Si. The experiments were performed with three metals, bismuth, lead, and tin, widely used in liquid phase epitaxy of silicon.

The choice of Bi, Pb, and Sn as potential getters is explained by two circumstances. On the one hand, silicon is virtually insoluble in these metals at $T = 700$°C and is only slightly soluble at 800–900°C [4]. On the other hand, these metals are good solvents for GaAs, which provides for the growth of GaAs layers without any negative influence upon the substrate. It was demonstrated [5, 6] that epitaxial GaAs layers can be grown from these metal solvents on poly-Si substrates even without forming special buffer layers matching the crystal lattice parameters of the film and substrate.

In this context, it was of interest to study the influence of these metal solvents on the properties of poly-Si in various regimes used for the epitaxial growth of GaAs [5, 6], since the properties of substrates affect some parameters of the epitaxial films. This is especially important from the standpoint of creating cascade structures for solar cells, in which the bottom narrow-band element is based on poly-Si.

It is suggested to increase the properties of poly-Si substrates through gettering the defects with liquid metal solvents, which is based on the exchange of freely mixing elements between solvent and substrate. The outdiffusion of excess impurity elements from a substrate to solution melt purifies a subsurface layer to a certain extent from various undesired elements, which leads to an increase in the minority carrier lifetime [2, 7]. The value of τ depends both on the time of treatment in a liquid metal and on the metal type, since the segregation coefficients of impurities in various metal are known to be different [8, 9].

The gettering process was effected at 800°C. The initial material was poly-Si of the *p* type with a resistivity of $\rho \approx 2.0$–$2.5\ \Omega$ cm and a minority carrier lifetime of $\tau \approx 10^{-6}$ s, which are typical parameters of the substrates used for the fabrication of solar cells [1, 10]. The samples had the form of disks with a diameter of 2.0 cm and a thickness of 1.0 ± 0.1 mm (after all pretreatment stages, including grinding and chemical polishing, the sample thickness was 0.8 ± 0.05 mm). All plates, including both the initial (control) ones and those upon gettering treatments, were cut into six identical 6×4 mm samples so as to obtain data averaged over each plate.

The experimental setup, the sample preparation stage, and the gettering procedure were analogous to those described previously [3]. After termination of the gettering process, the samples were ground to remove the damaged surface layer with a thickness of 50 ± 2.0 μm (the sample thickness was measured with a micrometer to within 1.0 μm). Then, the ohmic contacts of In (50%)–Sn (50%) eutectic were applied by thermal deposition in vacuum onto the samples heated to 120°C.

1063-7850/03/2910-0865$24.00

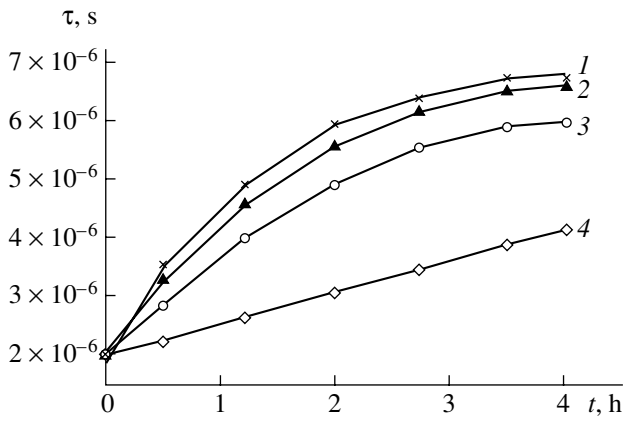

The plots of minority carrier lifetime τ for poly-Si substrates versus the time of treatment *t* at 800°C in various liquid metals: (*1*) Sn; (*2*) Bi; (*3*) Pb; (*4*) control.

The minority carrier lifetime τ was determined from data on the dc photoconductivity and on the quenching of photo emf generated by pulsed illumination of a sample [11, 12]. The results of these measurements are presented in the figure, from which it can be seen that a 2-h treatment leads to an almost twofold increase in τ, irrespective of the metal solvent, in comparison to that in the control samples treated in the same reactor without contact with the gettering solution. The rate of growth in the τ value decreases with the treatment duration, exhibiting saturation at a gettering time of 4–5 h. The data presented in the figure indicate that the best result is obtained with tin, while bismuth shows a somewhat less pronounced gettering effect.

An increase in the minority carrier lifetime as a result of gettering is related to deformation of the surface structure, which provides a sink for uncontrolled rapidly diffusing impurities. Since the bulk recombination in poly-Si is determined by the residual content of rapidly diffusing deep donors, such as Cu, Ni, Fe, Cr [7], it is suggested that the treatment at 800°C leads to decomposition of the solid solutions of silicon with these elements and accelerates their outdiffusion from bulk to the sample surface. This leads to the growth in τ with saturation upon the treatment for 4–5 h (see the figure). The trend in the variation of τ depending on the metal solvent type suggests that the mechanical stress depends on the covalent radius of the metal solvent [4, 9].

The obtained experimental results show evidence that the external gettering offers effective means of increasing τ and can be used in practice. The poly-Si substrates gettered as described above can be successfully used both as elements of solar cells and as substrates for the growth of films of some other materials, such as A_3B_5 semiconductor compounds, for various applications.

REFERENCES

1. A. L. Fahrenbruch and R. H. Bube, *Fundamentals of Solar Cells* (Academic Press, New York, 1987; Énergoatomizdat, Moscow, 1987).
2. *Polycrystalline and Amorphous Thin Films and Devices*, Ed. by L. L. Kazmerski (Academic, New York, 1980; Mir, Moscow, 1983).
3. B. Sapaev, A. S. Saidov, and M. S. Saidov, Geliotekhnika, No. 2, 95 (2001).
4. M. Hansen and K. Anderko, *Constitution of Binary Alloys* (McGraw-Hill, New York, 1958; Metallurgizdat, Moscow, 1962), Vol. 2.
5. B. Sapaev, A. S. Saidov, A. Kutlimratov, and U. T. Davlatov, Vestn. Gulistansk. Gos. Univ., No. 2, 40 (2001).
6. B. Sapaev, N. M. Mukhamedshina, A. S. Saidov, *et al.*, in *Proceedings of the 4th International Conference "Modern Problems of Nuclear Physics:" Book of Abstracts, Tashkent, 2001*, pp. 191–192.
7. V. I. Fistul', *Introduction to Semiconductor Physics* (Vysshaya Shkola, Moscow, 1984).
8. V. M. Andreev, L. M. Dolginov, and D. N. Tret'yakov, *Liquid-Phase Epitaxy in Technology of Semiconductor Devices* (Sov. Radio, Moscow, 1975).
9. M. S. Saidov, Doctoral Dissertation (Tashkent, 1970).
10. M. M. Koltun, *Optics and Metrology of Solar Cells* (Nauka, Moscow, 1985).
11. E. V. Kuchis, *Methods of Hall Effect Studies* (Nauka, Moscow, 1974).
12. L. P. Pavlov, *Methods for Determination of Key Parameters of Semiconducting Materials: A Textbook for Institutes of Higher Education* (Vysshaya Shkola, Moscow, 1987).

Translated by P. Pozdeev

Technical Physics Letters, Vol. 29, No. 10, 2003, pp. 867–870. Translated from Pis'ma v Zhurnal Tekhnicheskoĭ Fiziki, Vol. 29, No. 20, 2003, pp. 69–76.

Semiconductor–Propolis Heterojunction

S. I. Drapak, V. B. Orletskiĭ, Z. D. Kovalyuk, and V. V. Netyaga

Frantsevich Institute for Problems of Materials Science (Chernivtsy Department), National Academy of Sciences of Ukraine, Chernivtsy, Ukraine

e-mail: chimsp@unicom.cv.ua

Received March 31, 2003; in final form, May 27, 2003

Abstract—A heterojunction between *p*-type indium monoselenide and propolis (bee glue) has been created for the first time. The influence of technological factors on the electrical properties of the heterojunction has been studied. It is demonstrated that propolis behaves similarly to a *p*-type semiconductor. The heterojunction possesses a significant photosensitivity in the near infrared range. The prospects of using photodetectors of the new type are discussed. © *2003 MAIK "Nauka/Interperiodica".*

Investigations into the properties of heterojunctions of various types are continuously expanding, which provides a basis both for increasing the parameters of traditional semiconductor devices and for finding new functional relations, which stimulates the development of novel devices and systems [1]. Some recent papers reported the results of investigations of the physical properties of biological objects [2] and heterojunctions between semiconductors and biological media [3–5]. Provided that proper technological solutions are found, the main photoelectric characteristics of such structures can be comparable with or even higher than those of traditional devices [5].

Below we present the results of the first investigation of a semiconductor–propolis heterojunction, the semiconductor being represented by *p*-type indium monoselenide (*p*-InSe). Propolis (bee glue) is widely used in pharmaceuticals and cosmetics. This product of the living activity of honey bees represents a highly complicated mixture of organic substances, including tarry compounds (50–55%), wax (up to 30%), and essential oils and balms (about 10%). In addition, propolis contains organic acids, antibiotics, a number of vitamins, many trace elements (aluminum, vanadium, iron, calcium, silicon, manganese, strontium), and a number of natural enzymes (e.g., carotene) [6]. There is extensive literature devoted primarily to the chemical composition of propolis (see, e.g., [7]). Each subsequent analysis reveals new components in this substance. The physical measurements are reduced mostly to determining the density, the temperatures of phase transitions, etc.

We have undertaken the first attempt to use propolis as a material for photosensitive devices. For this purpose, we prepared sample heterostructures using the *p*-InSe:Cd substrates with a charge carrier density of $p \approx 10^{14}$ cm^{-3} at $T = 300$ K. The choice of this semiconductor was determined by a number of factors, the main of which are as follows. First, the possibility of obtaining plates with an atomically smooth surface and low density of surface states (below 10^{10} cm^{-2}) by cleavage of an InSe ingot in air. Second, the ability of this semiconductor to create rectifying barriers in contacts with various materials possessing both lower and higher electron work function [8].

The experiments were performed with samples of two kinds. Heterostructures of the first type were prepared by applying one drop of an ethanol solution of propolis to freshly cleaved semiconductor substrates with a metal (silver) contact preliminarily deposited onto the rear side. In order to obtain an organic film of uniform thickness, the substrate with applied propolis was treated in a centrifuge. The electrode on the propolis side was also made of silver. The thicknesses of propolis films varied from 10 to 30 μm, and their specific conductivities were on the order of 10^{-6}–10^{-7} Ω^{-1} cm^{-1}. In what follows, these samples will be referred to as the propolis film (PF) type. Structures of the second type represented the semiconductor in contact with a solution of propolis in 96% ethyl alcohol. These structures, referred to as propolis solution (PS) type, are virtually identical to those employed in semiconductor–protein junctions [4]. The thickness of an ethanol solution layer varied within 1–1.5 mm and the specific conductivity was on the order of 10^{-3}–10^{-4} Ω^{-1} cm^{-1}.

The stationary current–voltage (*J*–*V*) characteristics of the *p*-InSe–propolis heterojunctions of both types exhibit clearly pronounced rectification effect (Fig. 1, curves *1* and *2*): for a bias voltage of 1.5–2 V, the forward current exceeds the reverse current by not less than two orders of magnitude for PS and by not less than three orders of magnitude for PF structures. The forward direction corresponds to the bias voltage source plus on *p*-InSe for PS and on propolis for PF. Taking into account that the resistivity of propolis in PF

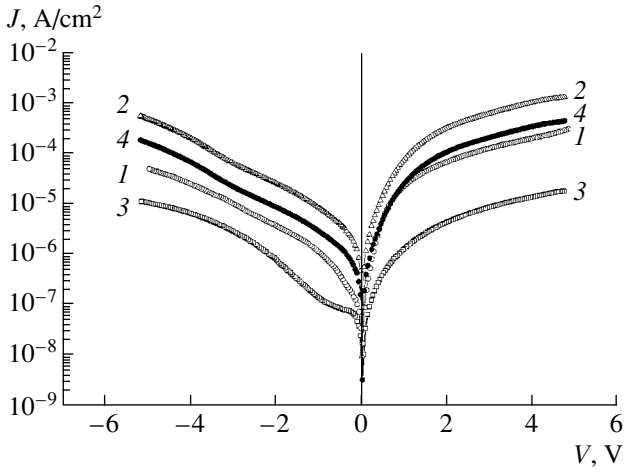

Fig. 1. The stationary current–voltage characteristics of the *p*-InSe heterojunctions with propolis and ethanol solutions: (*1*) *p*-InSe–PF; (*2*) *p*-InSe–PS; (*3*) *p*-InSe–96% ethanol; (*4*) *p*-InSe–70% ethanol at $T = 290$ K. The forward current direction corresponds to the bias voltage source minus (*1*) and plus (*2–4*) on the organic phase (propolis).

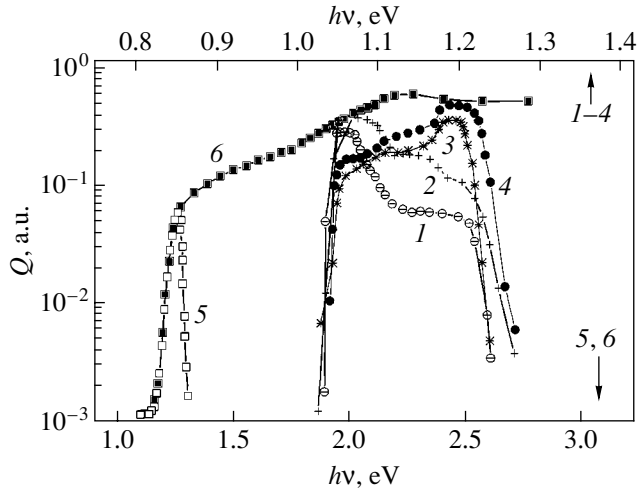

Fig. 2. The typical spectra of the relative quantum efficiency of photoconversion at the (*1*, *2*) *p*-InSE–PF, (*3*, *4*) *p*-InSE–PS, and (*5*, *6*) *p*-InSE–ethanol heterojunctions illuminated from the side of (*1*, *3*, *5*) semiconductor and (*2*, *4*, *6*) organic phase ($T = 290$ K).

is higher than in PS, this fact may indicate that the given biological medium in contact with InSe behaves as a semiconductor of the *p*-type.

For comparison, Fig. 1 (curve *3*) shows a stationary *J–V* curve of the *p*-InSe–96% ethanol junction. Note that the reverse branch of this junction is characteristic of the metal–dielectric–semiconductor structures [12]. In this case, an increase in the current density observed in negatively biased samples ($|V| \approx 1.5$–2 V) can be related to a resonance tunneling through a space charge region and the dielectric layer [9]. In a contact of *p*-InSe with 70% ethanol (Fig.1, curve *4*), the current density in both the forward and reverse directions increases in comparison with that for 96% ethanol, which is evidence of increasing conductivity of the liquid phase. In this case, the molecules of alcohol forming an electrochemical Helmholtz layer [10], play the role of a high-ohmic component of the structure. For the *p*-InSE–70% ethanol junction, an increase in the current density observed in the region of reverse bias voltages $|V| \approx 1.5$–2 V is significantly lower as compared to that for a 96% ethanol. This can be related to a decrease in the thickness of a dielectric layer at the interface between the two phases in contact [9]. Analogous results (increasing current density in both directions) is observed for the contacts of *p*-InSe with an ethanol solution of propolis.

The capacitance–voltage (*C–V*) characteristics of the semiconductor–propolis heterojunctions of both types are linearized in the C^2 versus V coordinates for the bias voltages up to 2 V, which is typical of sharp heterojunctions and can be considered as evidence of a sharp interface in the system studied. In addition, the *C–V* characteristics vary with the frequency ω at which the measurements are performed, representing a family of parallel lines, which is typical of the structures with large serial resistances [11]. In this case, the contact potential difference V_{bi}, as determined by extrapolating $V_0(\omega)$ to zero frequency [11], amounted to 1.24 and 1.52 eV for PS and PF, respectively. These values agree well with the barrier heights determined by extrapolating the linear portions of the *J–V* curves to the voltage axis (1.2 and 1.48 eV for PS and PF, respectively). In the course of a long-term (6 month) storage, the electrical characteristics of the *p*-InSe–propolis heterojunctions of both types remained virtually unchanged and were well reproduced, which is evidence of the absence of irreversible processes both at the semiconductor–propolis interface and in the propolis layer.

Under illumination, *p*-InSe–propolis heterojunctions exhibit photo emf, whereby propolis acquires negative charge in PS and positive in PF structures, which is consistent with the forward current direction in the corresponding heterojunctions. The maximum values of the open circuit voltage U_{oc} were observed for samples illuminated from the side of propolis and amounted to $U_{oc} \sim 0.45$ and 0.24 V for PF and PS, respectively, for an incident light intensity of 100 mW/cm^2 (in the *p*-InSe–ethanol system, the values of U_{oc} measured under otherwise identical conditions were much lower than those in the *p*-InSe–PS junctions). To determine the relative quantum efficiency $Q(h\nu)$ of the structures studied, the voltage was measured on a linear portion of the illumination–voltage characteristic and normalized to the number of incident photons.

Figure 2 shows the typical spectra of quantum efficiency $Q(h\nu)$ measured at 300 K for various semiconductor–propolis heterojunctions (curves *1–4*) illuminated in different modes. For comparison, we also

present the $Q(h\nu)$ curves of the *p*-InSe–ethanol heterojunctions (curves *5* and *6*). The latter are qualitatively similar to the spectra of photosensitivity of a semiconductor–distilled water [10] or semiconductor–protein [4] systems and can be interpreted in an analogous way. In the presence of propolis (in both PS and PF forms), the photosensitivity band of the heterojunctions shifts toward longer wavelengths.

A characteristic feature of the photosensitivity of *p*-InSe–propolis heterojunctions is that, within generally the same band, the peak of $Q(h\nu)$ is shifted toward longer waves for PF and toward shorter wavelengths for PS structures (Fig. 2, curves *1–4*). This difference can be explained, first, by the relative electrical parameters of two phases in contact, whereby the active region is localized in the more high-ohmic component (i.e., in semiconductor for the InSe–PS system and in propolis for the InSe–PF system). Second, this shape of the $Q(h\nu)$ curve is characteristic of nonideal structures with a large density of surface states at the heteroboundary [12]. Third, the $Q(h\nu)$ spectrum may be correlated with the optical transmission spectra of the two materials in contact [3]. However, the latter assumption is at variance with the experimental data (the results of optical investigations will be reported in a forthcoming paper).

The most interesting behavior is observed for the *p*-InSe–PF system, whereby the voltage drops mostly on the propolis layer. The forward branch of the current–voltage characteristic of this heterojunction (with allowance of the serial differential resistance at T = 290 K) can be divided into three regions (Fig. 3, curve *1*): (i) at low bias voltages, $J \sim \exp(eV/nkT)$ with $n \sim 2$; (ii) for $V \approx 4$–9 V, $J \sim \exp(\alpha V + \beta T)$, where α and β are the parameters independent of voltage and temperature; (iii) for $V > 8.7$–9 V, $J \sim \exp(eV/nkT)$ with $n \sim 1$. Similar forward branches of the *J–V* curves were observed for ZnTe–ZnSe heterojunctions, in which the forward current represented a superposition of the recombination current in the space charge region (J_{gr}), tunneling current (J_t), and over-barrier current (J_d) components [13]. However, in our case, the *J–V* curves in all regions exhibit parallel shift with the temperature (Fig. 3, curves *2* and *3*), which is evidence of the tunneling current present at all values of the forward bias. This behavior can be explained either by the presence of a dielectric gap at the heteroboundary [10] or by the influence of a reversely biased diode realized (in the simplest variant) between the Helmholtz layer and the Gouy–Chapman layer in propolis (or between an adsorbate and the Helmholtz layer). The latter assumption seems to be more realistic, since it also explains a considerable difference between the values of the contact potential difference determined from the current–voltage characteristic and photo emf measurements.

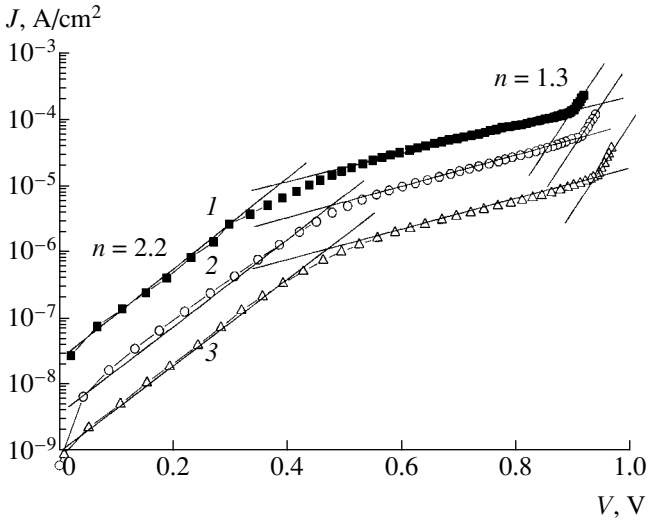

Fig. 3. Forward branches of the current–voltage characteristics of *p*-InSe–PF heterojunctions measured at various temperatures T = 290 (*1*), 268 (*2*), and 238 K (*3*).

Although the mechanism of photosensitivity of the *p*-InSe–propolis heterojunctions is incompletely clear, it is possible to make some conclusions.

(i) The results of our first experiments with the semiconductor–propolis allow the spectrum of materials used in photodetectors for the near infrared range to be expanded.

(ii) In *p*-InSe–propolis heterojunctions, propolis behaves as a *p*-type semiconductor.

(iii) Determining the substance (or a group of substances) responsible for the photosensitivity of *p*-InSe–propolis heterojunctions in the infrared range and increasing the content of this component in propolis may lead to the development of photodetectors with competitive photoelectric characteristics, as was done in [5].

In addition, it would be of interest to study the heterojunctions of propolis with other biological media (including green leaves), since this substance is capable of preventing living matter from decaying over a time period of up to several years [6].

REFERENCES

1. Zh. I. Alferov, Fiz. Tekh. Poluprovodn. (St. Petersburg) **32** (1), 3 (1998) [Semiconductors **32**, 1 (1998)].
2. V. P. Grishchuk, S. A. Davidenko, I. D. Zholner, *et al.*, Pis'ma Zh. Tekh. Fiz. **28** (21), 36 (2002) [Tech. Phys. Lett. **28**, 896 (2002)].
3. V. Yu. Rud', Yu. V, Rud', and V. Kh. Shpunt, Fiz. Tekh. Poluprovodn. (St. Petersburg) **31** (2), 1 (1997) [Semiconductors **31**, 97 (1997)].
4. Yu. V. Rud', V. Yu. Rud', I. V. Bodnar', *et al.*, Fiz. Tekh. Poluprovodn. (St. Petersburg) **33**, 1201 (1999) [Semiconductors **33**, 1093 (1999)].

5. R. Rinaldi, E. Branca, R. Cingolani, *et al.*, Appl. Phys. Lett. **78**, 3541 (2001).
6. V. V. Dontsov and V. I. Dontsov, *Medicinal Plants and Apiculture Products* (Floks, Nizhni Novgorod, 1992).
7. N. G. Takaisi-Kikuni, Planta Med. **60**, 222 (1994).
8. J. Martine-Pastor, A. Segura, J. L. Valdes, and A. Chevy, J. Appl. Phys. **62**, 1477 (1987).
9. G. G. Kareva, M. I. Viksler, I. V. Grekhov, and A. F. Shulkin, Fiz. Tekh. Poluprovodn. (St. Petersburg) **36**, 953 (2002) [Semiconductors **36**, 889 (2002)].
10. Yu. V. Gurevich and F. V. Pleskov, *Photoelectrical Chemistry of Semiconductors* (Nauka, Moscow, 1983).
11. A. A. Lebedev, A. A. Lebedev, and D. V. Davydov, Fiz. Tekh. Poluprovodn. (St. Petersburg) **34** (1), 113 (2000) [Semiconductors **34**, 115 (2000)].
12. A. G. Milnes and D. L. Feucht, *Heterojunctions and Metal–Semiconductor Junctions* (Academic, New York, 1972; Moscow, 1975).
13. V. E. Baranyuk and V. P. Makhniĭ, Fiz. Tekh. Poluprovodn. (St. Petersburg) **31**, 1074 (1997) [Semiconductors **31**, 918 (1997)].

Translated by P. Pozdeev

Technical Physics Letters, Vol. 29, No. 10, 2003, pp. 871–872. Translated from Pis'ma v Zhurnal Tekhnicheskoĭ Fiziki, Vol. 29, No. 20, 2003, pp. 77–80.

A Xenon–Iodine Electric Discharge Bactericidal Lamp

A. K. Shuaibov, L. L. Shimon, and I. A. Grabovaya

Uzhgorod State University, Uzhgorod, Ukraine

e-mail: ishev@univ.uzhgorod.ua

Received April 11, 2003

Abstract—We present the working characteristics of a continuous UV lamp emitting at λ = 206 nm, pumped by a longitudinal glow discharge. The pressure of the working Xe–I_2 gas–vapor mixture was within 0.1–10 kPa. The power deposited in the discharge was varied within 10–130 W. The current–voltage characteristics, the emission spectra in a 200–600 nm wavelength range, the line emission intensity as a function of the power deposited in the discharge plasma, and the partial pressure of xenon in the lamp were studied. It is established that the lamp operates in the range of 206–342 nm on a resonance line of iodine at 206 nm and on the bands at 253 nm [XeI(B–X)] and 342 nm [I_2(B–X)]. Not less than half of the output UV emission power is concentrated in the bactericidal spectral interval (around λ = 206 nm). The total UV emission power of the lamp reaches 6–7 W at an efficiency of ≤5%. *© 2003 MAIK "Nauka/Interperiodica".*

High-power sources of spontaneous UV radiation, capable of emitting in a bactericidal spectral interval using the electron-vibrational transitions in inert gas monohalides and halogen dimers, are widely used in photochemistry, ecology, biophysics, and medicine [1, 2]. Excimer halogen lamps pumped with longitudinal dc discharge are among the sources most simple from the standpoint of manufacturing technology [3–5]. Unfortunately, the working life of such lamps employing highly reactive fluorine and chlorine-containing media does not exceed 100 h, being determined by gas purity and the rate of interaction between halogens and the electrodes and walls of the discharge tube. Passage to a less aggressive halogen-containing media based on bromine and iodine allows the working life of the such discharge lamps to be increased almost tenfold [6]. In the case of iodine-containing media, the main radiation component is that at λ = 206 nm, but the relative contributions of XeI* and I_2^* molecules to the total emission power previously remained unknown.

Here we present the results of investigations aimed at optimization of the output characteristics of a continuous discharge UV lamp employing a xenon–iodine gas–vapor mixture. The glow discharge was initiated in a quartz discharge tube transmitting not less that 70% of the total intensity at λ = 200 nm. The discharge tube had an internal diameter of 14 mm and an interelectrode distance of 190 mm. The device was equipped with cylindrical electrodes made of nickel. High-purity crystalline nickel was contained into a special finger behind the anode.

The discharge emission spectrum was analyzed by a monochromator of the MDR-2 type and detected by a photomultiplier (FEU-106). The detector was calibrated with respect to the relative spectral sensitivity using standard lamps of the SI 8-200U (Δλ = 400–1000 nm) and DVS-25 (200–400 nm) types. The discharge was power supplied from a high-voltage rectifier ($I_{ch} \le -70$ mA; $U_{ch} \le 10$ kV). Prior to being filled with xenon, the discharge tube was evacuated to a residual pressure of 5 Pa. The quartz tube was air-cooled by a ventilator, so that the temperature of the finger with iodine was in most cases close to room temperature. The tube temperature did not exceed 35–40°C, so that the iodine pressure was within 130–200 Pa [7]. The total UV power was measured using a power meter of the Quartz-01 type as described in [8, 9]. A filter (UFS-5) placed in front of the detector head of the power meter rejected radiation in the visible and infrared range. The electric power deposited in the plasma was varied in a range from 10 to 130 W. Stable initiation of the glow discharge was observed at a voltage drop between electrodes ≤3.0 kV. The current–voltage characteristics corresponded to the subnormal and normal stages of glow discharge.

Figure 1 shows the emission spectrum of the lamp (without correction for the relative spectral sensitivity of the monochromator and photomultiplier). The most intense emission line within the bactericidal spectral interval corresponds to the resonance line of iodine observed at λ = 206 nm. Because of incomplete vibrational relaxation process at a low gas pressure, the bands at 253 nm [XeI(B–X)] and 342 nm [I_2(B–X)] are strongly broadened and may also contribute to the total UV emission from the discharge plasma. For a partial xenon pressure of P(Xe) = 266 Pa (close to the optimum level ensuring maximum UV emission power), a distribution of the relative intensity of emission in the I_2^* and XeI_2^* molecular lines and the resonance line of iodine was 1.0/0.3/0.7.

1063-7850/03/2910-0871$24.00 © 2003 MAIK "Nauka/Interperiodica"

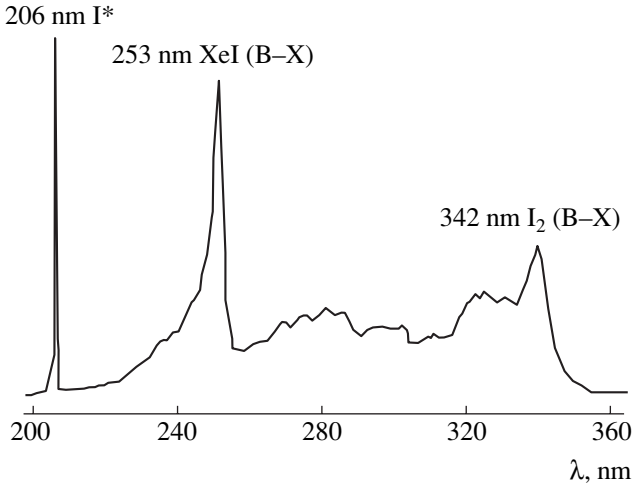

Fig. 1. The emission spectrum of a dc glow discharge in a xenon–iodine gas–vapor mixture at P(Xe) = 133 Pa.

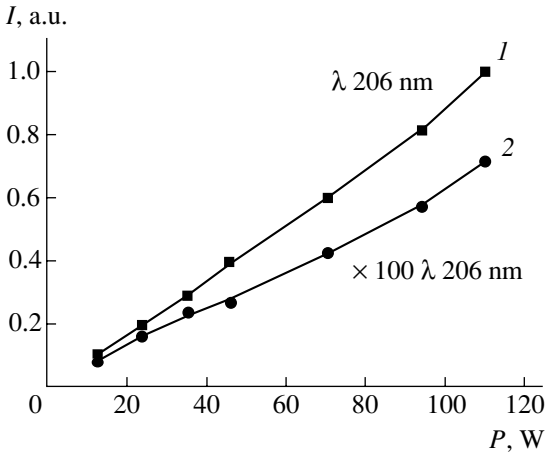

Fig. 2. Plots of the intensity of atomic emission lines at (*1*) 206 nm [I(I)] and (*2*) 476 nm [Xe(I)] versus electric power deposited in the glow discharge at P(Xe) = 133 Pa.

In the visible spectral range, the emission spectrum exhibited the most intense atomic emission lines of xenon and iodine on the background of the continuum. The plots of emission intensity in the I(I) (Fig. 2) and Xe(I) lines versus glow discharge power were close to linear. This fact indicates that excitation of both xenon and iodine atoms in the discharge plasma is produced by direct electron impact or, for iodine molecules only, by dissociative excitation with electrons.

The absolute output UV emission power from the side surface of the discharge tube measured in a spectral interval from 200 to 400 nm amounted to 6–7 W at an efficiency of ≤5%. The working life with respect to the UV emission in a gasostatic operation mode was not less than 300 h.

In conclusion, we have demonstrated that the most intense emission of a stationary low-density electric discharge plasma formed in xenon–iodine gas–vapor mixture is observed in a bactericidal emission interval at λ = 206 nm [I(I)]. Other significant output radiation power components represent the wideband emission due to the electron-vibrational transitions in XeI(B–X) and I_2 molecules in the interval from 230 to 350 nm. The optimum partial pressure of xenon in the working gas–vapor mixture is within 130–270 Pa. The total UV emission power of the lamp reaches 6–7 W at an efficiency of ≈5%.

REFERENCES

1. I. W. Boyd and J.-X. Zhang, Mater. Res. Soc. Symp. Proc. **617**, J4.4.1 (2000).
2. G. S. Polunin, V. V. Kourencov, and E. G. Polunina, J. Refract. Surg. **14**, S230 (1998).
3. A. P. Golovitskiĭ and S. N. Kan, Opt. Spektrosk. **75**, 604 (1993) [Opt. Spectrosc. **75**, 357 (1993)].
4. A. I. Panchenko and V. F. Tarasenko, Opt. Spektrosk. **84**, 389 (1998) [Opt. Spectrosc. **84**, 337 (1998)].
5. A. K. Shuaibov, A. I. Dashchenko, and I. V. Shevera, Kvantovaya Élektron. (Moscow) **31**, 371 (2001).
6. M. I. Lomaev and V. F. Tarasenko, Proc. SPIE **4747**, 390 (2002).
7. *Properties of Inorganic Compounds: A Handbook* (Khimiya, Leningrad, 1983).
8. A. K. Shuaibov, L. L. Shimon, A. I. Dashchenko, and I. V. Shevera, Prib. Tekh. Éksp., No. 1, 104 (2002).
9. A. K. Shuaibov, L. L. Shimon, A. I. Dashchenko, and I. V. Shevera, J. Phys. Stud. **5** (2), 131 (2001).

Translated by P. Pozdeev

Technical Physics Letters, Vol. 29, No. 10, 2003, pp. 873–875. Translated from Pis'ma v Zhurnal Tekhnicheskoĭ Fiziki, Vol. 29, No. 20, 2003, pp. 81–87.

Effective Generation of Electron Beams in an Abnormal Discharge with Increased Photoelectron Emission from a Cathode

A. P. Bokhan, P. A. Bokhan, and Dm. E. Zakrevsky*

Institute of Semiconductor Physics, Siberian Division, Russian Academy of Sciences, Novosibirsk, 630090 Russia
"Coherent Technologies" Research and Production Enterprise, Novosibirsk, Russia
** e-mail: zakrdm@isp.nsc.ru*
Received April 16, 2003

Abstract—An abnormal discharge is realized in which electron beams with energies in a kiloelectronvolt range are generated at an efficiency of $\eta \sim 1$. The results are explained within the framework of a photoelectron discharge model. A transition to this mechanism is possible due to a significant increase in the power of self-illumination from a large electron beam drift volume. The passage to a discharge with predominant photoemission leads to a decrease in the cathode potential fall region, a drop in the ion current to the cathode, and an increase in the efficiency. *© 2003 MAIK "Nauka/Interperiodica".*

Low-pressure gas discharges are traditionally used as simple and reliable sources of electron beams with the energies ranging from units to hundreds of kiloelectronvolts. A relatively high electron beam generation efficiency ($\eta > 0.5$) in an abnormal glow discharge in helium is retained at a gas pressure of up to $P \sim 1$ Torr [1]. Under these conditions, it is possible to connect the region of electron acceleration directly to the active region of a laser or some other plasma device. This possibility is used, for example, in a large class of electron beam pumped lasers [2].

Further development of the methods of electron beam generation at medium gas pressures was provided by the discovery of the open discharge [3–5], which significantly increased the possibilities of creating high-efficiency metal vapor lasers [2, 5]. In the open discharge, electrons are accelerated in a narrow (~1 mm) gap between a cathode and a grid anode and then enter a long drift space. Owing to the small gap width, ionization processes in this region are relatively weak and the main source of electrons is photoemission under the action of vacuum ultraviolet (VUV) radiation emitted from the drift space. This mechanism provides for high electron beam generation efficiencies ($\eta > 0.9$) at medium gas pressures (for helium, above 10 Torr). In a system with the metal grid replaced by a developed dielectric structure [7, 8], the photoelectron mechanism becomes absolutely predominant and the practical efficiency of the electron beam generation in a kiloelectronvolt energy range reaches $\eta \sim 1$.

In this study, the self-sustained photoemission dominated discharge was realized under the conditions different from those used previously [7, 8]. The approach based on suppression of the ion flux to the cathode results in a discharge current density $j = f(U_{cf}, P)$ three orders of magnitude lower then that in the abnormal glow discharge (U_{cf} is the cathode potential fall, which is virtually equal to the applied voltage U). However, the photoelectron discharge mechanism can be rendered predominant without taking special technical measures for suppressing the ion-induced electron emission. In this study, the same goal was achieved by increasing the discharge volume (mostly, by increasing the cathode diameter and the drift space length). The ion-induced electron emission under the abnormal glow discharge conditions is essentially a one-dimensional phenomenon: the process is determined by the ion (or fast atom) energy and is independent (to the first approximation) of the cathode area and the drift space length. In contrast, the photoemission current density is controlled by the discharge geometry [6]. If the discharge volume is increased to a certain level, the density of the electron current due to photoemission can exceed that due to the heavy particle bombardment of the cathode. In the experiment, this is manifested by an increase in the current density (at constant U and P) and in the electron beam generation efficiency calculated as $\eta = I_e/(I_e + I_a)$, where I_e is the electron beam current and I_a is the electron current to the anode compensating for the ion current to the cathode.

The experiments were performed in discharge cells (Fig. 1) analogous to that described previously [1], using neon as the working gas. The discharge was initiated between a spherical aluminum cathode and an iron ring anode (fixed on the cell wall). The electron beam current was detected by the electron collector. The distance between cathode and anode was $l = 3$ cm $> l_{cf}$, where l_{cf} is the cathode potential fall length (in the nor-

1063-7850/03/2910-0873$24.00 © 2003 MAIK "Nauka/Interperiodica"

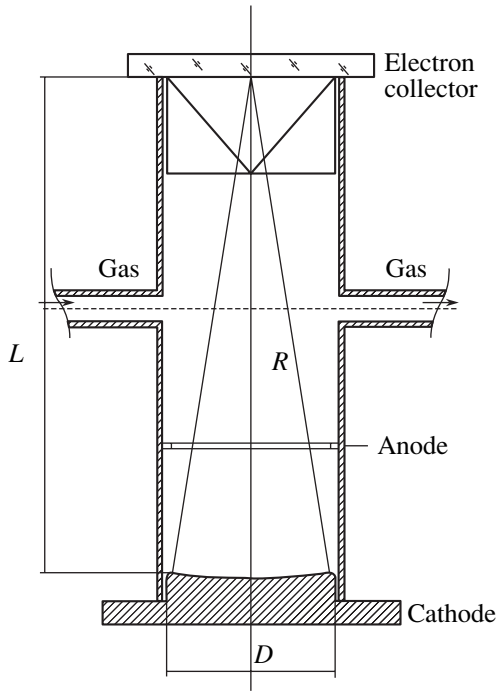

Fig. 1. A schematic diagram of the gas discharge cell (see the text for explanations).

mal discharge at a pressure used in the experiment). The cathode diameter D, the curvature radius R, and the cell length L (see table) obey an approximate similarity relation (except cell no. 4, for which the electron beam penetration depth in the range of working pressures and discharge voltages could be much smaller than L = 50 cm according to the similarity relation).

Figure 2 shows the current–voltage (j–U) characteristics of the discharge and the electron beam generation efficiency η as a function of the voltage U for cells no. 2 (j_2, η_2) and no. 4 (j_4, η_4) at a neon pressure of P = 38 Pa (j_i is the total current density in the corresponding cell).

Figure 3 presents the plot of $\eta(D)$ for U = 1000 V and P = 38 Pa (curve *1*); curves *2* and *3* show $\eta(P)$ and $j/j_{AGD}(P)$, respectively, for cell no. 4 operating at U = 500 V (here, $j_{AGD} = 5.65 \times 10^{-13} P^2 U_{cf}^3$ [mA/cm^2] is the current density for an abnormal glow discharge in neon, determined from the data of Gunterschulze and Klarfeld reproduced in [9, 10]).

Discharge cell dimensions

Cell no.	D, mm	R, mm	L, mm	S, mm^2
1	17.5	42	52	241
2*	34	100	103	908
3	76	240	217	4536
4	170	560	230	22700

* Cell no. 2 has the same cathode diameter as the cell studied in [1].

As can be seen from Fig. 2, cell no. 2 with the cathode dimensions analogous to those used in [1] exhibits an efficiency typical of the abnormal glow discharge, whereas the η value for cell no. 4 reaches 0.99. Such values of the electron beam generation efficiency can be obtained only in the photoemission dominated discharge [6]. The j–U curves also reveal a difference: the current density in cell no. 2 obeys the law $j_{AGD} \sim U^3$ typical of the abnormal glow discharge, while that in cell no. 4 is almost ten times greater and is described by the relation $j \sim (U–230)$, where $U_{in} \approx 230$ V is the discharge initiation voltage. A change in the character of the j–U curve is related to an increase in the energy per electron of the beam dissipated in the drift space, which is approximately proportional to U (for the given discharge geometry and voltage interval).

A transition to the photoelectron discharge with increasing cathode diameter and working gas pressure is clearly manifested in Fig. 3 by curves *1* and *2*, respectively. At a pressure of P = 38 Pa, the effect of photoemission for a cathode with D = 34 mm is already significant, while the discharge for D = 76 mm is maintained mostly due to this factor (see curve *1* in Fig. 3). In a cell with D = 170 mm, the photoelectron discharge becomes predominant in the region of pressures P > 25 Pa, where the current density is almost twice that in the abnormal glow discharge; at P = 60 Pa, this growth becomes almost tenfold (Fig. 3, curve *3*) and reaches j/j_{AGD} = 12 at U = 400 V.

Thus, the dominating mechanism of electron emission exhibits a change in a discharge cell of sufficiently large dimensions. It is interesting to note that a significant influence of photoemission for a cell with increasing D in the open discharge [6] and in this study is observed at approximately equal values of the $P \times D$ product and is accompanied by a rapid growth in the efficiency η. An analogous transition to the photoemission dominated discharge takes place in the microchannels of plasma displays [11], where (by analogy with the open discharge) this is provided by increased pressure in the working medium. The calculations [6] show that the photoemission coefficient in cell no. 4 reaches γ = 1 already for an energy of 300–400 eV per electron dissipated in the drift space, which also confirms the photoelectron emission mechanism. On the other hand, the value of $\eta \sim 0.99$ is not merely a consequence of this transition: for a ratio of j/j_{AGD} = 10 provided by the photoinduced current, the calculation yields $\eta \sim 0.9$, rather than 0.99 as observed in the experiment. From this we infer that the ion current to the cathode (and, accordingly, the compensating electron current to the anode) in the photoemission dominated discharge is significantly reduced as compared to that in the abnormal glow discharge.

In order to elucidate the mechanism responsible for a decrease in the ion current and an increase in the effi-

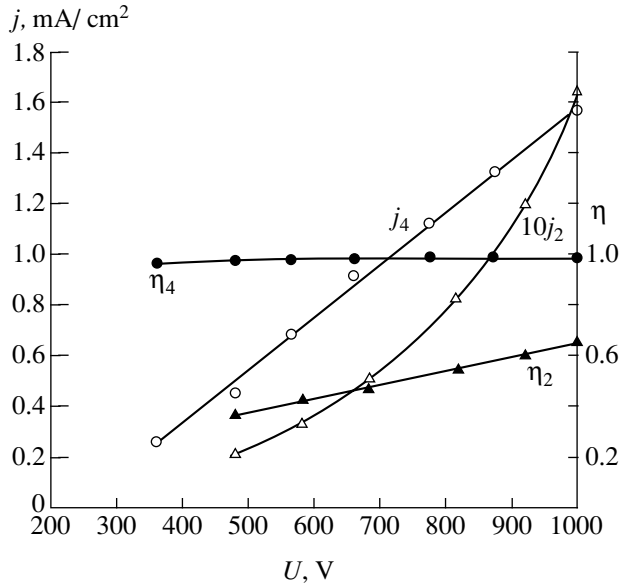

Fig. 2. The current–voltage (j–U) characteristics of the discharge and the electron beam generation efficiency η as a function of the applied voltage U for the cells no. 2 (j_2, η_2; D = 34 mm) and no. 4 (j_4, η_4; D = 170 mm).

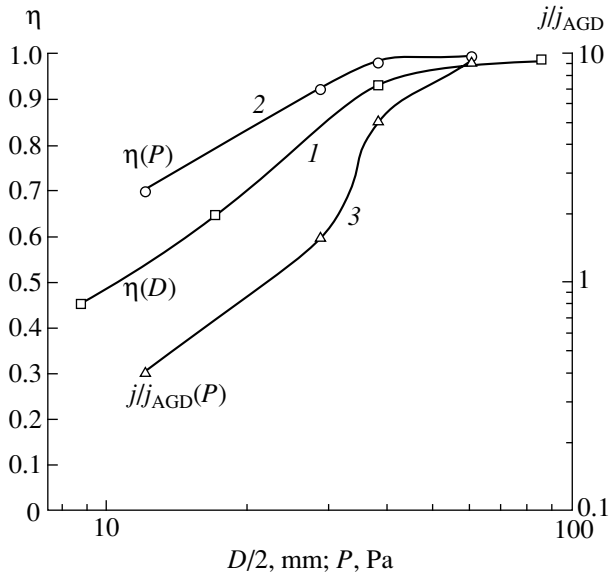

Fig. 3. The plots of (*1*) η(D) for U = 1000 V and P = 38 Pa and (*2*, *3*) η(P) and $j/j_{AGD}(P)$, respectively, for cell no. 4 (D = 170 mm) operating at U = 500 V (j_{AGD} is the current density for an abnormal glow discharge).

ciency up to η ~ 0.99, we calculated the potential profile in the cathode region with allowance of the predominant photoemission and the gas displacement as a result of heating. Under these conditions, the cathode potential fall length decreases as compared to that in the abnormal glow discharge (as was established long ago by Engel, see [10]). At a pressure of P = 60 Pa, this decrease is approximately twofold. As the cathode potential fall length in the photoelectron discharge decreases, the field strength in this region grows. This leads to a decrease in the rate of secondary ionization processes and to exponential drop in the flux of ions and fast atoms to the cathode. As a result, the secondary electrons generated in the range of energies corresponding to the maximum ionization cross section exhibit runaway and are detected on the collector, rather than on the anode.

Taking into account that the ion-induced electron emission is characterized by η ~ 0.5 (the left point of curve *1* for D = 17.5 mm in Fig. 3) and j/j_{AGD} = 10 for D = 170 mm, we obtain with allowance of the above considerations that $I_e/I_a > 50$ and η > 0.98 in agreement with experiment.

In conclusion, we have demonstrated that an increase in the discharge cell volume leads to a change in the principal mechanism of electron emission in the abnormal glow discharge, whereby photoemission begins to prevail over the ion-induced emission. This phenomenon allows simple discharge devices to be created for the obtaining of high-power electron beams with energies in the kiloelectronvolt range, an efficiency η ~ 1, and a reduced level of cathode sputtering.

REFERENCES

1. J. J. Rocca, J. D. Meyer, M. R. Farrell, *et al.*, J. Appl. Phys. **56**, 790 (1984).
2. C. E. Little, *Metal Vapour Lasers* (Wiley, Chichester, 1999).
3. P. A. Bokhan and G. V. Kolbychev, Zh. Tekh. Fiz. **51**, 1823 (1981) [Sov. Phys. Tech. Phys. **26**, 1057 (1981)].
4. P. A. Bokhan and A. R. Sorokin, Zh. Tekh. Fiz. **55**, 88 (1985) [Sov. Phys. Tech. Phys. **30**, 50 (1985)].
5. P. A. Bokhan and E. I. Molodykh, *Pulsed Metal Vapour Lasers* (Kluwer, Dortrecht, 1996), Vol. 5, p. 137.
6. A. P. Bokhan and P. A. Bokhan, Opt. Atmos. Okeana **15**, 216 (2002).
7. P. A. Bokhan and D. É. Zakrevskiĭ, Pis'ma Zh. Tekh. Fiz. **28** (11), 21 (2002) [Tech. Phys. Lett. **28**, 454 (2002)].
8. P. A. Bokhan and D. E. Zakrevsky, Appl. Phys. Lett. **81**, 2526 (2002).
9. A. L. Ward, J. Appl. Phys. **33**, 2789 (1962).
10. V. L. Granovskiĭ, *Electric Current in a Gas* (Nauka, Moscow, 1971).
11. R. Ganter, J. Ouyang, Th. Callegari, *et al.*, J. Appl. Phys. **91**, 992 (2002).

Translated by P. Pozdeev

Technical Physics Letters, Vol. 29, No. 10, 2003, pp. 876–878. Translated from Pis'ma v Zhurnal Tekhnicheskoĭ Fiziki, Vol. 29, No. 20, 2003, pp. 88–94.

The Effect of Phase Modulation of Scattered Radiation on the Asymptotic Behavior of the Contrast Ratio of Partially Coherent Speckle Fields

D. A. Zimnyakov*, R. A. Zdrazhevskiĭ, V. A. Trifonov, E. V. Gur'yanov, and A. V. Zhimskiĭ

Saratov State University, Saratov, Russia

** e-mail: zimnykov@sgu.ru*

Received February 20, 2003

Abstract—We analyze the influence of a weak phase modulation of multiply scattered partially coherent light fields on the variance of fluctuations of the scattered field intensity. It is suggested to perform diagnostics of scattering media by analyzing the probing radiation scattered from a "modulating" medium and determining the speckle intensity index (or contrast ratio) upon introduction of an object studied into the scheme of measurements. The proposed method is experimentally verified on model scattering media. © *2003 MAIK "Nauka/Interperiodica".*

Probing randomly inhomogeneous media by partially coherent radiation is a promising direction in the development of optical diagnostics. Various modifications of the method of incoherent interferometry, based on the measurement of interference of partially coherent object and reference beams at a periodic variation of the path length difference between these beams, is now widely used in various medical and technological applications [1–4]. One of the methods used for the diagnostics of scattering media is the statistical analysis of speckle fields formed when a partially coherent probing light is scattered from an object [5–9]. In this case, the diagnostic parameter is the scattered field intensity index, $\beta_I = \langle(\delta I)^2\rangle/\langle I\rangle^2$, or the related speckle contrast ratio defined as $V = \sqrt{\beta_I}$, where $\langle(\delta I)^2\rangle$ is the variance of intensity fluctuations and $\langle I\rangle$ is the average intensity of speckles over the detection zone.

Within the framework of a scalar model describing interference of the partial components of scattered fields, characterized by the probability density $\rho(s)$ of the optical path lengths in a scattering medium, the speckle intensity index is expressed as follows [8, 9]:

$$\beta_I = \int_0^\infty |g(\Delta s/l_c)|^2 \Re(\Delta s)\, d(\Delta s). \qquad (1)$$

Here, $g(\Delta s/l_c)$ is the coherence function of the radiation source, l_c is the coherence length of the probing radiation, and $\Re(\Delta s) = \int_0^\infty \rho(s)\rho(s + \Delta s)ds$ is the probability density function of the optical path length difference for the partial components. In this case, the diagnostics consists in restoration of the probability density $\rho(s)$ from the experimental dependences of β_I on l_c by means of numerical inversion of Eq. (1) for a given form of $g(\Delta s/l_c)$. Using the known $\rho(s)$ and solving the inverse problem of the theory of radiation transfer, it is possible to determine the optical characteristics of the medium.

We propose an approach to incoherent probing of scattering media based on an analysis of the probing radiation scattered from a "modulating" medium and the calculation of β_I upon introduction of an object studied into the scheme of measurements. An advantageous feature of the proposed method is the possibility of controlling the sensitivity of β_I with respect to variations of the optical properties of the object by selecting the "modulating" medium for the given characteristics of a light source. This method can be used for the analysis of weakly scattering media generating (in the case of traditional low-coherence radiation sources, such as superluminescent diodes) the speckle fields with $\beta_I \approx 1$, which makes this parameter almost insensitive to changes in the object characteristics.

This study was aimed at a theoretical analysis and experimental verification of the proposed method in the case of a weakly scattering medium playing the role of a source of phase modulation of the radiation transmitted through the "modulating" medium.

From an analysis of Eq. (1) in the case when $\langle\Delta s\rangle \gg l_c$, so that $\beta_I \ll 1$, it follows that $\beta_I \approx K\Re(0)l_c$, where K is the normalization coefficient. Taking into account the relation between $\Re(\Delta s)$ and $\rho(s)$ and using the Fourier image of the optical path length function $F_\rho(\omega) = \int_0^\infty \rho(s)\exp(-j\omega s)ds$, we arrive at the expression $\beta_I \approx Kl_c\int_{-\infty}^{\infty} |F_\rho(\omega)|^2\, d\omega$. Introduction of an additional scat-

1063-7850/03/2910-0876$24.00

terer into the scheme of measurements alters the path length statistics. The change can be described in terms of a convolution of the unperturbed density $\rho(s)$ and the pulsed response function $h(s)$ of the object: $\rho'(s) = \rho(s) \otimes h(s)$. In the absence of perturbations (i.e., when an optically homogeneous object is introduced to the scheme of measurements), $h(s) = \delta(s)$, where $\delta(s)$ is the delta function. In the presence of a scatterer, the value of β_I is determined as

$$\beta_I' \approx K l_c \int_{-\infty}^{\infty} |F_\rho(\omega) H(\omega)|^2 d\omega, \qquad (2)$$

where $H(\omega) = \int_0^\infty h(s)\exp(-j\omega s)ds$. When the object produces a weak phase modulation of the radiation scattered from the "modulating" medium, $|H(\omega)|^2$ can be represented as a combination of the unperturbed and perturbed components, $|H(\omega)|^2 \approx 1 - |\Delta H(\omega)|^2$, so that

$$\beta_I' = \beta_I - \Delta\beta_I \approx \beta_I - K l_c \int_{-\infty}^{\infty} |F_\rho(\omega)\Delta H(\omega)|^2 d\omega. \qquad (3)$$

Let us consider an object in the form of random phase screen (RPS) [10, 11] and establish a relationship between the RPS parameters (correlation radius r_ϕ and the variance of fluctuations σ_ϕ^2 of the boundary field) and the transmission function $H(\omega)$. Perturbations of the ensemble of partial components of the scattered radiation field are related to random phase shifts upon scattering on the object structure. Within the framework of an RPS model with Gaussian statistics of the boundary field phase fluctuations, $h(s)$ can be represented as

$$h(s) \approx (1/\sqrt{2\pi\sigma_s})\exp\{-(s - 3\sigma_s)^2/2\sigma_s^2\}, \qquad (4)$$

with a permissible accuracy obeying the condition $s \geq 0$. Then, $|H(\omega)|^2 \approx \exp\{-\sigma_s^2 \omega^2\}$ and the variance of optical path lengths σ_s^2 has to be evaluated proceeding from the scheme of detection of scattered radiation.

In particular, in the case when a lens system is used for imaging the surface of a "modulating" medium, with the statistical analysis of speckles in the image plane, the σ_s^2 value is determined by the structural function of fluctuations of the boundary field phase, $D_\phi(\bar{\rho}) = \langle\{\phi(\bar{r}) - \phi(\bar{r} + \bar{\rho})\}^2\rangle$ [10], and depends on the resolving power of the lens system. We can use the following expression: $\sigma_s^2 \approx K' D_\phi(R)$, where K' is a coefficient dependent on the radiation wavelength and R is the characteristic size of an RPS area determining the dispersion s as a function of the lens resolution. We adopt the following model [12]: $D_\phi(\bar{\rho}) = 2\sigma_\phi^2\{1 - \exp\lfloor-(|\bar{\rho}|/r_\phi)^a\rfloor\}$, where a is a parameter. This implies that $|H(\omega)|^2$ has a quadratic asymptotics of the type $1 - 2K'P(\sigma_\phi, r_\phi)\omega^2$, where $P(\sigma_\phi, r_\phi) = \sigma_\phi^2\{1 - \exp\lfloor-(R/r_\phi)^a\rfloor\}$. Under the given conditions of detection, the asymptotic behavior corresponds to the linear dependence of $\Delta\beta_I$ on $P(\sigma_\phi, r_\phi)$.

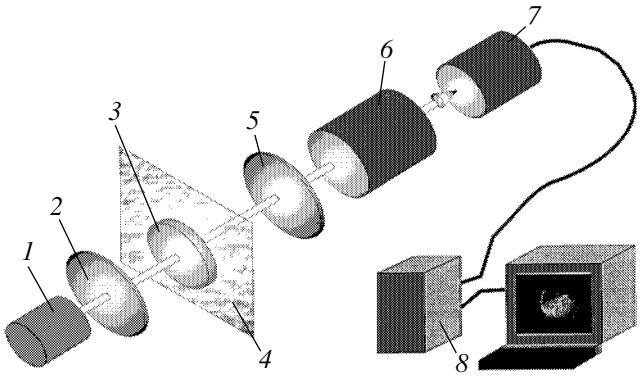

Fig. 1. A schematic diagram of the experimental setup: (*1*) superluminescent diode with collimator; (*2*) polarizer; (*3*) "modulating" medium; (*4*) sample (random phase screen); (*5*) polarizer; (*6*) objective; (*7*) CCD camera; (*8*) personal computer with display.

Figure 1 shows a schematic diagram of the experimental setup used for verification of the proposed method. The radiation source was a superluminescent diode (P_{em} = 10 mW, $\bar{\lambda}$ = 820 nm, $\Delta\lambda$ = 16 nm). The radiation beam was collimated and transmitted through a 10-mm-thick optic fiber plate (OFP) with a fiber diameter of 5 μm and aperture ratio of 0.2, which plays the role of a "modulating" medium. The speckle-modulated images of the plate surface in the system with and without objects were recorded using a CCD camera of the VS-CTT-60-075 type (SObI Videoscan, Russia) equipped with an LMZ13A5M (LMZ) objective lens. The objective aperture was selected so that the average speckle size in the image plane would be 3–4 times the CCD matrix pixel size. The speckle modulation of the image was provided by stochastic interference of the paraxial beams propagating from the OFP–object system. In order to exclude the depolarizing influence of the "modulating" medium upon the β_I value, we used polarizers with parallel oriented layers.

The image was processed and β_I values for a selected fragment were calculated. For the OFP surface in the absence of objects, the β_I value was 0.24 ± 0.03. The model objects were RPSs (whitened speckle patterns [12] with various values of σ_ϕ, r_ϕ, and a). Preliminary estimates of the σ_ϕ, r_ϕ, and a values were obtained upon probing the system with a spatially modulated laser beam [13]. For some objects, the fluctuation auto-

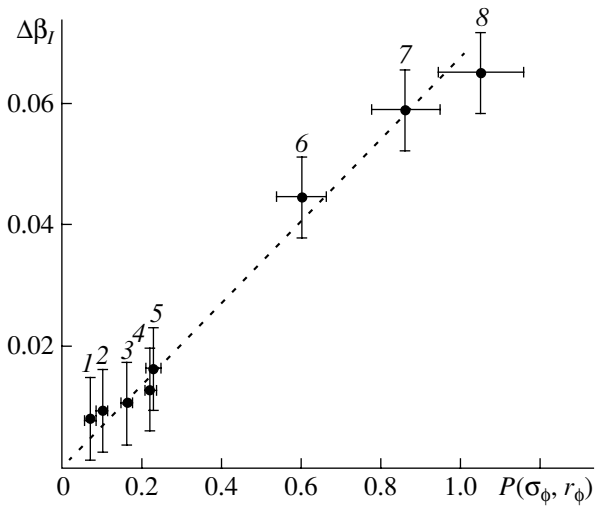

Fig. 2. A plot of the scattered field intensity index $\Delta\beta_I$ in the image plane versus parameter $P(\sigma_\phi, r_\phi)$ for the optical scheme with various RPS samples: (*1*) $\sigma_\phi = 0.7$, $r_\phi = 7$ μm, $a = 2$ (oscillating autocorrelation function of the boundary field phase); (*2*) $\sigma_\phi = 1.4$, $r_\phi = 21$ μm, $a = 1.6$; (*3*) $\sigma_\phi = 1.6$, $r_\phi = 18.5$ μm, $a = 1.6$; (*4*) $\sigma_\phi = 1.7$, $r_\phi = 18$ μm, $a = 1.5$; (*5*) $\sigma_\phi = 1.95$, $r_\phi = 19$ μm, $a = 1.6$; (*6*) $\sigma_\phi = 1.4$, $r_\phi = 6.5$ μm, $a = 1.6$ (oscillating autocorrelation function of the boundary field phase); (*7*) $\sigma_\phi = 1.3$, $r_\phi = 4.1$ μm, $a = 1.6$; (*8*) $\sigma_\phi = 1.25$, $r_\phi = 3$ μm, $a = 1.65$.

correlation functions $\phi(\bar{r})$ exhibited an oscillating character (the oscillation period was taking into account in evaluating r_ϕ).

Figure 2 shows a plot of $\Delta\beta_I$ versus $P(\sigma_\phi, r_\phi)$ for the samples studied. The $P(\sigma_\phi, r_\phi)$ values were calculated using R as a fitting parameter, which was determined from the comparison of $\Delta\beta_I$ values for the samples with significantly different r_ϕ but close σ_ϕ and a values (samples *2* and *7*). The R value amounted to 3.3 μm. The confidence intervals indicated in Fig. 2 were determined from an analysis of the uncertainty of evaluating σ_ϕ, r_ϕ, and a and determining $\Delta\beta_I$ in our experiments. Thus, within the developed model, the dependence presented in Fig. 2 for a weakly scattering medium admits with acceptable accuracy a linear approximation. An increase in $P(\sigma_\phi, r_\phi)$ is accompanied by the natural growth of a systematic error of the linear approximation (sample *8*), reaching large values for the sample with $\sigma_\phi \geq 2$ and small r_ϕ (these points are not depicted in the plot).

The proposed method can be used for a rapid diagnostics of weakly scattering media by evaluating $P(\sigma_\phi, r_\phi)$ from the measured values of $\Delta\beta_I$. Additional possibilities in determining σ_ϕ, r_ϕ, and a values can be provided by using various detection conditions corresponding to different values of the parameter R.

Acknowledgments. This study was supported by the Russian Foundation for Basic Research (project no. 01-02-17493) and the US Civilian Research and Development Foundation for the Independent States of the Former Soviet Union (CRDF Award No. REC-006).

REFERENCES

1. A. F. Fercher, J. Biomed. Opt. **1**, 157 (1996).
2. G. J. Tearney, M. E. Brezinski, B. E. Bouma, *et al.*, Science **267**, 2037 (1997).
3. W. Drexler, U. Morgner, F. X. Kartner, *et al.*, Opt. Lett. **24**, 1221 (1999).
4. D. A. Boas, K. K. Bizheva, and A. M. Siegel, Opt. Lett. **23**, 319 (1998).
5. C. A. Thompson, K. J. Webb, and A. M. Weiner, J. Opt. Soc. Am. A **14**, 2269 (1997).
6. G. Hausler, J. M. Herrmann, R. Kummer, *et al.*, Opt. Lett. **21**, 1087 (1996).
7. A. Eigensee, G. Hausler, J. M. Herrmann, *et al.*, Proc. SPIE **2925**, 169 (1996).
8. L. V. Kuznetsova and D. A. Zimnyakov, Proc. SPIE **4001**, 217 (2000).
9. J.-T. Oh, D. A. Zimnyakov, and G. G. Akchurin, Proc. SPIE **4705**, 137 (2002).
10. S. M. Rytov, Yu. A. Kravtsov, and V. I. Tatarskiĭ, *Introduction to Statistical Radio Physics* (Nauka, Moscow, 1978), Part 2.
11. J. W. Goodman, *Statistical Optics* (Wiley, New York, 1985; Mir, Moscow, 1988).
12. V. P. Ryabukho, Opt. Spektrosk. **94**, 513 (2003) [Opt. Spectrosc. **94**, 453 (2003)].
13. V. P. Ryabukho, Yu. A. Avetisyan, and A. B. Sumanova, Opt. Spektrosk. **79**, 299 (1995) [Opt. Spectrosc. **79**, 275 (1995)].

Translated by P. Pozdeev